

# **Thesis Title**

**Thomas P. Ogden**

---

## **Abstract**

Here is my abstract.

# **Thesis Title**

**Thomas P. Ogden**

---

A thesis submitted in partial fulfilment  
of the requirements for the degree of  
Doctor of Philosophy.



Department of Physics  
Durham University

January 18, 2016

## *Declaration*

I confirm that no part of the material offered has previously been submitted by myself for a degree in this or any other University. Where material has been generated through joint work, the work of others has been indicated.

Thomas P. Ogden

Durham, January 18, 2016

The copyright of this thesis rests with the author. No quotation from it should be published without their prior written consent and information derived from it should be acknowledged.

*Dedicated to Someone Special,  
for some special reason.*

# *Contents*

<b>1</b>	<b>Introduction</b>	<b>10</b>
<b>2</b>	<b>Propagation of Light in Thermal Atomic Vapours</b>	<b>11</b>
2.1	Introduction . . . . .	11
2.2	Deriving the Propagation Equation . . . . .	11
2.2.1	Maxwell's Equations and the Wave Equation . . . . .	12
2.2.2	The Slowly Varying Envelope Approximation . . . . .	14
2.2.3	Energy and Intensity . . . . .	16
2.3	Linear Optics, Susceptibility and Refractive Index . . . . .	16
2.3.1	Susceptibility . . . . .	16
2.3.2	Refractive Index . . . . .	19
2.4	Interaction of Light with Atoms . . . . .	20
2.4.1	Spontaneous Decay of Excited States . . . . .	21
2.4.2	The Interaction Hamiltonian . . . . .	21
2.4.3	Dipole Matrix Elements and Parity . . . . .	23
2.4.4	Atomic Coherence and Polarisation . . . . .	24
2.4.5	Thermal Atoms . . . . .	25

2.4.6	Shifting to the Speed-of-Light Reference Frame . . . . .	26
2.4.7	A Recap . . . . .	26
2.5	Linear Propagation in Two-level Atoms . . . . .	27
2.5.1	The Two-level System . . . . .	28
2.5.2	The Natural Unit System . . . . .	29
2.5.3	Weak Probe Lineshape . . . . .	30
2.5.4	Weak Pulse Propagation Results . . . . .	31
2.5.5	Spectral Analysis . . . . .	34
2.5.6	The Voigt Profile . . . . .	40
2.6	Discussion . . . . .	42
<b>3</b>	<b>Nonlinear Propagation Phenomena</b>	<b>44</b>
3.1	Introduction . . . . .	44
3.2	Self-Induced Transparency & Optical Solitons . . . . .	45
3.2.1	The Area Theorem . . . . .	46
3.2.2	Self-Induced Transparency . . . . .	47
3.2.3	Pulse Breakup . . . . .	53
3.3	Propagation of Light in Three-level Atoms . . . . .	56
3.4	Matched Pulses & Simultons . . . . .	58
3.4.1	Literature Review . . . . .	58
3.4.2	The Two-Photon Area Theorem . . . . .	60
3.5	Discussion . . . . .	62
<b>4</b>	<b>Storage and Retrieval of Dark-State Polaritons</b>	<b>63</b>

4.1	Introduction	63
4.2	Electromagnetically-Induced Transparency in $\Lambda$ -Type Atoms	63
4.3	Pulse Propagation in EIT Media	63
4.4	Storage & Retrieval of Dark-State Polaritons	63
4.5	Discussion	63
<b>5</b>	<b>Two-Photon Excitation in a High-Intensity Beam</b>	<b>64</b>
5.1	Introduction	64
5.2	Description of the Experiment	65
5.3	Theoretical Model	67
5.3.1	Angular Momentum Structure	69
5.3.2	Reducing the Transition Dipole Matrix Elements	73
5.3.3	Selection Rules	75
5.3.4	The Interaction Hamiltonian	76
5.3.5	Spontaneous Decay and the Master Equation	78
5.4	Numerical Results	80
5.5	Discussion	80
<b>6</b>	<b>Propagation of Short Pulses in V-Type Atoms</b>	<b>81</b>
6.1	Introduction	81
6.2	Description of the Experiment	82
6.2.1	Experimental Results	84
6.3	Theoretical Model	86
6.3.1	Simulation Results	88

6.3.2	Inhomogeneous Broadening	93
6.3.3	Collision Dephasing	94
6.3.4	Hyperfine Pumping	95
6.4	Comparison of Simulation Results with Data	97
6.4.1	Power Dependence	99
6.4.2	Temperature Dependence	101
6.4.3	A Recap	103
6.5	Analysis of the Evolution of a Single Atom	103
6.5.1	Coherent Population Trapping	106
6.6	Simulating Longer Propagation Distances	109
6.6.1	Propagation in the Coupling Pulse Scheme	109
6.6.2	Comparison with Experimental Data	113
6.6.3	Hyperfine Structure & Degeneracy	115
6.6.4	Weak Probe Fields	117
6.7	Discussion	118
7	Conclusions	123
A	Dynamics of Open Quantum Systems	124
A.1	The Density Operator	124
A.2	The Master Equation	126
B	Numerical Integration of the Lindblad Master Equation	128
C	Numerical Integration of the Maxwell-Bloch Equations	129

C.1	Formulating the Problem	129
C.2	Computational Scheme	131
C.2.1	Details of the Algorithm	133
C.2.2	Code Implementation	134
C.3	Convergence & Accuracy	134
C.4	Parallelisation & Performance	138
D	The Two-Step Adams-Bashforth Method	141
	Acknowledgements	144
	Bibliography	145

# *1     Introduction*

## *2 Propagation of Light in Thermal Atomic Vapours*

### *2.1 Introduction*

In this chapter we will define the model for propagation in thermal atoms to be used throughout the thesis, based on the well-known Maxwell Bloch (MB) equations. We will introduce the concept of susceptibilities and discuss analytic solutions to the equations that are available in the regime of weak incident light, before generalising the problem to nonlinear interaction with quantised atoms. Finally we will present results from numerical solutions and compare with the analytic results for weak fields to verify the accuracy of the numerical model.

### *2.2 Deriving the Propagation Equation*

In this section we will derive an equation to describe the propagation of a classical electromagnetic field in a polarised medium. Our starting point, naturally, is Maxwell's set of equations of classical electrodynamics.

### 2.2.1 Maxwell's Equations and the Wave Equation

In a medium with no free charges or free current, Maxwell's equations for the electric field  $\mathbf{E}$  and the magnetic field  $\mathbf{B}$  can be written<sup>1</sup>

$$\nabla \cdot \mathbf{D} = 0 \quad (2.1a)$$

$$\nabla \cdot \mathbf{B} = 0 \quad (2.1b)$$

$$\nabla \times \mathbf{E} = -\frac{\partial \mathbf{B}}{\partial t} \quad (2.1c)$$

$$\nabla \times \mathbf{B} = \mu_0 \frac{\partial \mathbf{D}}{\partial t}. \quad (2.1d)$$

The electric displacement  $\mathbf{D}$  accounts for the effect of charges in a medium and is given by

$$\mathbf{D} = \epsilon_0 \mathbf{E} + \mathbf{P} \quad (2.2)$$

where  $\epsilon_0$  is the vacuum permittivity and the electric polarisation  $\mathbf{P}$  describes the cumulative effect of induced dipole moments in individual atoms. We'll discuss the source of polarisation in atoms further in section 2.3.

Taking the curl of (2.1c) and substituting (2.1d) we find

$$\nabla \times (\nabla \times \mathbf{E}) = -\mu_0 \frac{\partial \mathbf{D}^2}{\partial t^2}.$$

We then apply the vector identity

$$\nabla \times (\nabla \times \mathbf{E}) = \nabla(\nabla \cdot \mathbf{E}) - \nabla^2 \mathbf{E}$$

and, assuming that the polarisation varies little in the plane transverse to propagation such that  $\nabla \cdot \mathbf{P} \approx 0$ , arrive at the Maxwell wave equation

$$\nabla^2 \mathbf{E} - \frac{1}{c^2} \frac{\partial^2 \mathbf{E}}{\partial t^2} = \mu_0 \frac{\partial^2 \mathbf{P}}{\partial t^2}. \quad (2.3)$$

The Maxwell wave equation (MWE) thus describes the wave-like propagation of an electric field  $\mathbf{E}$  through a medium with polarisation  $\mathbf{P}$ . The

second derivative on the right-hand side tells us that the accelerating charges described by  $\mathbf{P}$  can act as a source of new components of the electromagnetic field. For this reason, polarisation plays a critical role in practically all optical phenomena.<sup>2</sup>

A similar propagation equation to (2.3) may be derived for the magnetic field, however we'll find that the interaction of atoms with the electric field dominates and so we will not consider  $\mathbf{B}$  further.

We will consider 1D propagation along the  $z$ -axis, a restriction well-justified by the deconstructive interference of light scattered by atomic dipoles in directions not aligned with the incident radiation.<sup>3</sup> Then we might write the transverse field as  $\mathbf{E} = \hat{\mathbf{x}}E(z, t)$ , where  $\hat{\mathbf{x}}$  is a unit vector perpendicular to  $z$ . We assume that we are dealing with atoms that are electrically neutral to start with, such that all of the polarisation in the medium will be induced by that field, so we may similarly set  $\mathbf{P} = \hat{\mathbf{x}}P(z, t)$ . In this way we can reduce the MWE to the scalar form

$$\frac{\partial^2 E}{\partial z^2} - \frac{1}{c^2} \frac{\partial^2 E}{\partial t^2} = \mu_0 \frac{\partial^2 P}{\partial t^2}. \quad (2.4)$$

In the absence of sources (i.e.  $P = 0$ ) we can solve the homogeneous equation (2.4) analytically. For a nonconducting medium with spatially constant permeability and susceptibility the solution is a transverse monochromatic plane wave<sup>1</sup>

$$\tilde{E}(z, t) = \tilde{E}_0 e^{i(kz - \omega t)}. \quad (2.5)$$

where as usual  $k$  represents wavenumber and  $\omega$  the angular frequency. The amplitude is given by  $\tilde{E}_0$ . Of course, the electric field is an observable physical quantity and so must be real-valued — it is the real part of the complex  $\tilde{E}(z, t)$  given by

$$E(z, t) = \Re[\tilde{E}(z, t)] = \frac{1}{2}\tilde{E}_0(z, t)e^{i(kz - \omega t)} + \frac{1}{2}\tilde{E}_0^*(z, t)e^{-i(kz - \omega t)}. \quad (2.6)$$

We continue with the complex notation for the usual reason that manipulations, such as adding components of different phases, are much simpler.

By substituting (2.5) into (2.4) we obtain the simplest *dispersion relation* of  $\omega = ck$ , *i.e.* all frequencies travel at a speed  $c$ , a familiar result for light in vacuo. Such plane wave solutions will propagate without attenuation or dispersion, which is how we are able to look up at the night sky and observe light from distant stars that has travelled enormous distance through the void of interstellar space.

Light travelling through matter is a more complex problem. We next want to look for solutions to (2.4) in the presence of sources, such that we have  $P \neq 0$  describing induced atomic dipoles in the medium. For that we will need to make a useful approximation.

### 2.2.2 The Slowly Varying Envelope Approximation

If the spectrum of the electric field is narrowband, we approximate the field as the product of a quasi-monochromatic *carrier* function with angular frequency  $\omega$  and wavenumber  $k$  and a *slowly-varying envelope*

$$E(z, t) = \frac{1}{2}\mathcal{E}(z, t)e^{i(kz - \omega t)} + \frac{1}{2}\mathcal{E}^*(z, t)e^{-i(kz - \omega t)} \quad (2.7)$$

where the envelope is in general a complex function

$$\mathcal{E}(z, t) = |\mathcal{E}|e^{i\varphi}. \quad (2.8)$$

We apply the same treatment to the polarisation

$$P(z, t) = \frac{1}{2}\mathcal{P}(z, t)e^{i(kz - \omega t)} + \frac{1}{2}\mathcal{P}^*(z, t)e^{-i(kz - \omega t)} \quad (2.9)$$

with a polarisation envelope

$$\mathcal{P}(z, t) = |\mathcal{P}|e^{i\varphi}. \quad (2.10)$$

We can substitute these into (2.4) and by matching co-rotating terms we find

$$\left[ (\partial_{zz} + 2ik\partial_z - k^2) - \frac{1}{c^2}(\partial_{tt} - 2i\omega\partial_t - \omega^2) \right] \mathcal{E} = \mu_0(\partial_{tt} - 2i\omega\partial_t - \omega^2)\mathcal{P}. \quad (2.11)$$

Now we're set to make the *slowly-varying envelope approximation*.<sup>4</sup> If the envelope changes only a small amount over the distance of a wavelength, and over the duration of the optical period, we can take

$$\begin{aligned} |\partial_{zz}\mathcal{E}| &\ll k|\partial_z\mathcal{E}| \\ |\partial_{tt}\mathcal{E}| &\ll \omega|\partial_t\mathcal{E}| \end{aligned}$$

and neglect the second derivatives. Similar approximations hold for  $\mathcal{P}$ , where we may also neglect the first-order time derivative

$$\begin{aligned} |\partial_{zz}\mathcal{P}| &\ll k|\partial_z\mathcal{P}| \\ |\partial_{tt}\mathcal{E}| &\ll \omega|\partial_t\mathcal{E}| \\ |\partial_t\mathcal{P}| &\ll \omega|\mathcal{P}|. \end{aligned}$$

In the case of visible light with wavelengths on the order of 100 nm and optical periods of the order of 1 fs, where we're interested in the behaviour over ns or  $\mu$ s, this approximation is justified.

With these approximations made, (2.11) becomes

$$\left[ 2ik\partial_z - k^2 + \frac{1}{c^2}(2i\omega\partial_t + \omega^2) \right] \mathcal{E} = -\mu_0\omega^2\mathcal{P} \quad (2.12)$$

As the carrier wavenumber and frequency are still related by the vacuum dispersion relation  $\omega = ck$  we then obtain the first-order propagation equation

$$\left[ \frac{\partial}{\partial z} + \frac{1}{c} \frac{\partial}{\partial t} \right] \mathcal{E} = i \frac{k}{2\epsilon_0} \mathcal{P}. \quad (2.13)$$

The wave equation (2.13), first-order in space  $z$  and time  $t$ , can be solved numerically for a given medium, to determine how light will propagate through it. But we will next need to determine how the media through  $\mathcal{P}$  is itself affected by the field  $\mathcal{E}$ .

### 2.2.3 Energy and Intensity

In an experiment we will not be measuring the electric field directly, but the energy transferred to a detector such as a photon counter. Also, any macroscopic measurement of light is necessarily going to extend over many optical cycles (of duration  $\sim 10^{-15}$  s). So a property useful to us is the time-averaged power per unit area that the electromagnetic field transports through the medium, which we call the intensity  $I$  and is calculated to be<sup>5</sup>

$$I = \frac{1}{2}c\epsilon_0|\mathcal{E}^2|. \quad (2.14)$$

## 2.3 Linear Optics, Susceptibility and Refractive Index

The effect of an electric field  $\mathbf{E}$  applied on a single neutral atom is to separate the positively charged core (which moves in the direction of the field  $\mathbf{E}$ ) and the negatively charged electron cloud (which moves in the opposite direction  $-\mathbf{E}$ ) such that a dipole is induced on the atom parallel to the field. For an atomic vapour subject to a field, dipoles will be induced on many atoms. The cumulative effect is that the medium is polarised, and we define  $\mathbf{P}$  as the dipole moment per unit volume.

### 2.3.1 Susceptibility

In general, the instantaneous polarisation induced by the field at a time  $t$  is some function of the input field, which we may write as a power expansion<sup>2</sup> in  $\mathbf{E}$ ,

$$\mathbf{P}_{\text{inst}}(t) = \epsilon_0 \left[ \chi^{(1)}(t)\mathbf{E}(t) + \chi^{(2)}(t)\mathbf{E}(t)^2 + \chi^{(3)}(t)\mathbf{E}(t)^3 + \dots \right] \quad (2.15)$$

where the expansion coefficients  $\chi^{(j)}(t)$  are known as the  $j$ th- order susceptibilities.

If the applied field is weak, we find that the induced polarisation is proportional to that field, such that susceptibilities higher than  $\chi^{(1)}$  are taken as zero and terms higher than the first order in (2.15) are neglected. This is the regime of *linear optics*. In this thesis we are particularly interested in developing and understanding numerical solutions of *nonlinear* problems, *i.e.* those in which higher order terms become significant. Systems involving weak fields are commonplace however, and as they permit analytic solution, along with offering insight into a broad range of optical phenomena, we will look at the linear regime briefly.

The cumulative induced polarisation  $P(t)$  is an integral of the instantaneous polarisation over all times  $t'$  previous

$$P(t) = \varepsilon_0 \int_{-\infty}^t \chi(t') E(t - t') dt' \quad (2.16)$$

where we no longer require a superscript to define the linear susceptibility  $\chi(t) := \chi^{(1)}(t)$ . The upper limit on the integral expresses the causality condition that only the applied field at times in the past may affect the current state of the atoms.

So far we have described atomic response in the time domain, which is particularly useful when looking at time-dependent input fields such as short pulses. But it is also instructive to look at the frequency domain, which is advantageous when the input field is monochromatic. The change in perspective is effected as usual via the Fourier transform.<sup>3</sup> We will use the convention for the transform on the electric field envelope  $\mathcal{E}(t)$

$$\mathcal{E}(\omega) = \int_{-\infty}^{\infty} \mathcal{E}(t) e^{i\omega t} dt \quad (2.17)$$

and for the inverse

$$\mathcal{E}(t) = \frac{1}{2\pi} \int_{-\infty}^{\infty} \mathcal{E}(\omega) e^{-i\omega t} d\omega \quad (2.18)$$

and we define the transform in the same way for the polarisation envelope  $\mathcal{P}(t)$ .

Making the envelope and carrier ansatz as in (2.33) and substituting (2.18) into the right-hand side of (2.16), we get

$$\mathcal{P}(t) = \varepsilon_0 \int_{-\infty}^t \chi(t') \frac{1}{2\pi} \int_{-\infty}^{\infty} \mathcal{E}(\omega) e^{-i\omega(t-t')} d\omega dt'. \quad (2.19)$$

We now define the frequency-dependent linear susceptibility

$$\chi(\omega) := \int_{-\infty}^t \chi(t') e^{i\omega t'} dt' \quad (2.20)$$

such that

$$\mathcal{P}(t) = \frac{1}{2\pi} \int_{-\infty}^{\infty} \varepsilon_0 \chi(\omega) \mathcal{E}(\omega) e^{-i\omega t} d\omega. \quad (2.21)$$

This expression gives the time-dependent polarisation in terms of the frequency components of the field weighted by that frequency-dependent susceptibility function. We may then take the Fourier transform of the left-hand side and, as the equality holds for each frequency, we obtain the frequency domain linear response function

$$\mathcal{P}(\omega) = \varepsilon_0 \chi(\omega) \mathcal{E}(\omega). \quad (2.22)$$

We may now substitute this expression into (2.13), with  $\mathcal{E}(\omega)$  time-independent by the definition (2.17), to obtain

$$\frac{\partial \mathcal{E}(z, \omega)}{\partial z} = i \frac{k}{2} \chi(\omega) \mathcal{E}(z, \omega). \quad (2.23)$$

This first-order differential equation in  $z$  has the analytical solution

$$\mathcal{E}(z, \omega) = e^{i \frac{k}{2} \chi z}. \quad (2.24)$$

Having determined an expression for the electric field envelope in terms of the frequency-dependent susceptibility, we can put this expression for the envelope into 2.13 in order to determine the effect it will have. It is useful to separate the real and imaginary parts of the susceptibility  $\chi(\omega) := \chi_R(\omega) + i\chi_I(\omega)$ , and we find

$$\mathcal{E}(z, \omega) = \mathcal{E}(0, \omega) e^{i(\frac{k}{2}\chi_R z)} e^{-\frac{k}{2}\chi_I z}. \quad (2.25)$$

The real part of the frequency dependent susceptibility then corresponds to a phase shift  $\frac{k}{2}\chi_R z$  and so dispersion, and the imaginary part diminishes the field. As defined in (2.14) the intensity  $I \propto |\mathcal{E}|^2$  and so is attenuated as it progresses through the medium via

$$I(z, \omega) = I_0(z, \omega)e^{-\alpha(\omega)z} \quad (2.26)$$

where the absorption coefficient  $\alpha(\omega) := k\chi_I(\omega)$ . This is the familiar Beer law of absorption for weak fields.

### 2.3.2 Refractive Index

If we return back to the Maxwell equations, we see by substitution of the susceptibility  $\chi$  into the definition for dispersion (2.2), we get

$$\mathbf{D} = \epsilon_0(1 + \chi)\mathbf{E}. \quad (2.27)$$

Deriving the Maxwell wave equation again using this substitution, we find that the result is as for propagation in free space but with the vacuum speed  $c$  replaced with a general phase velocity

$$v_p = \frac{c}{\sqrt{1 + \chi}} = \frac{c}{n} \quad (2.28)$$

where  $n$  is the refractive index, familiar from geometrical optics. In most linear media  $\chi$  is positive, so light travels more slowly in the medium.<sup>6</sup>

This leads us to consider what this velocity represents, considering that photons are massless and must travel at  $c$ .<sup>7</sup> The resultant field wave is a superposition of the applied field wave and a secondary field wave which results from induced dipoles. In linear media, this resultant wave has the same carrier frequency but a different phase. The fact that the frequency is the same is the reason dense transparent materials exist. If the secondary wave lags the applied wave, the resultant wave will also lag. An observer in the medium will have to wait longer for the peaks

of the resultant wave to come past. It is this phase difference which leads to an apparently slower phase velocity. The refractive index represents the cumulative phase difference as the light moves through the medium.<sup>3</sup>

## 2.4 Interaction of Light with Atoms

We have seen in the weak field regime how the linear susceptibility relates to the absorptive and dispersive response of the medium. But we have not yet determined how that susceptibility relates to the properties of the atomic ensemble. Beyond the linear regime, the susceptibility is not a good descriptor for the response of the medium, and analytic expressions for the field propagation are not available. In the nonlinear regime, we will need to follow the dynamics of the atoms to determine how the field will propagate through the medium.

For the dynamics of atom-light interaction to be properly considered the system must be treated as an open quantum system. While the processes of absorption and stimulated emission (of photons from and to the applied field) can be described within a closed quantum system, the process of spontaneous decay due to interaction with vacuum fluctuations surrounding an atom cannot. As such, the time evolution is described by the Lindblad master equation

$$i\hbar \frac{\partial \rho}{\partial t} = [\mathcal{H}, \rho] + \mathcal{L} \{\rho\}. \quad (2.29)$$

The background of this equation and the conditions under which it is valid are discussed in appendix A. It constitutes a set of differential equations to be solved: one for each of the density matrix elements.

### 2.4.1 Spontaneous Decay of Excited States

As described in equation (A.9), coupling to the environment is implemented via the Lindblad superoperator  $\mathcal{L}$  which is completely defined by a finite set of collapse operators. In the case of spontaneous emission due to interaction with vacuum fluctuations, these are defined as

$$C_{ij} = \sqrt{\Gamma_{ij}} |i\rangle \langle j|. \quad (2.30)$$

where  $\Gamma_{ij} = 1/\tau_{ij}$  and  $\tau_{ij}$  is the stochastic rate at which electrons spontaneously decay from a higher state  $|j\rangle$  to a lower state  $|i\rangle$ . The quantity  $\Gamma_{ij}$  is known as the natural linewidth for the specific transition  $|i\rangle \rightarrow |j\rangle$ , for reasons that will be clarified in section 2.5.

### 2.4.2 The Interaction Hamiltonian

A single-electron (or hydrogenic) atom has a positively charged nucleus and a negatively charged electron, both of which will interact with an applied electromagnetic field. At optical wavelengths, however, the interaction with the nucleus is negligible,<sup>8</sup> so we focus our attention on the electron.

Without interaction with an external field, the bare atomic Hamiltonian is given by

$$\mathcal{H}_0 = \frac{\mathbf{p}^2}{2m_e} + V(r) \quad (2.31)$$

where  $m_e$  is the mass of the electron,  $\mathbf{r}$  and  $\mathbf{p} = i\hbar\nabla$  are its position and momentum operators, and  $V(r)$  is the spherical atomic potential.

The non-relativistic Hamiltonian of the electron interacting with an applied classical electric field  $\mathbf{E}$ , in the Coulomb gauge, may be written

$$\mathcal{H} = \mathcal{H}_0 + \mathcal{H}_I \quad (2.32)$$

where the interaction Hamiltonian term  $\mathcal{H}_I$  describes the coupling of the atomic dipole to the field.<sup>8</sup> The problem of the atom-light interaction is then one of calculating the matrix elements of  $\mathcal{H}_I$  as a perturbation to the eigenstate basis of  $\mathcal{H}_0$ .

We will consider a monochromatic field with angular frequency  $\omega$  and wavenumber  $\mathbf{k}$  (the analysis extends to multi-chromatic fields, which we will consider in chapter 3). We may write the field as

$$\mathbf{E}(\mathbf{r}, t) = \hat{\mathbf{x}} \left[ \frac{1}{2} \mathcal{E}(t) e^{i(\mathbf{k} \cdot \mathbf{r} - \omega t)} + \frac{1}{2} \mathcal{E}^*(t) e^{-i(\mathbf{k} \cdot \mathbf{r} - \omega t)} \right] \quad (2.33)$$

where  $\hat{\mathbf{x}}$  is the unit polarisation vector and  $\mathcal{E}(t)$  is the field amplitude.

We simplify calculation of matrix elements by making the exponential expansion

$$e^{i\mathbf{k} \cdot \mathbf{r}} \approx 1 + (i\mathbf{k} \cdot \mathbf{r}) + \frac{1}{2!} (i\mathbf{k} \cdot \mathbf{r})^2 + \dots \quad (2.34)$$

and neglecting all but the first term, unity. This *electric dipole approximation*<sup>9</sup> represents neglecting the spatial dependence of the field over the extent of the atom, and is justified as the electronic wavefunction is on the order of the Bohr radius at  $10^{-10}$  m and the optical carrier wavelength  $\lambda = 2\pi/k$  is on the order of  $10^{-7}$  m. The approximation may equivalently be derived as truncating a multipole expansion of the interaction at the dipole term.<sup>10</sup>

Applying the electric dipole approximation, we may write the interaction Hamiltonian term as

$$\mathcal{H}_I = -e\mathbf{r} \cdot \mathbf{E} = -\mathbf{d} \cdot \mathbf{E} \quad (2.35)$$

where analogous with a classical dipole moment,  $\mathbf{d}$  is the electric dipole operator. And we may take the field out of the spatial integral implicit in calculating the matrix elements between two bare atom eigenstates  $|a\rangle$

and  $|b\rangle$ ,

$$\begin{aligned}\langle a | \mathcal{H}_I | b \rangle &= - \left[ \frac{1}{2} \mathcal{E}(t) e^{-i\omega t} + \frac{1}{2} \mathcal{E}^*(t) e^{i\omega t} \right] \langle a | \hat{\mathbf{x}} \cdot e\mathbf{r} | b \rangle \\ &= - \left[ \frac{1}{2} \mathcal{E}(t) e^{-i\omega t} + \frac{1}{2} \mathcal{E}^*(t) e^{i\omega t} \right] d_{ab}\end{aligned}\quad (2.36)$$

where  $d_{ab}$  is then the matrix element of the electric dipole operator  $\mathbf{d}$  projected on the polarisation direction of the electric field. The crux of the problem is then in calculating (or looking up) dipole matrix elements for the eigenstates of a given system.

#### 2.4.3 Dipole Matrix Elements and Parity

We can show that the diagonal matrix elements of  $\mathbf{d} = e\mathbf{r}$  are zero by making a parity argument. We define the parity operator  $\Pi$  as the unitary operator (i.e.  $\Pi^\dagger \Pi = 1$ ) that flips the sign of the position operator  $\mathbf{r}$  via

$$\Pi \mathbf{r} \Pi^\dagger = -\mathbf{r}. \quad (2.37)$$

Operating with  $\Pi$  on the right of both sides shows that the anticommutator  $\{\Pi, \mathbf{r}\} = \Pi \mathbf{r} + \mathbf{r} \Pi = 0$  and thus the matrix elements vanish

$$\langle i | \{\Pi, \mathbf{r}\} | j \rangle = \langle i | \Pi \mathbf{r} + \mathbf{r} \Pi | j \rangle = 0 \quad (2.38)$$

for any states  $|i\rangle, |j\rangle$ . Now  $\Pi$  commutes with  $\mathcal{H}$ , and so has the same eigenstates, so we have eigenvalues  $\pi_i, \pi_j$  such that  $\Pi |i\rangle = \pi_i |i\rangle$  and  $\Pi |j\rangle = \pi_j |j\rangle$ . Thus we can write

$$\langle i | \Pi \mathbf{r} + \mathbf{r} \Pi | j \rangle = (\pi_i + \pi_j) \langle i | \mathbf{r} | j \rangle. \quad (2.39)$$

The right hand side can only be zero if  $\pi_i + \pi_j$  is zero or if the matrix element is. Now, as  $\Pi^2 = 1$ , the eigenvalues  $\pi = \pm 1$ . So for the diagonal matrix elements,  $\pi_i + \pi_i$  can't be zero and  $\pi_j + \pi_j$  can't be zero so it must be that  $\langle i | \mathbf{r} | i \rangle = \langle j | \mathbf{r} | j \rangle = 0$ . The off-diagonal matrix elements  $\langle i | \mathbf{r} | j \rangle$  are non-vanishing if the states have opposite parity such that  $\pi_i = -\pi_j$ .

### 2.4.4 Atomic Coherence and Polarisation

We introduced the polarisation  $P$  in section 2.2 as the cumulative effect of charge separation induced on individual atoms and defined it in 2.3 as the dipole moment per unit volume. In terms of atomic observables, the polarisation at a distance  $z$  through the medium at time  $t$  may therefore be written as the expectation value of the scalar dipole operator for those atoms

$$P(z, t) = N(z) \langle d(z, t) \rangle \quad (2.40)$$

where  $N(z)$  is the number density (atoms per unit volume) of the medium, which may in general be a function of propagation distance  $z$ , for example in an atom cloud shaped by the geometry of a magneto-optical trap,<sup>11</sup> or constant for a thermal cell in thermal equilibrium.

The expectation value of an observable for a system in a pure or mixed state represented by a density matrix  $\rho$  is defined in equation (A.5), such that we may write

$$P(z, t) = N(z) \text{Tr} [\rho d(z, t)]. \quad (2.41)$$

As we know from the above parity argument that the diagonal matrix elements of the dipole operator are zero, we may then write  $P$  directly in terms of the off-diagonal elements and the atomic coherences, via

$$P(z, t) = N(z) \sum_{i \neq j} [d_{ij}\rho_{ij}(z, t) + d_{ji}\rho_{ji}(z, t)]. \quad (2.42)$$

Now in order to relate this to the slowly-varying envelope  $\mathcal{P}$ , we need to rotate the density matrix elements, via

$$\begin{aligned} \rho_{ij} &= \tilde{\rho}_{ij} e^{i(kz - \omega t)} \\ \rho_{ji} &= \rho_{ij}^* = \tilde{\rho}_{ij}^* e^{-i(kz - \omega t)} \end{aligned}$$

where tilde-notated variables  $\tilde{\rho}_{ij}$  are slowly-varying density matrix elements. Dropping the tilde notation, we then derive an expression for the

slowly-varying polarisation envelope in terms of the atomic coherences

$$\mathcal{P}(z, t) = N(z) \sum_{i \neq j} d_{ij} \rho_{ij}(z, t) \quad (2.43)$$

which we may substitute into the propagation equation (2.13).

Note that in our discussion of polarisation in this section we have made no reference to the susceptibilities  $\chi^{(j)}(t)$ . These are implicit in the density matrix coherences. This analysis is valid for any general nonlinear form of polarisation as expressed in equation (2.15) if we can determine the evolution of atomic states from the Lindblad equation (2.29).

#### 2.4.5 Thermal Atoms

The above analysis for the atom-light interaction is appropriate for stationary (*i.e.* ultracold) atoms but must be modified for thermal atoms due to the averaging effect of atomic motion.<sup>12</sup>

An atom moving with a velocity component  $v$  in the  $z$ -direction will interact with a Doppler-shifted field frequency  $\omega - kv$ . This shift is effected over a 1D Maxwell-Boltzmann probability distribution function of velocity<sup>13, 14</sup>

$$f(v) = \frac{1}{u\sqrt{\pi}} e^{-(kv/u)^2} \quad (2.44)$$

where the thermal width  $u = kv_w$ . Here  $k$  is again the wavenumber of the quasi-monochromatic field and  $v_w = 2k_B T / m$  is the most probable speed of the Maxwell-Boltzmann distribution for a temperature  $T$  and atomic mass  $m$ . As is usual,  $k_B$  represents the Boltzmann constant.

To include this Doppler effect in the field propagation equations (2.13), we replace the atomic coherence factor by an integral over a convolution of  $f(v)$ , with the atomic coherence now a function of velocity, so that

$$\mathcal{P}(z, t) = N \sum_{i \neq j} d_{ij} \int_{-\infty}^{\infty} \rho_{ij}(z, t; v) f(v) dv. \quad (2.45)$$

This velocity-dependent  $\rho_{ij}(z, t; v)$  represents the atomic coherence resulting from interaction with a field at the Doppler-shifted frequency  $\omega - kv$ .

The result of the inclusion of thermal effects is a broadening of absorption resonance widths, a familiar concern in spectroscopy. We will consider example spectral profiles in section 2.5.

#### 2.4.6 Shifting to the Speed-of-Light Reference Frame

To solve the propagation equation (2.13) as a boundary value problem, it is useful to introduce co-moving variables  $\zeta = z$  and  $t' = t - z/c$ . This is equivalent to using a reference frame that moves with the speed of light across the medium.<sup>12</sup> We then have

$$\frac{\partial}{\partial \zeta} = \frac{\partial z}{\partial \zeta} \frac{\partial}{\partial z} + \frac{\partial t}{\partial \zeta} \frac{\partial}{\partial t} = \frac{\partial}{\partial z} + \frac{1}{c} \frac{\partial}{\partial t} \quad (2.46)$$

so that

$$\frac{\partial}{\partial z} \mathcal{E}(z, t') = i \frac{k}{2\epsilon_0} N(z) \sum_{i \neq j} d_{ij} \int_{-\infty}^{\infty} \rho_{ij}(z, t; v) f(v) dv. \quad (2.47)$$

In this reference frame we see that the propagation equation for the field is now a differential equation only in  $z$ .

#### 2.4.7 A Recap

At this point we have derived a set of coupled partial differential equations describing the dynamics of the atomic density operator (2.29) and the propagation of the electric field envelope (2.47).

These coupled equations can be integrated numerically for a given set of boundary conditions defining the input profile of the electric field and the initial state of the atoms. The integration proceeds via the following recipe, which must be repeated in a self-consistent manner:

1. Solve the Lindblad master equation for the quantal dynamics of the atomic density matrix over time  $t'$ .
2. Average the Maxwell-Boltzmann probability distribution over velocity  $v$ .
3. Solve the Maxwell wave equations for propagation of the electro-magnetic field over space  $z$ .

The description of the specific numerical algorithms used for integration, along with details of the Python code used to implement these algorithms, is given in appendices B and C. We will make use of these methods to solve the MB equations for various systems of interest throughout the chapters of this thesis.

## 2.5 Linear Propagation in Two-level Atoms

Now that we have derived the necessary differential equations to describe 1D propagation in an atomic vapour and described computational algorithms for the numerical solution of the problem for a given set of boundary conditions, we will look at example results from simulated propagation of a monochromatic (*i.e.* single carrier frequency) field in a simple two-level system.

We will define the two-level system and present the results of propagation for some boundary conditions representative of laboratory experiments: pulsed and continuous-wave (cw) input fields. We'll then make an analysis of the frequency dependent behaviour of the simulated propagation of a wider-spectrum field. We will use these results to verify that these results match the known analytic response functions for the linear regime, such that we have confidence in the computational

scheme for the simulations we will later obtain for nonlinear systems with more than one carrier frequency.

We will also introduce the natural unit system which will be used throughout this thesis.

### 2.5.1 The Two-level System

No real atomic system exists with only two levels of course, but this minimal scheme is a good approximation in the case of resonant interaction with a well-separated transition.

The system is defined by a Hilbert space covered by a basis that consists of a ground state  $|0\rangle$  and an excited state  $|1\rangle$  with eigenenergies  $E_0$  and  $E_1$ . The resonance frequency  $\omega_0 = (E_1 - E_0)/\hbar$ . As is conventional we define the detuning of the input carrier frequency from resonance as  $\Delta = \omega - \omega_0$  and the complex Rabi frequency<sup>15</sup>

$$\Omega(z, t) = \frac{d_{01}}{\hbar} \mathcal{E}(z, t) \quad (2.48)$$

where  $d_{01} = \langle 0 | d | 1 \rangle$  is the transition dipole matrix element.

The time evolution is independent of the absolute value of the bare state energies, so we may set the ground state energy  $E_0 = 0$ . Making the rotating wave approximation, we find that the atomic Hamiltonian is given by

$$\mathcal{H} = \hbar \begin{bmatrix} 0 & \Omega/2 \\ \Omega^*/2 & -\Delta \end{bmatrix} \quad (2.49)$$

in the frame rotating with the carrier frequency.<sup>16</sup>

For the Lindblad superoperator  $\mathcal{L}$  we have just a single collapse operator representing spontaneous decay of the electron from the the excited state to the ground state

$$C = \sqrt{\Gamma} |0\rangle\langle 1|. \quad (2.50)$$

In two-level medium we only have one dipole matrix element and one coherence to consider, such that (neglecting the Doppler effect for now) the propagation equation (2.47) may be written

$$\frac{\partial}{\partial z} \mathcal{E}(z, t') = iN(z) \frac{k}{2\epsilon_0} d_{01} \cdot \rho_{01}(z, t'). \quad (2.51)$$

It is useful to write the propagation now in terms of the Rabi frequency

$$\frac{\partial}{\partial z} \Omega(z, t') = iN(z) g \cdot \rho_{01}(z, t') \quad (2.52)$$

where we define a propagation coefficient

$$g_{01} = \frac{d_{01}^2 k}{2\epsilon_0 \hbar} \quad (2.53)$$

which is constant for a given transition with dipole matrix element  $d_{01}$  and for a field with carrier wavenumber  $k$ .

### 2.5.2 The Natural Unit System

For a two-level system we have a single natural linewidth, and so it is convenient to introduce a natural unit system, with frequencies in units of the natural linewidth  $\Gamma$ , times in terms of the reciprocal spontaneous decay lifetime  $\tau = 1/\Gamma$  and distances in terms of the length of the medium  $L$ .

To give an illustrative example, we will take a rubidium 85 cell and apply a monochromatic field on resonance with the D1 transition from the  $5^2S_{1/2}$  ground state to the  $5^2P_{1/2}$  excited state at  $\omega = 2\pi \times 377$  THz. The spontaneous decay rate for the transition  $\Gamma = 2\pi \times 5.75$  MHz such that the lifetime  $\tau = 27.6$  ns. The transition dipole matrix element is  $d_{01} = 2.53 \cdot 10^{-29}$  C m. From this we can calculate that the propagation coefficient for the transition  $g_{01} = 2\pi \times 4.34 \cdot 10^{-9}$  MHz cm<sup>2</sup>.

The number density  $N$  in a contained cell is a function of the temperature of the cell. For an example temperature  $T = 200$  C we have  $N =$

$9.26 \cdot 10^{14} \text{ cm}^{-3}$ . If we then take a cell of a typical length  $L = 1 \text{ mm}$ , the key parameter we require for describing propagation in the medium can be expressed purely in terms of the natural units as  $N g_{01} = 2\pi \times 70 \Gamma / L$ .

By introducing this natural unit system we are able to reduce the number of parameters involved in the mathematical problem. For example, it becomes clear that increasing the length of the medium ten times is equivalent to raising the number density by the same scale, or by choosing a system with a suitably higher dipole moment.

### 2.5.3 Weak Probe Lineshape

The Lindblad master equation (2.29) represents a set of differential equations in time for the time evolution of each density matrix element.

As we know via equation (2.43) that the polarisation  $\mathcal{P}$  is related to the off-diagonal coherence  $\rho_{01}$ , we write out the particular equation to follow its time evolution, such that

$$\frac{d\rho}{dt} = i\Omega(\rho_{00} - \rho_{11}) + \left(i\Delta - \frac{\Gamma}{2}\right)\rho_{10}. \quad (2.54)$$

In the case of weak field input on the medium, we may assume that we're in a quasi-static regime where the atomic density matrix changes negligibly over the time of the input. We thus set the time derivative in equation (2.54) to zero.

The initial condition is that all of the atomic population starts in the ground state. For a weak field we may also assume that population transfer is negligible such that  $\rho_{11} = 0$ .

Under these weak field approximations, we may thus derive the steady state, weak field lineshape

$$\rho_{01}(z) = -\Omega(z) \frac{1}{i\frac{\Gamma}{2} + \Delta}. \quad (2.55)$$

### 2.5.4 Weak Pulse Propagation Results

The first Maxwell-Bloch simulation results we will consider are for an input field profile of finite duration, namely a Gaussian pulse. In general for short duration pulses, the atoms do not reach equilibrium with the applied field before the pulse has passed, however for weak fields so little population is transferred that a quasi-static regime can be a good approximation.

The Gaussian pulsed input field is defined by

$$\Omega(t) = \Omega_0 \exp \left[ -4 \log 2 \left( \frac{t - t_0}{t_w} \right) \right] \quad (2.56)$$

where  $\Omega_0$  is the peak input Rabi frequency,  $t_0$  is the time at which the function reaches that peak, and  $t_w$  is the full width at half maximum (FWHM) of the pulse.

In this simulation we let the peak  $\Omega_0 = 2\pi \times 10^{-3} \Gamma$ , the centre  $t_0 = 0$  and the width  $t_w = 0.1 \tau$ . We define the medium to have a length  $L$ , number density  $N$  and coupling  $g$  such that the key absorption parameter  $Ng = 2\pi \times 1 \Gamma/L$ .

In figure 2.1 we present a colour map of the simulated real part of the complex Rabi frequency  $\Omega(z, t)$  describing the field profile as it propagates through the medium.

Time  $t$  is shown on the  $x$ -axis and the propagation distance  $z$  is shown on the  $y$ -axis such that the field enters at the bottom of the plot. The horizontal slice at  $z = 0$  thus represents the Gaussian input field. All propagation results are presented in the speed-of-light reference frame described in section 2.4.

We see that the primary pulse envelope is attenuated and slightly fast, such that the first peak arrives at the rear of the medium,  $z = 1L$ , at a time  $t \approx -0.05 \tau$  in the speed-of-light reference frame. [normal disper-

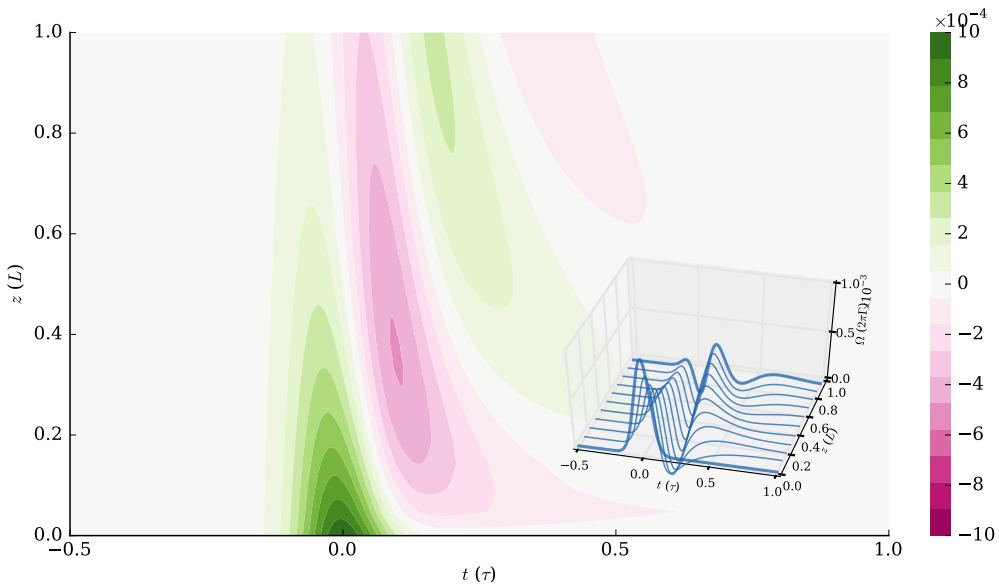


FIGURE 2.1 The real part of the complex Rabi frequency  $\Omega(z, t)$  showing the simulated result of propagation of a weak pulse through a two-level medium. (Inset 3D) The field has Gaussian profile entering the medium at  $z = 0$ , with peak  $\Omega_0 = 2\pi \times 10^{-3} \Gamma$  and width  $t_w = 0.1 \tau$ .

sion profile]. Not all of the energy of the pulse is absorbed, however. This is because the pulse is short in duration relative to  $\tau$ , such that its spectral profile is wider in frequency space than the absorption window of the atoms. Thus some spectral components of the field see a medium which is transparent to them. However, they remain subject to phase shift. We see high-frequency ringing, also described as a  $0\pi$  pulse as the total area integrates to zero.<sup>16, 17</sup>

In figure 2.2 we present colour maps of simulated density matrix elements describing the response of the atoms along the medium as the applied field reaches them.

The cumulative Rabi frequency of the pulse is many orders of magnitude too small to saturate the excited state population so that for the atoms at the front of the medium at  $z = 0$ ,  $\rho_{11}$  continues to rise through the pulse to a peak at time  $t \approx 0.01 \tau$  after the input field has peaked. There is a small ‘echo’ in the excited state, due to the field ringing, visi-

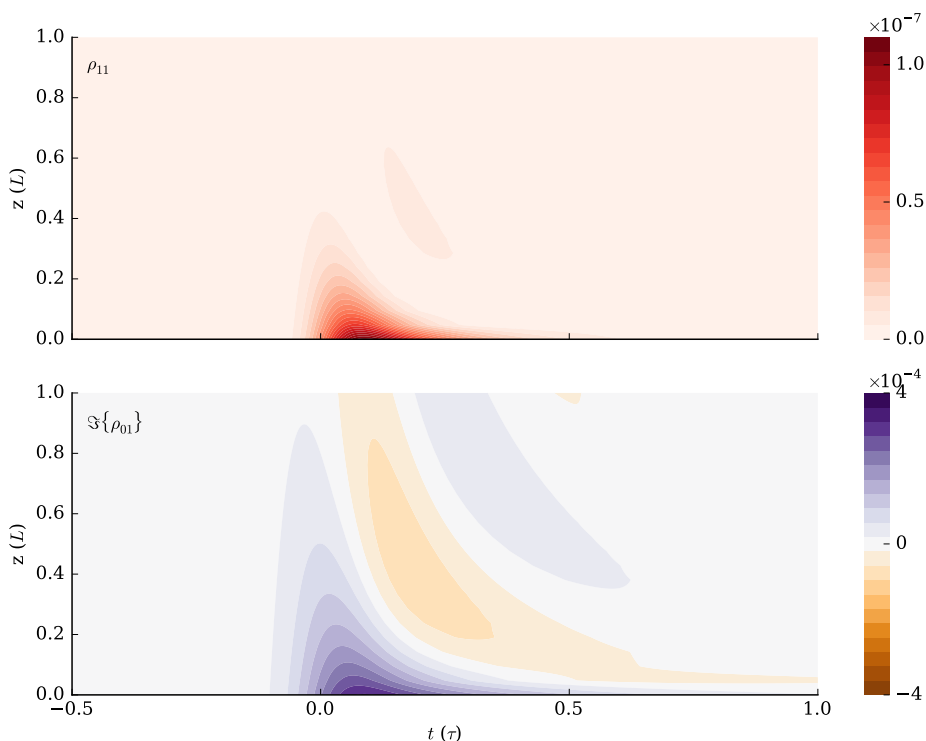


FIGURE 2.2 Density matrix elements of the two-level atom system as a function of  $z$  and  $t$  during the simulation. (Top) Excited state population  $\rho_{11}(z, t)$ . (Bottom) Coherence  $\rho_{01}(z, t)$  between the states. The simulation parameters and boundary conditions are as for figure 2.1.

ble at  $t \approx 0.2\tau$  and between  $z = 0.4L$  and  $0.6L$ .

A positive imaginary coherence  $\Im[\rho_{01}]$  is driven by the applied field at the front of the medium. We observe that the coherence decays at half the rate of the excited state population,  $\Gamma/2$ , consistent with equation (2.54).

### 2.5.5 Spectral Analysis

In section 2.3 we made use of Fourier transforms to shift perspective to the frequency domain. We showed that in the linear regime it is possible to derive a response function, given in equation (2.22), which when substituted into the propagation equation allows us to understand how the susceptibility describes the frequency-dependent absorptive and dispersive properties of a medium with respect to a weak field.

In order to verify the numerical model we have developed, as well as to demonstrate these spectral properties, we will now look at results from a simulation of a pulse propagating through the two-level medium. We wish to confirm that the results of the simulation match the known analytic response functions for the linear regime.

For this simulation we define an unusual and artificial time profile for the input field boundary condition: a cardinal sine (sinc) function given by

$$\Omega(t) = \frac{1}{20\sqrt{2\pi}} \text{sinc}(10t). \quad (2.57)$$

This input profile, shown in the top subplot of figure 2.3, is clearly impractical for any experimental setup. We choose this profile because its Fourier transform, shown in the bottom subplot of figure 2.3, is a square function with a width of  $10\Gamma$ . This gives us a wide spectral range over which to observe the effect of the two-level medium on the field.

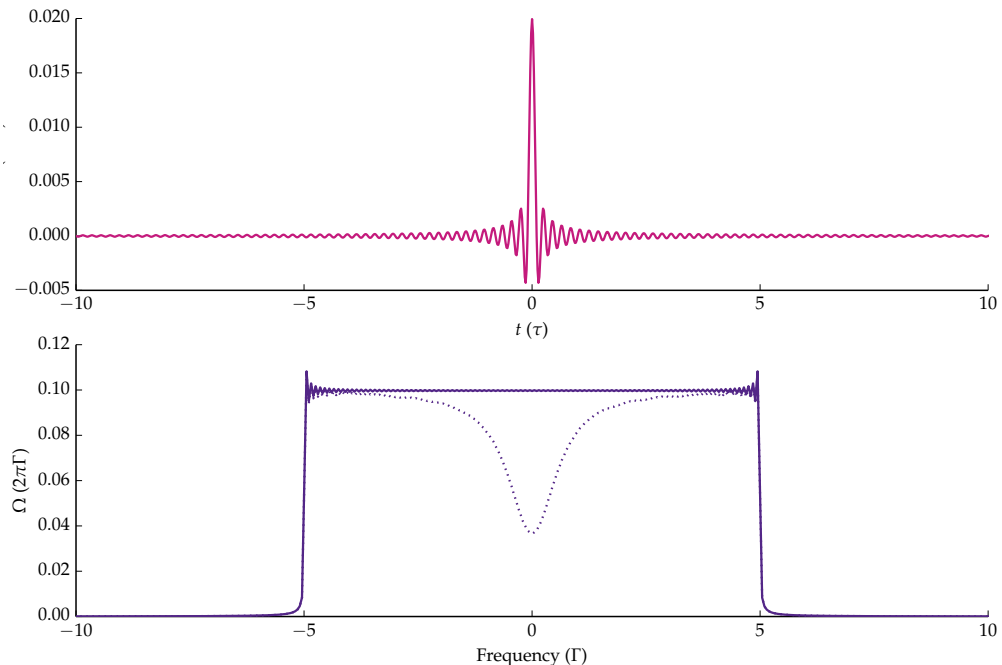


FIGURE 2.3 (Top) The sinc function (pink) defined by equation (2.57) which forms a simulated pulse profile in time  $\Omega(t, 0)$  entering the medium at  $z = 0$ , *i.e.* the boundary condition. (Bottom) (Purple solid) The discrete Fourier transform  $|\Omega(\omega, 0)|$  of the sinc shape above, representing the same function in the frequency domain at  $z = 0$ . (Purple dotted) The resulting field profile  $|\Omega(\omega, z = 1)|$  in the frequency domain at  $z = 1 L$ , after propagation through the medium. The medium is defined with a length  $L$ , number density  $N$  and coupling  $g$  such that  $Ng = 2\pi 1 \Gamma / L$ .

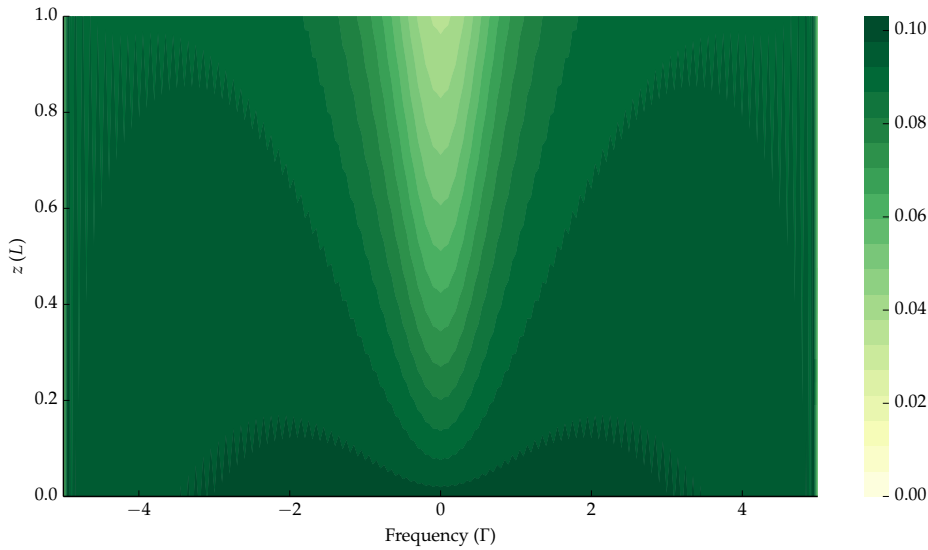


FIGURE 2.4 Magnitude of the Fourier-transformed Rabi frequency  $|\Omega(z, \omega)|$ , showing propagation of the field through the medium in the frequency domain during the simulation. The input boundary condition field profile at  $z = 0$  is the sinc function shown in figure 2.3. The medium is defined with a length  $L$  and number density  $N$  such that  $Ng = 2\pi 1\Gamma/L$ .

The discrete Fourier transform (DFT) is used as the numerical method for shifting to the frequency domain, which results in some Gibbs ringing<sup>18</sup> seen at the corners at  $\pm 5\Gamma$ .

A more-realistic Gaussian time profile, short in duration, would also cover a wide spectral range. We choose the sinc function for the reason that it provides greater accuracy in the wings far away from resonance, where both the input and output field amplitudes would be extremely small for the Gaussian function, bringing inaccuracy as we get close to limits for floating point storage.

The absorptive effect of the medium is immediately visible if we compare the  $|\Omega(\omega, z=1)|$ , the profile at the back of the medium, also shown (dotted) in the bottom subplot of figure 2.3. Around resonance there is a significant dip of around 60% in the transmitted Rabi frequency (and thus the electric field amplitude).

In figure 2.4 we show the results for  $|\Omega(\omega, z)|$  as the sinc pulse moves through the medium. On resonance, the field decays exponentially while in the spectral wings we see nearly full transmission.

We can compare the simulated result with the analytic expression given in equation (2.25), which tells us that we can obtain the imaginary part of the susceptibility by checking the attenuation of the field via

$$\frac{k}{2}\chi_I(\omega)z = -\log \frac{|\Omega(z, \omega)|}{|\Omega(z = 0, \omega)|} \quad (2.58)$$

and the real part of the susceptibility by checking the phase shift over the medium,

$$\frac{k}{2}\chi_I(\omega)z = \phi(z, \omega) - \phi(z = 0, \omega) \quad (2.59)$$

where the  $\phi$  is defined via

$$\Omega(z, \omega) = |\Omega|e^{i\phi}. \quad (2.60)$$

In figure 2.5 we present the simulated results for the susceptibility as defined in (2.58) and (2.59).

We see that the imaginary part, describing absorption of the field, has the Lorentzian lineshape familiar as a solution for classical systems involving forced and damped resonance. The FWHM is measured numerically, and as we would expect it is equal to  $1\Gamma$ , the natural linewidth around which we designed the natural unit system.

Absorption linewidths observed in experiment will in general be significantly wider, as the important effects of Doppler broadening and atomic collisions must be considered. This natural linewidth represents the theoretical minimum linewidth that could be observed for cold atoms due to spontaneous emission rate, which for an atom in free space can never be reduced.<sup>15</sup>

The real component has the familiar dispersion lineshape describing the

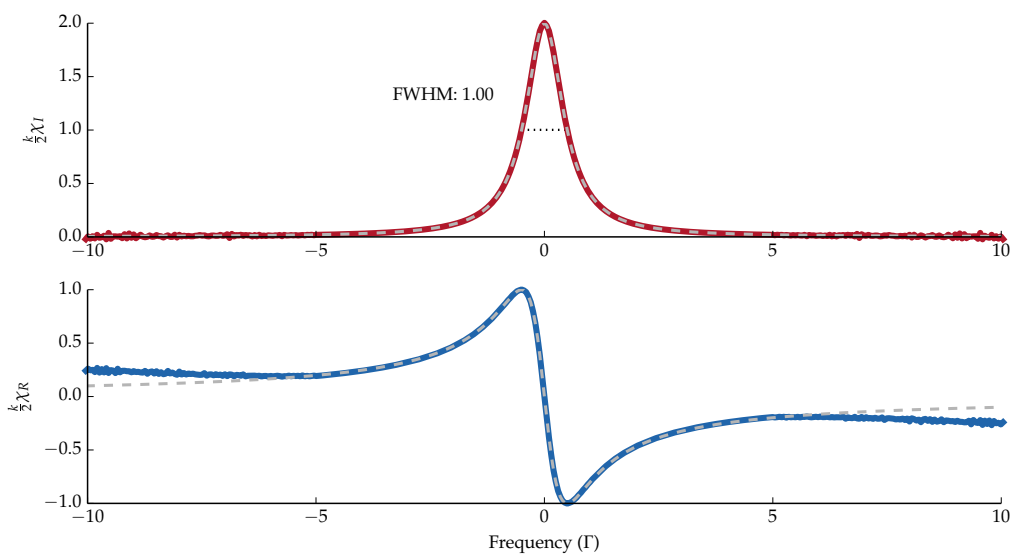


FIGURE 2.5 (Top) (red solid) The imaginary part of the linear susceptibility  $\chi_I$  derived from the simulation via equation (2.58). (Bottom) (blue solid) The real part of the linear susceptibility  $\chi_R$  derived from the simulation via equation (2.59). (grey dashed) Analytic functions of  $\chi_I$  and  $\chi_R$  derived from the weak probe lineshape given in equation (2.61). The FWHM of the  $\chi_I$  lineshape is shown as measured numerically.

phase of the input field relative to the frequency of the oscillator as it passes over resonance from lagging to leading.<sup>3</sup>

By comparing the linear propagation equation (2.23) with the weak probe approximation for the coherence, given in equation (2.55), we note that we can also derive an analytic expression for the frequency-dependent susceptibility in this regime,

$$\frac{k}{2}\chi(\omega) = -Ng\frac{1}{i\frac{\Gamma}{2} + \Delta}. \quad (2.61)$$

The real and imaginary parts of this function are overlaid (grey dashed lines) on the simulated results and we see excellent agreement around resonance. We see in (2.61) that the imaginary part of the susceptibility, and thus the absorption, is solely due to the spontaneous decay term  $\Gamma$ . This we can understand as it is this scattering of energy by the atoms to the environment which results in a loss of energy in the system.

Spectral field components beyond  $\pm 5\Gamma$  are negligible (as defined by the sinc function, see figure 2.3) and so we see some noise in the result beyond this point. We also see deviation between the analytic and simulated results in the dispersion profile far from resonance, which is due to the linear susceptibility approximation being valid only for near-resonant components of the field.

This result tells us that the computational scheme designed to model propagation of light in atomic media is accurate in the linear regime, which gives us confidence in the scheme for the work we will do later going beyond this weak field limit.

In the scope of input field boundary conditions, at the other extreme to short duration, wide-spectral pulses are continuous wave (cw) fields, with constant intensity over time. Such field envelopes are monochromatic, meaning that the frequency domain representation of a cw field in the time domain is a Dirac delta function.

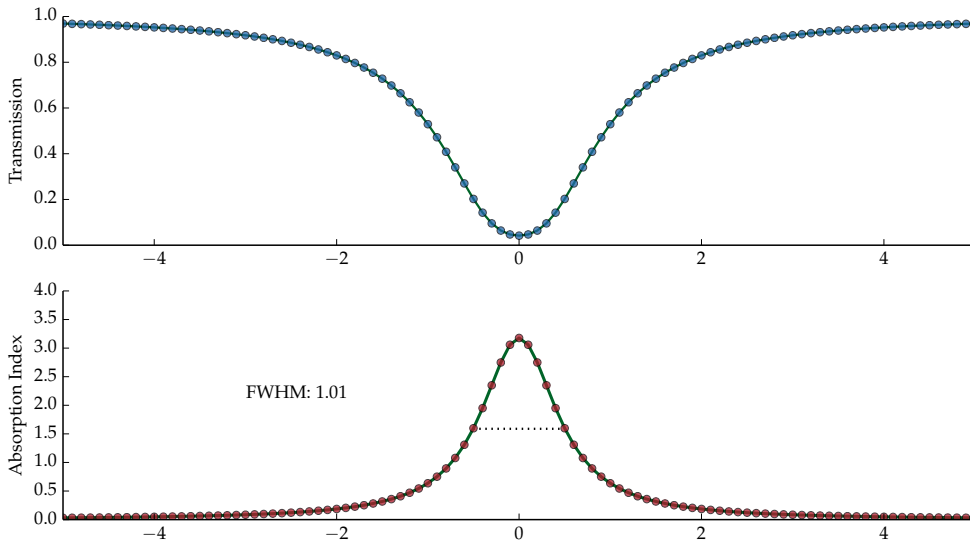


FIGURE 2.6 Peak transmission (top) and absorptive index (bottom) for a monochromatic cw field across a discrete range of 100 detunings  $\Delta$  around resonance. The solid lines in both represent the same values for the continuous spectrum deriving from propagation of the short sinc pulse function.

In figure 2.6 we make a scan of the field detuning  $\Delta$  across resonance with the two-level atom, and mark the peak transmission ( $T = I/I_0$ ) of the field along with the associated absorptive index.

We also plot the transmission and absorption index of the transmission and absorption as a function of frequency for the wide-spectrum sinc pulse. The close agreement tells us that the short pulse's propagation is as if it were composed of many monochromatic frequency components interacting independently with the medium. In the linear regime, the solution is a superposition of individual frequencies.<sup>2</sup>

### 2.5.6 The Voigt Profile

As mentioned, the lineshapes presented thus far for weak probe spectra neglect the thermal motion of the atoms, and so are only valid for atoms that are stationary, *i.e.* close to absolute zero.

To account for thermal atoms, we must include the Doppler effect by means of the average over detunings described by the integral in equation 2.45. The thermal lineshape function may then be expressed as

$$s(\Delta) = \int_{-\infty}^{\infty} h(\Delta - kv) \times f(v) dv \quad (2.62)$$

where the weak probe natural lineshape

$$h(\Delta) = -Ng \frac{1}{i\frac{\Gamma}{2} + \Delta} \quad (2.63)$$

is given in equation (2.61) and  $f(v)$  is the Maxwell- Boltzmann distribution over atomic velocities  $v$  given in equation (6.4).

Using the convolution theorem for Fourier transforms, this integral can be computed as

$$s(\Delta) = \frac{i\sqrt{\pi}}{2u} e^{-z^2} \times \text{erfc}(-iz) \quad (2.64)$$

where  $z = ia/2 + b$  given  $a = \Gamma/u$  and  $b = \Delta/u$ , and  $\text{erfc}$  is the complementary error function.<sup>19</sup> This convolution of a Lorentzian function with a Gaussian function is known as a Voigt profile.

In figure we show simulated results for the real and imaginary parts of the susceptibility for the same system as in figure 2.5, but this time including Doppler effects in the numerical algorithm by a weighted averaging over a range of velocity classes as described in appendix C. We take the thermal width to be  $u = 2\pi \times 0.5 \Gamma$ . As an example, this might correspond to a  $\sim 0.1$  mK vapour of  $^{85}\text{Rb}$  probed on the D1 line.

We compare these simulated lineshapes with the weak probe Voigt profile given in equation (2.64) and see agreement with the analytic result. We see that the inclusion of temperature in the model has the effect of broadening the spectral lineshapes.

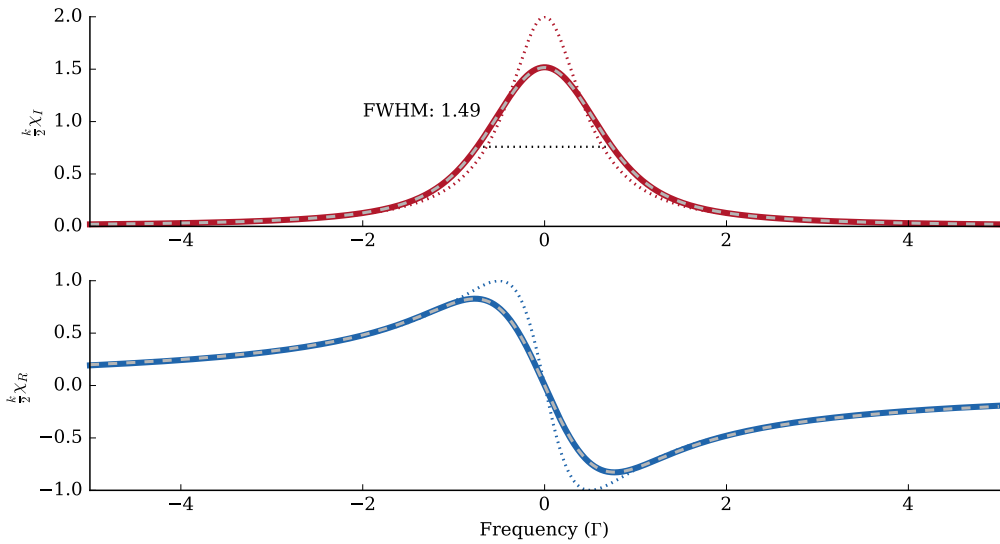


FIGURE 2.7 Top) The imaginary part of the linear susceptibility  $\chi_I$  derived from a thermal simulation via equation (2.58). (Bottom) (blue solid) The real part of the linear susceptibility  $\chi_R$  derived via equation (2.59). (grey dashed) Analytic functions of  $\chi_I$  and  $\chi_R$  derived from the convoluted Voigt profile given in equation (2.64).

## 2.6 Discussion

In this chapter we started from the Maxwell equations and derived a propagation equation for monochromatic light, using the slowly varying envelope approximation. We introduced the linear and nonlinear optics, and for the linear regime, for weak fields, the useful concept of susceptibility and how this relates to the absorptive and dispersive response of the medium.

Going beyond the linear regime, we need to follow the quantal dynamics of the atomic density matrix, which we do with the Lindblad master equation. We defined the interaction Hamiltonian within the electric dipole approximation, and how the polarisation of the medium can be derived from atomic coherences. For thermal atoms this coherence must be averaged over a Maxwell-Boltzmann distribution. We discussed algo-

rithms (presented in appendix C) for integrating the propagation equations numerically for nonlinear propagation.

We presented results for a two-level system in the linear regime. In doing so we used spectral analysis to compare with the analytic results derived in this regime. The good agreement in these results gives us confidence in the numerical methods. In the next chapter, we will employ the model in considering nonlinear pulse propagation in two-level and three-level systems.

# 3 Nonlinear Propagation Phenomena

## 3.1 Introduction

In chapter 2 we introduced a model of the propagation of light through a thermal atomic vapour, based on the Maxwell-Bloch equations. We presented analytic solutions of those equations in the linear regime of a weak applied field, and introduced computational methods (described in appendix C) to solve the equations beyond the weak field approximations.

In this chapter, we will take the model beyond the weak probe and into the nonlinear regime, demonstrating some of the effects that emerge from the interaction of thermal atomic vapours with strong applied fields: notably *self-induced transparency*. We will also introduce light propagation in three-level atoms, which has been found to result in a variety of interesting phenomena due to the existence of *dark* superposition states.

Putting these together in the final section, we will look at strong applied fields in three-level atoms leading to propagation of *matched pulses* and *simultons*.

## 3.2 Self-Induced Transparency & Optical Solitons in Two-Level Atoms

In chapter 2 we made first use of the Maxwell-Bloch propagation model to consider weak pulses of light incident on a medium of two-level atoms, and saw that it is possible to derive analytic solutions to these problems. Once we go beyond this linear regime, the approximations made in deriving those weak field solutions are not available, so in general the problem of nonlinear propagation must be solved numerically.

There exists another set of conditions, however, that has proved susceptible to analytic description, and that is the case of short, strong pulses of light. By ‘short’ here we specifically mean that the duration of the pulses is much shorter than the natural decay lifetime of the excited state, i.e.  $\tau_w \ll \tau_T$ . Strong, resonant interaction with light on this timescale results in a response from the atoms that is definitively non-classical, as the interaction all happens within the phase memory of the atoms such that quantum-mechanical coherence is critical to understanding the propagation behaviour.

Neglecting damping in this way, it must be the case that the total energy of the macroscopic atom-light system is a conserved quantity. We can express this conservation as

$$\left[ \frac{\partial}{\partial z} + \frac{1}{c} \frac{\partial}{\partial t} \right] |\mathcal{E}|^2 + \frac{\partial U}{\partial t} = 0 \quad (3.1)$$

where  $U$  is the matter energy density given by<sup>16</sup>

$$U = N \frac{\hbar \omega}{2} \int_{-\infty}^{\infty} \rho_{11} f(\Delta) d\Delta. \quad (3.2)$$

We must also have conservation of probability in the density matrix, such that

$$\text{Tr} [\rho] = \rho_{00} + \rho_{11} = 1 \quad (3.3)$$

and it is this conservation law that distinguishes the semiclassical propagation model from any classical theory, with saturation of excitation inherent in two-level atoms that can store energy only of  $\hbar\omega_0$ . The phenomena of self-induced transparency (SIT) we shall discuss in this section is one interesting result of such saturation effects.

### 3.2.1 The Area Theorem

A central tool for describing the propagation of short, strong pulses is the nonlinear *area theorem*.<sup>20</sup> The concept of the pulse area generalises the Rabi frequency from steady fields such that it is useful for the description of time-dependent field envelopes. We define the pulse area by

$$\theta(z) = \int_{-\infty}^{\infty} \Omega(z, \tau) d\tau \quad (3.4)$$

where  $\Omega(z, \tau)$  as before is the Rabi frequency envelope of the pulse.

Inserting this definition for  $\theta(z)$  into the expression we derived for the time-evolution of the electric field envelope ([REF]) and taking the analytic expression for Rabi oscillation of the atomic coherence  $\rho_{01}$  on resonance [REF], it is possible to derive an expression for the evolution of the pulse area as the pulse propagates through the medium

$$\frac{\partial}{\partial z} \theta(z) = -\frac{\alpha}{2} \sin \theta(z) \quad (3.5)$$

where  $\alpha$  is the resonant absorption coefficient defined in equation (2.26).

In the case of weak fields such that  $\theta(z) \ll 1$  we may approximate  $\sin \theta(z) = \theta$  and obtain the Beer absorption law, which we thus see is generalised by the area theorem. [TODO FIX REFS]

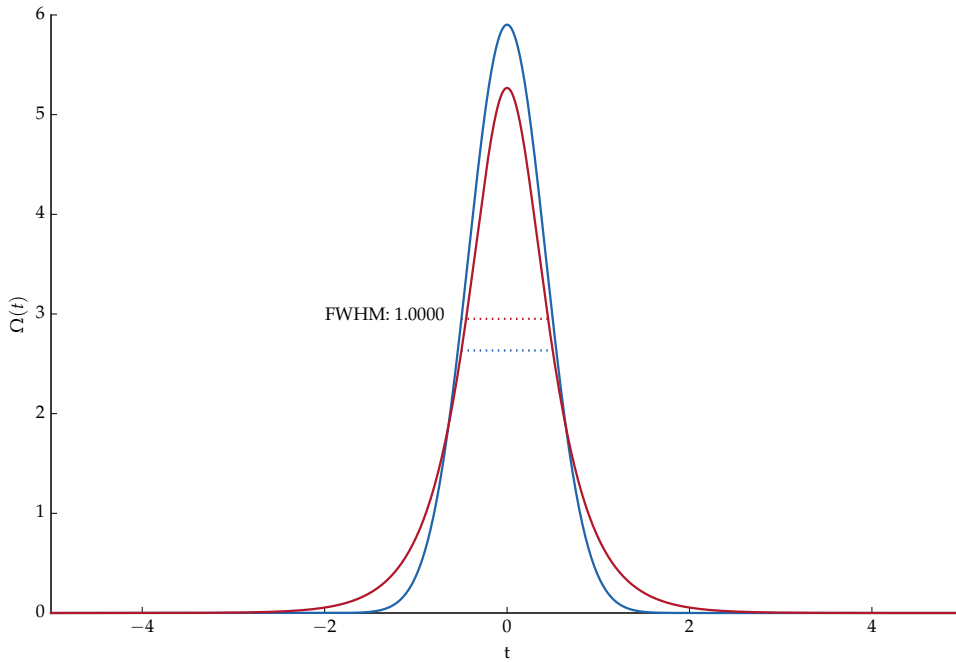


FIGURE 3.1 The hyperbolic secant function (red) expressed in equation (3.6) and Gaussian (blue) expressed in equation (2.56). Both have pulse area  $\theta = 2\pi$  and FWHM  $\tau_w = 1.0$ . The FWHMs are indicated with dotted lines.

### 3.2.2 Self-Induced Transparency

Now looking at the case of a pulse of light with a time-dependent profile such that  $\theta(z) = 2\pi$ , we see that equation (3.5) tells us  $\partial\theta/\partial z = 0$ , i.e. that the area of the pulse will remain constant.

This suggests that it is possible for some form of  $2\pi$  pulse to travel through the medium without attenuation. This indeed turns out to be the case if the envelope profile is such that the Bloch vector is rotated along a specific trajectory, effected by a hyperbolic secant profile

$$\Omega_{2\pi}(z, \tau) = \frac{2}{\tau_s} \operatorname{sech} \left( \frac{\tau - z/v_g}{\tau_s} \right) \quad (3.6)$$

where  $\tau_s$  defines the width of the pulse and  $v_g$  is the group velocity.

In figure 3.1 we show the hyperbolic secant function expressed in equation (3.6) and compare it with the familiar Gaussian profile of equation

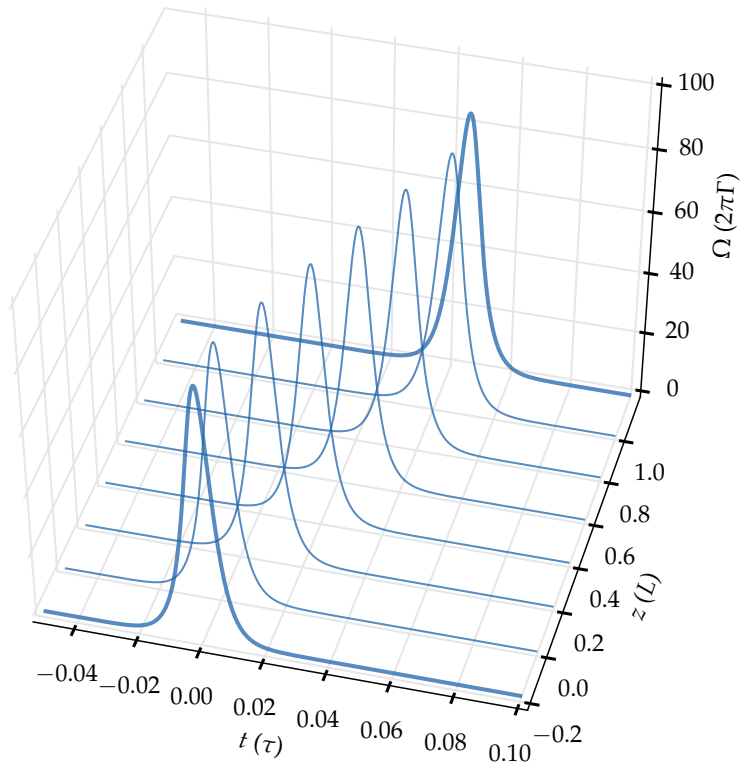


FIGURE 3.2 Simulated absolute value of the complex Rabi frequency  $\Omega(z, \tau)$  for the propagation of a  $\theta = 2\pi$  sech pulse of FWHM  $\tau_w = 0.01 \tau_T$  through a medium with constant density such that  $Ng = 2\pi 10^3 \Gamma/L$ .

(2.56) of the same pulse area  $\theta = 2\pi$  and FWHM  $\tau_w = 1.0$ . We see that these functions are similar but that the sech function has a smaller peak amplitude and larger wings. We determine numerically that the FWHM is related to the sech-width  $\tau_s$  via  $\tau_s \approx 2.633916 \tau_w$ .

The group velocity, relative to the speed-of-light reference frame, is given by

$$v_g = \frac{2}{Ng \cdot t_s^2} \quad (3.7)$$

which means that the exit of the envelope from the medium is delayed relative to an equal travel distance in vacuo by  $L/v_g$ .

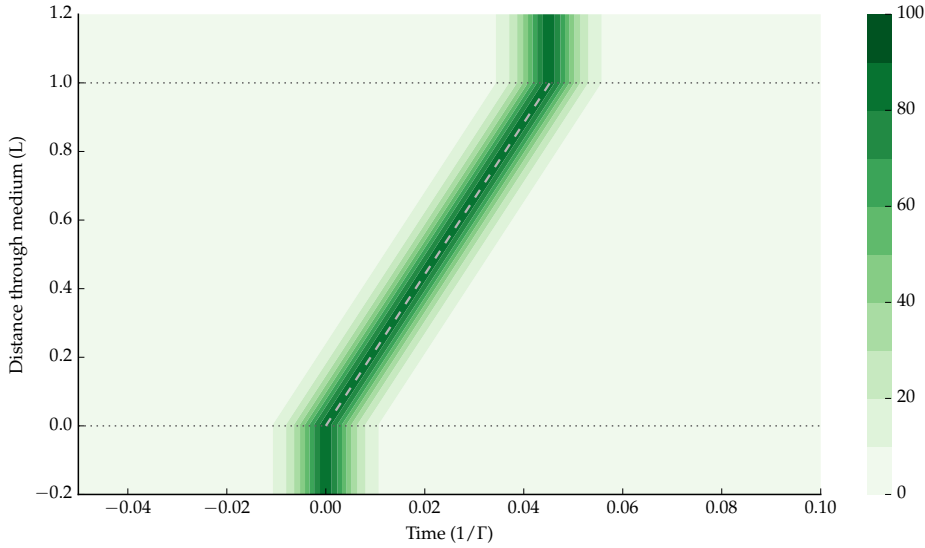


FIGURE 3.3 Colormap showing the same simulated results shown in figure 3.2. The dotted lines at  $z = 0, 1 L$  mark the start and end of the medium. The dashed line indicates the analytic pulse velocity given in equation (3.7).

In figure 3.2 we show the results of a simulation, again using the numerical scheme defined in appendix C, of the absolute part of the Rabi frequency  $\Omega(z, \tau)$  for the propagation of a  $\theta = 2\pi$  sech pulse through a medium of two-level atoms. The pulse has a FWHM  $\tau_w = 0.01 \tau_\Gamma$  and the medium is defined such that  $Ng = 2\pi 10^3 \Gamma/L$ .

We see that the  $2\pi$  pulse retains its profile through the medium, but is delayed by  $\approx 0.05 \tau_\Gamma$ . Recall that in the speed-of-light reference frame shown in these figures, a pulse of light in vacuo arrives at the same time it left.

In figure 3.3 we show the same result as a colour map, from which we can more clearly see both the consistency of the pulse profile as it propagates through the medium and the slower group velocity. The analytic pulse velocity, given in equation (3.7), is shown by the dotted line, and we see that the pulse peak matches that result.

We can understand the reason the pulse is able to travel without attenu-

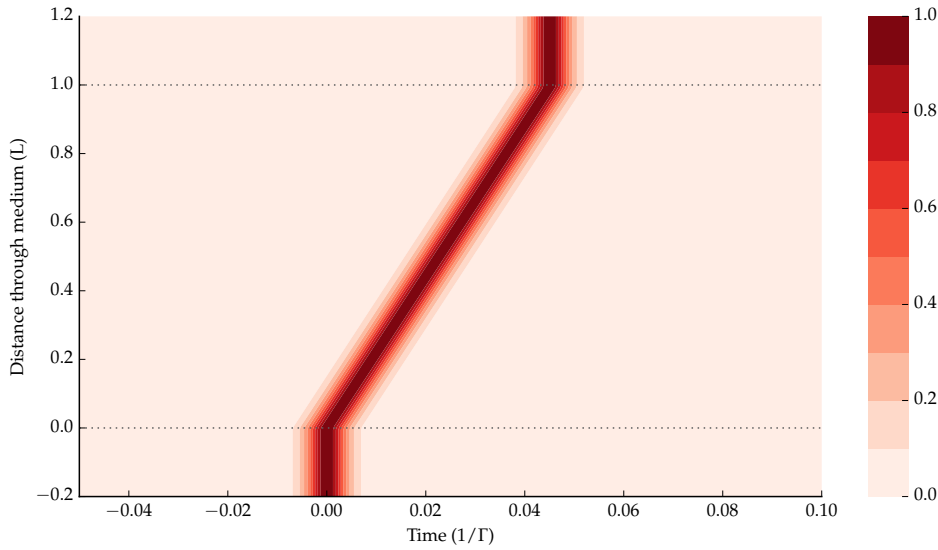


FIGURE 3.4 Simluated excited state population  $\rho_{11}$  for the propagation of a  $\theta = 2\pi$  sech pulse of FWHM  $\tau_w = 0.01 \tau_\Gamma$  through a medium with constant density such that  $Ng = 2\pi 10^3 \Gamma/L$ .

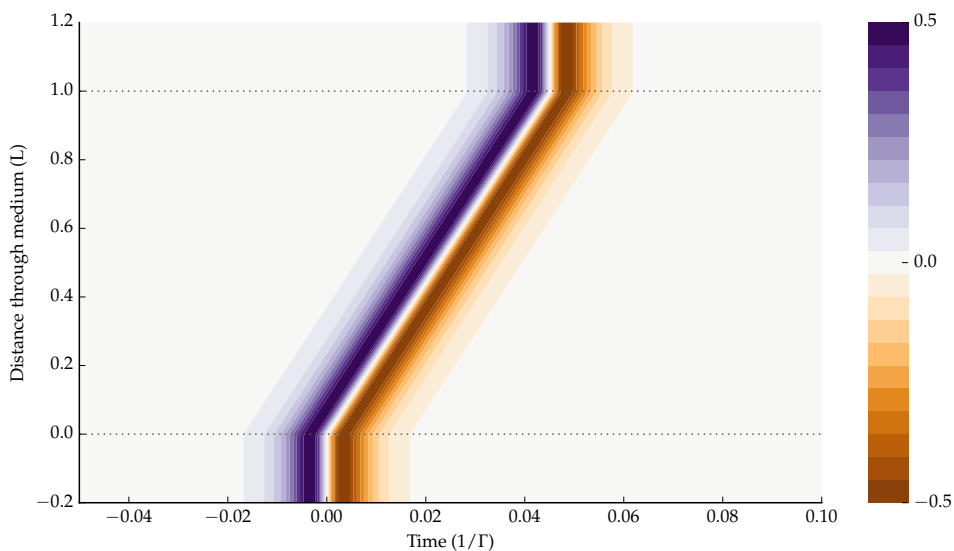


FIGURE 3.5 Simluated imaginary coherence  $\Im \rho_{01}$  for the propagation of a  $\theta = 2\pi$  sech pulse of FWHM  $\tau_w = 0.01 \tau_\Gamma$  through a medium with constant density such that  $Ng = 2\pi 10^3 \Gamma/L$ .

ation by looking at elements of the density matrix.

Figure 3.4 shows the excited state population  $\rho_{11}$ . We see that at each point in space through the medium, the pulse transfers all of the population to the excited state as the atoms absorb energy from the field, before returning it completely to the ground state.

In figure 3.5 we consider the imaginary part of the coherence  $\Im[\rho_{01}]$ . We see that at each point in space through the medium, this makes a complete oscillation.

Note that due to the form of the simulation, the results show atomic populations outside of the area of the medium area. We may consider the number density  $N$  to be arbitrarily close to zero in these regions.

As the sech pulse moves through the medium, its leading edge inverts each slice of the atomic population via absorption before its trailing edge returns the population to the ground state by stimulated emission.<sup>21</sup> The fact that we are in the regime where we may neglect spontaneous decay means that this rotation happens entirely within the phase memory of the atoms, and no energy is taken from the pulse. This phenomenon is known as *self-induced transparency* (SIT) as it is the area of the pulse itself which makes the medium transparent to it, and is an example of an optical soliton.<sup>22</sup>

We can understand that the group velocity  $v_g$  must necessarily be less than  $c$  due to the fact that the pulse energy spends some non-zero amount of its time as an excitation in the non-moving medium.

We are next led to consider the effect of applying a pulse of an area that is not exactly  $2\pi$  or of a different shape to the sech profile. In figure 3.6 we show the result of integration of the area theorem differential equations over a range of input pulse areas, representing the initial condition, from 0 to  $6\pi$  for an absorption coefficient  $\alpha = 2\pi 2\Gamma/L$ . We ob-

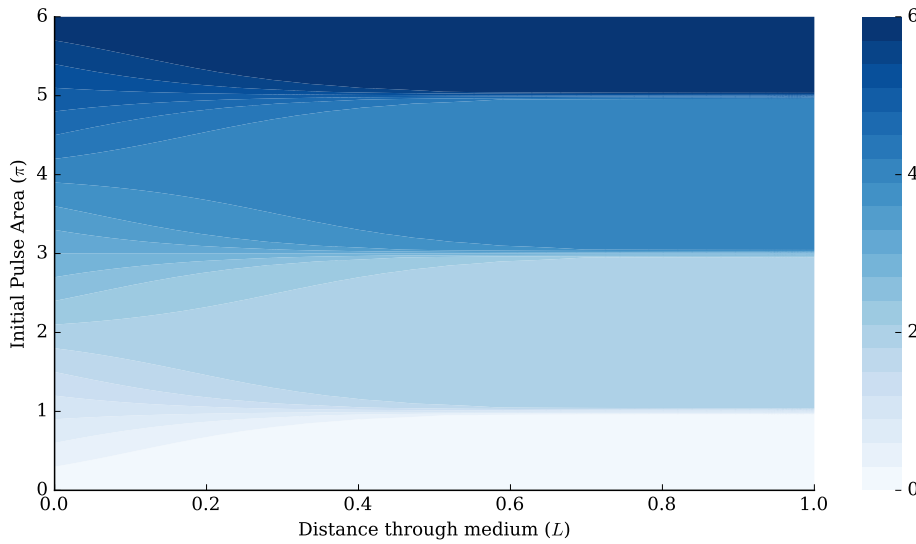


FIGURE 3.6 The pulse area  $\theta(z)$  solution to the area theorem differential equation (3.5) as a function of distance  $z$  and initial pulse area  $\theta_0(z)$  from 0 to  $6\pi$  for an absorption coefficient  $\alpha = 2\pi 2\Gamma/L$ .

serve that these inputs converge on stable solutions at the nearest even multiple of  $\pi$  (i.e.  $\theta(z) \rightarrow 0, 2\pi, 4\pi, \dots$ ).

In figure we demonstrate the effect of SIT for the propagation of resonant input pulses of  $0.8\pi$  and  $1.8\pi$  respectively. Both input pulses are Gaussians of width  $\tau_w = 0.01 \tau_\Gamma$  and the medium is such that  $N g_{01} = 2\pi 10^3 \Gamma/L$ .

We see that for the  $0.8\pi$  pulse in figure 3.7 (a) the area  $\theta(z)$  rapidly attenuates soon after entering the medium. The pulse energy is not entirely absorbed, however. The pulse bandwidth is much wider than the absorption window but still prone to dispersion and so the envelope is distorted and we see high-frequency ringing through the medium.

In clear contrast, for the  $1.8\pi$  pulse in figure 3.7 (b) the area  $\theta(z)$  tends to  $2\pi$  and the profile steepens and narrows into the sech-type soliton which propagates without absorption. We thus observe that the input pulse *does not need* to be of the sech profile to be capable of propagating

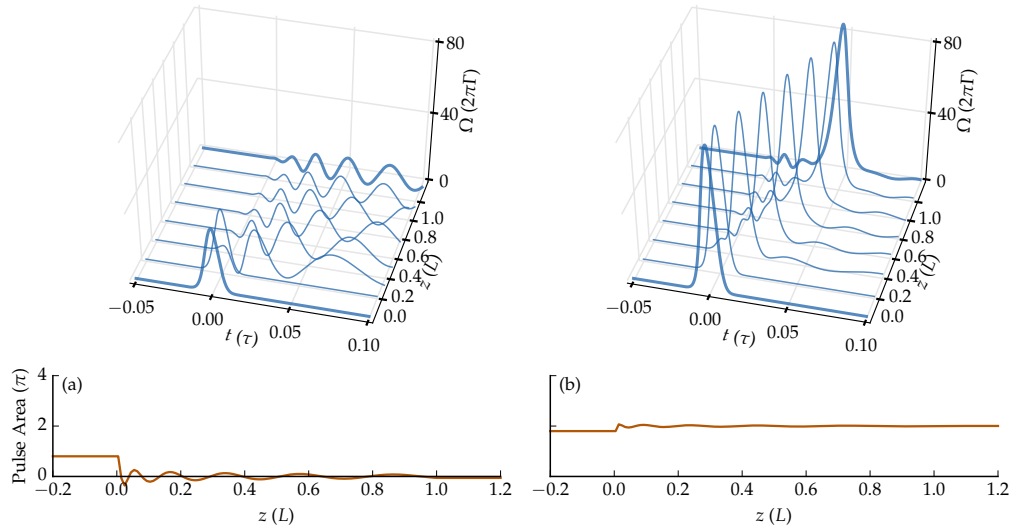


FIGURE 3.7 Propagation of (a)  $0.8\pi$  and (b)  $1.8\pi$  pulses, showing (top) profiles of the real part of the complex Rabi frequency  $\Omega(z, \tau)$  and (bottom) pulse area  $\theta(z)$ .

as an optical soliton as the medium can shape the pulse into that profile as it propagates if the pulse area  $\theta(z) > \pi$ .

We note again that the group velocity  $v_g$  is lower than  $c$  due to the energy of the field spending some amount of its time as an excitation in the fixed medium.

### 3.2.3 Pulse Breakup

For pulses  $> 3\pi$ , the area theorem predicts that the area will tend to the nearest even multiple of  $\pi$ , but in fact there are no steady-state solutions to the propagation problem other than the  $2\pi$  sech pulse.<sup>23</sup> In larger pulses, we find that the Rabi frequency envelope breaks into discrete  $2\pi$  envelopes with different widths and thus group velocities.<sup>21</sup>

In figures 3.8 and 3.9 we see the result of  $4\pi$  and  $6\pi$  sech-type pulses of width  $\tau_w = 0.02 \tau_\Gamma$  through a medium with  $Ng = 2\pi 10^3 \Gamma/L$ . Again we

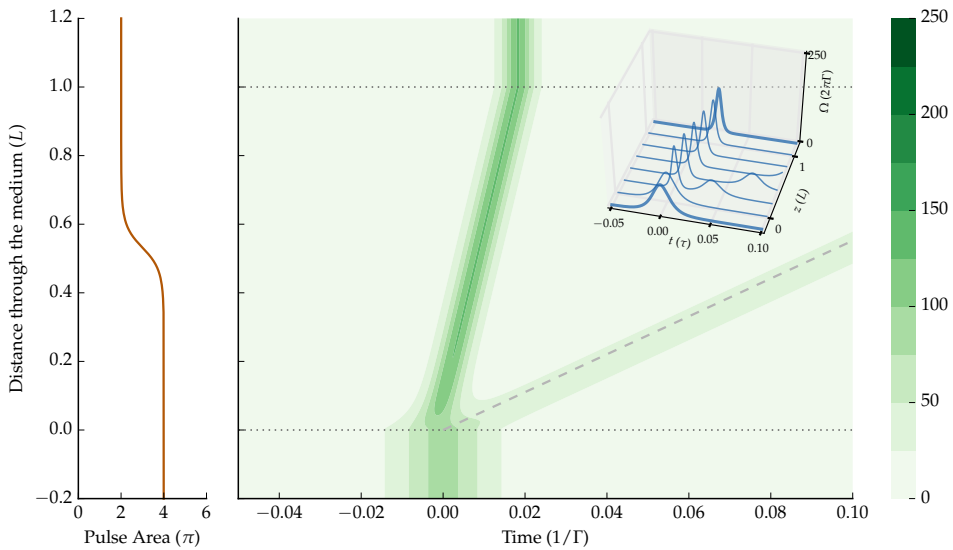


FIGURE 3.8 Propagation of a  $4\pi$  sech-type pulse. (main colourmap) Absolute value of the complex Rabi frequency  $\Omega(z, \tau)$ . The dashed line indicates the analytic pulse velocity given in equation (3.7). (inset 3D) Propagation profile of the pulse. (left) pulse area  $\theta(z)$ .

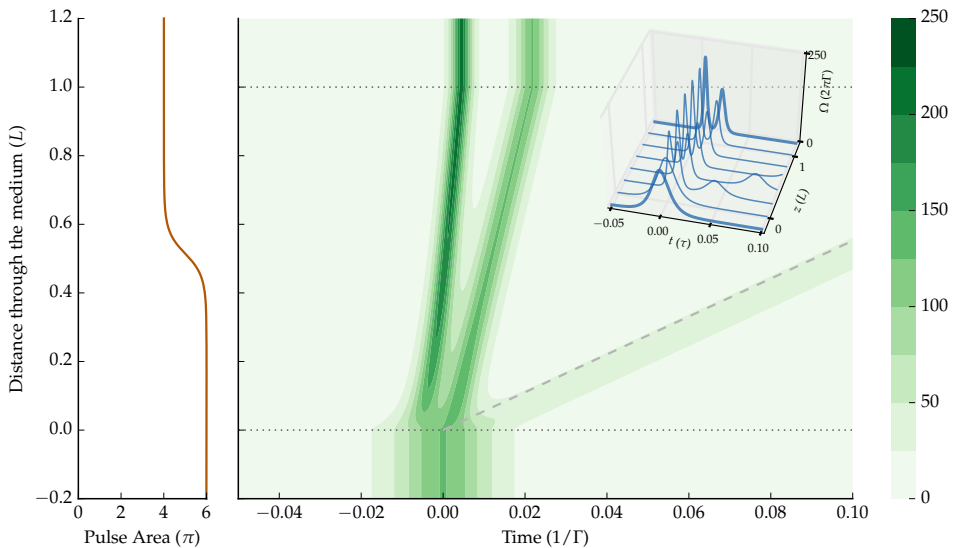


FIGURE 3.9 Propagation of a  $6\pi$  sech-type pulse. (main colourmap) Absolute value of the complex Rabi frequency  $\Omega(z, \tau)$ . (inset 3D) Propagation profile of the pulse. (left) pulse area  $\theta(z)$ .

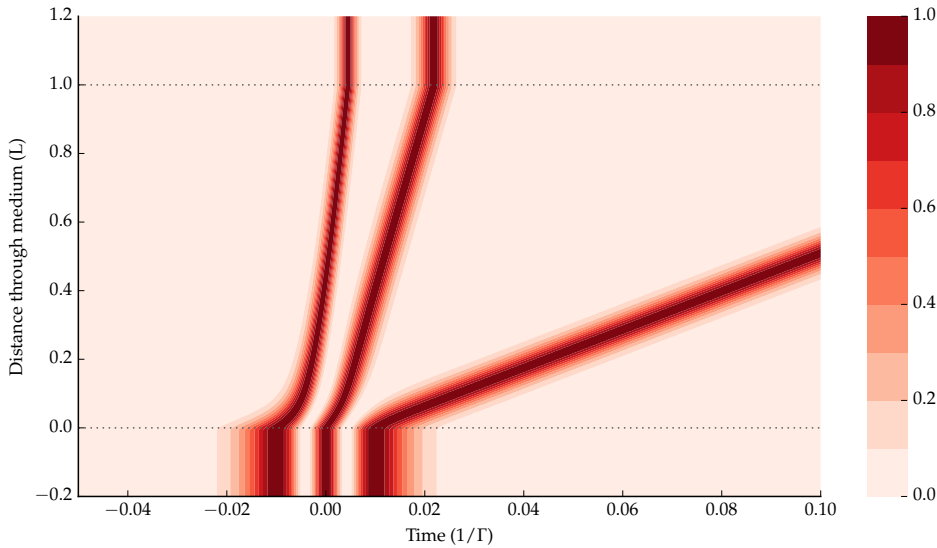


FIGURE 3.10 Simulated excited state population  $\rho_{11}$  for the propagation of a  $\theta = 6\pi$  sech pulse of FWHM  $\tau_w = 0.02 \tau_\Gamma$  through a medium with constant density such that  $Ng = 2\pi 10^3 \Gamma/L$ .

neglect the spontaneous decay of the excited state. We see that the pulse immediately breaks up on entering the medium and that the resultant pulses steepen into sech-type solitons just like the single  $2\pi$  pulse.

The resultant pulses have different widths and thus different group velocities as predicted in equation (3.6), though we see that the final resultant pulse travels at the same velocity as an incident  $2\pi$  pulse of the same original width. The area subplots confirm that the pulse area of each resultant pulse is the steady-state solution,  $2\pi$ .

Figure 3.10 shows the excited state population  $\rho_{11}$  corresponding to the  $6\pi$  sech pulse. We see that the resultant pulses emerge from each of the three full Rabi oscillations made by the  $6\pi$  pulse.

The first paper by McCall and Hahn describing SIT theoretically included experimental evidence of the effect.<sup>20</sup> Results were presented from an experiment using a liquid-helium ruby absorber showing that intense light transmitted without attenuation but delayed. In such early

experiments however it was difficult to discount the possibility of a hole-burning effect, where the absorber is saturated by the pulse. Gibbs and Slusher presented conclusive results from experiments using rubidium vapours,<sup>24</sup> including both large pulse delays and pulse breakup in good agreement with the theoretical prediction.

### 3.3 *Propagation of Light in Three-level Atoms*

The solutions to the Maxwell-Bloch equations we have considered thus far have all involved the two-level atom model. In reality atoms consist of an infinite number of discrete levels along with a continuum of levels corresponding to the free electron. Two-level atom do not exist, but the model can successfully describe the interaction of a monochromatic field with a frequency near resonant with a pair of discrete energy levels. For multi-chromatic fields, other energy levels may need to be introduced due to transitions involving them becoming near-resonant with components of the field.

The simplest extension of the two-level model is obviously to add a second frequency complement near-resonant with a third atomic level. This extension may seem incremental but in fact produces a variety of interesting and useful phenomena, due to the presence of quantum superposition dark states. Such phenomena include stimulated Raman adiabatic passage (STIRAP),<sup>25,26</sup> lasing without inversion<sup>27–29</sup> and phaseonium,<sup>30,31</sup> which have been well-studied in theory and experiment. We will discuss further two other well-studied phenomena in this thesis: matched pulses and simultons in this chapter, and electromagnetically induced transparency (EIT) in chapter 4.

First we take the opportunity to note that there are three available configurations of three-level atoms according to the transitions chosen for

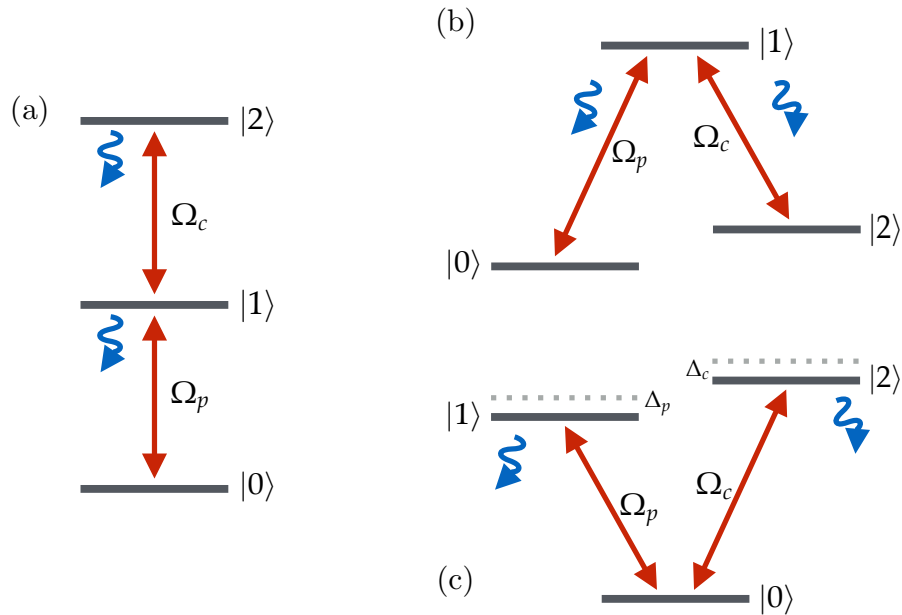


FIGURE 3.11 The three possible configurations of three-level atoms: (a) the  $\Sigma$  (or ladder) configuration, (b) the  $\Lambda$  configuration and (c) the V configuration.

coupling. These are illustrated in figure 3.11.

In the  $\Sigma$  (or ladder) configuration, the ground-state  $|0\rangle$  is coupled to the excited state  $|1\rangle$  as in the two-level atom, and a second field couples the transition from this intermediate excited state to a higher state, which we label  $|2\rangle$ . The transition  $|0\rangle$  to  $|2\rangle$  is considered to be dipole forbidden by virtue of these states having the same parity. This configuration has proved useful for excitation to highly excited Rydberg states which allow for strong dipole-dipole interaction between atoms.<sup>32</sup>

In the  $\Lambda$  configuration, the atom has two lower states  $|0\rangle$  and  $|2\rangle$ , and a single excited state  $|1\rangle$  which is coupled to both lower states. These could for example represent a ground state hyperfine doublet. The two lower states are taken to be dipole forbidden. We will investigate the  $\Lambda$  configuration in greater detail when we investigate EIT and the propagation of dark state polaritons in chapter 4.

Finally, in the V configuration, the atom has two excited states  $|1\rangle$  and  $|2\rangle$ , and a single ground state level  $|0\rangle$  which is coupled to both excited states. We do not allow transitions between the two excited states. It is the V configuration we will consider further in this chapter, as we extend the theory of SIT in two-level atoms to a pair of fields interacting with a thermal medium on resonance with transitions such that we describe the medium as consisting of V-type atoms.

### 3.4 Matched Pulses & Simultons in Three-Level Atoms

The study of optical solitons propagating due to self-induced transparency, summarised in section 3.2, can be extended to consider short resonant pulses in three-level media. It has been determined theoretically that simultaneous optical solitons — or *simultons* — propagating at the different transition wavelengths exist as analytic solutions to the three-level MB equations.

#### 3.4.1 Literature Review

As the results of this work on short resonant pulses in three-level atoms, beginning in the 1980s, are less familiar than that of soliton propagation in the two-level system, we take the opportunity here to review some of the key developments.

The first studies on propagation of simultaneous, different-wavelength optical pulses were made by Konopnicki & Eberly, 1981.<sup>33,34</sup> The authors derived analytic solutions to the MB equations representing optical solitons propagating simultaneously at different wavelengths, which they named *simultons*. They found analytic descriptions for exactly matched sech pulses with identical oscillator strengths (*i.e.*  $g_{01} = g_{02}$

in the MB model) in  $Xi$ -type and  $V$ -type three-level media.

Further analytic work by Kujawski, 1982<sup>35</sup> showed that the MB equations for the three-level system on two-photon resonance can be reduced to the sine-Gordon equation,<sup>36</sup> thus confirming that the simulton is an optical soliton solution. The author also showed that the conditions required for multi-simulton propagating are the same as Konopnicki & Eberly showed for single multitons.

Eberly, 1999 looked at transmission of dressed fields in  $\Lambda$ -type three-level media.<sup>37</sup> The  $\Lambda$  system has a dark state which is able to trap population (we will consider this further in chapter 4). The analytic solution in this case showed that the probe envelope  $\Omega_p$  is of the familiar sech shape while the coupling envelope must be of a tanh profile, in a counter-intuitive pulse sequence similar to that employed in STIRAP.

Rahman & Eberly, 1998, provided<sup>38</sup> an ansatz for analytic solution of the three-level MB equations for Doppler-broadened pulse pairs, including analytic solutions for pulse amplitude, excited state population, group and phase velocities. In an associated numerical study, the same authors looked at<sup>39</sup> propagation of pulses in V-type media with inhomogeneous broadening. The authors relaxed the conditions imposed by the analytic model to include non-matched pulses and non-sech envelopes, finding that it is possible for non-matched pulses to match themselves in certain conditions and that, as in the two-level case, the sech shape is a natural steady state for V-type pulses rather than a mathematically singular solution, and so other pulse envelopes will propagate. Finally, they demonstrated the numerical validity of a two-photon pulse area theorem, including the case of pulse breakup.

### 3.4.2 The Two-Photon Area Theorem

We will consider the V-type system similar to that described in the latter papers by Rahman and Eberly,<sup>39</sup> and present some numerical results from our MB model for this system. We start with a quantised V-type three-level atom as illustrated in figure 3.11.

The total electric field vector for the two laser beams is described by

$$\mathbf{E}(z, t) = \left[ \frac{1}{2} \hat{\mathbf{x}}_p \mathcal{E}_p(z, t) e^{i(k_p z - \omega_p t)} + \frac{1}{2} \hat{\mathbf{x}}_c \mathcal{E}_c(z, t) e^{i(k_c z - \omega_c t)} + \text{c.c.} \right] \quad (3.8)$$

where  $\hat{\mathbf{x}}_p$  and  $\hat{\mathbf{x}}_c$  are orthogonal polarisations of the fields and the envelopes  $\mathcal{E}_p$  and  $\mathcal{E}_c$  are in general complex functions. We define corresponding Rabi frequencies  $\Omega_p = d_{01} \mathcal{E}_p / \hbar$  and  $\Omega_c = d_{02} \mathcal{E}_c / \hbar$  where  $d_{0j}$  is the dipole moment between level  $|0\rangle$  and  $|j\rangle$ , which we take parallel to its respective field polarisation.

The Hamiltonian for the V-type three-level atom interacting with these two classical fields is

$$\mathcal{H}_V = -\hbar(\Delta_p \sigma_{11} + \Delta_c \sigma_{22}) - \frac{\hbar}{2} [(\Omega_p \sigma_{10} + \Omega_c \sigma_{20}) + \text{h.c.}] \quad (3.9)$$

within the dipole approximation and in the frame rotating with the frequencies of the optical fields. Here  $\sigma_{ij} := |i\rangle \langle j|$  is the transition operator. The detunings of the fields are represented by  $\Delta_p$  and  $\Delta_c$ .

We may imagine a pair of synchronised input fields, such that

$$\Omega_c(0, \tau) = r \Omega_p(0, \tau) \quad (3.10)$$

for some constant  $r$ . The labels  $p$  and  $c$  denote the typical probe-coupling setup in three-level atom experiments. It can be shown<sup>38</sup> by substitution into the MB equations that the system is equivalent to the two-level system addressed by a single pulsed field.

The concept of the area theorem then extends to the pair of field envelopes with

$$\theta(z) = \sqrt{\theta_c(z)^2 + \theta_p(z)^2} \quad (3.11)$$

where  $\theta_c(z)$  and  $\theta_p(z)$  are the areas of the coupling and probe pulses defined in the same way as equation (3.4). A pair of pulses that can be expressed in the form of equation (3.10) are known as *matched pulses*.

Equation (3.11) does not constrain the individual pulse areas, and so predicts that matched pulses will propagate through the medium even if the area of either or both of the individual pulses would not be strong enough to support a soliton solution in a two level system.

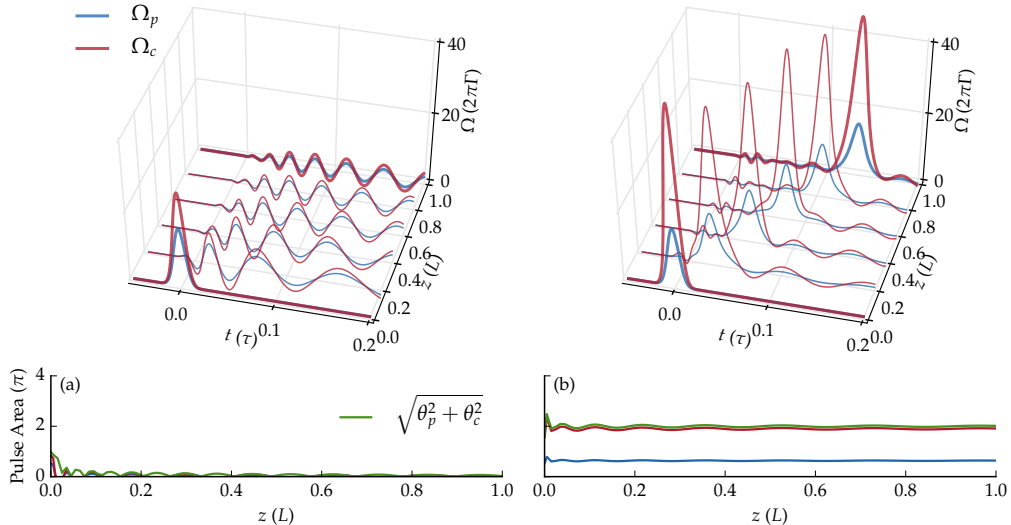


FIGURE 3.12 Propagation of matched pulses. (a) A probe input  $0.5\pi$  pulse with a  $0.8\pi$  coupling pulse. (b) A probe input  $0.5\pi$  pulse with a  $1.5\pi$  coupling pulse, showing (top) profiles of the real part of the complex Rabi frequencies  $\Omega(z, \tau)$  and (bottom) pulse areas  $\theta(z)$ .

In figure 3.12 we show example numerical results for propagation of matched pulses in a V-type medium. In both cases the input probe pulse has an area  $\theta_p = 0.5\pi$ . The medium is specified such that  $Ng = 2\pi 10^3 \Gamma/L$  on both transitions and spontaneous decay is neglected. In

figure 3.12(a) the input coupling pulse has area  $\theta_c = 0.8\pi$ , such that the total area given in equation (3.11) is  $\theta(z=0) = 0.9\pi$ . We see that neither of the fields propagates, both are absorbed and  $\theta(z) \rightarrow 0\pi$ . In figure 3.12(b), the input coupling pulse has area  $\theta_c = 1.5\pi$ , such that the total area  $\theta(z=0) = 1.6\pi$ . We see that both fields propagate as sech-type solitons such that  $\theta(z) \rightarrow 2\pi$ .

This striking result suggests that it is possible for weaker pulses to propagate through media they would ordinarily find opaque, by virtue of them being ‘carried along’ with an exactly matched coupling pulses.

### 3.5 Discussion

In this chapter we have taken the model introduced in chapter 2 for propagation of light in thermal two-level atomic vapours beyond the weak probe regime to consider nonlinear phenomena, specifically the propagation of optical solitons via self-induced transparency. We then extended the quantised atom model to consider three-level atom configurations, which present a range of interesting properties due to the presence of quantum superposition dark states. Finally we considered the theoretical concept of simultaneous optical solitons, *simultons* in V-type three-level configurations.

This completes the part of the thesis dedicated to presenting theoretical background, and in the following chapters we will present original research findings based on the concepts we've introduced. We start in chapter 4 with an investigation into the propagation of dark-state polaritons in  $\Lambda$ -type atoms.

## *4 Storage and Retrieval of Dark-State Polaritons*

*4.1 Introduction*

*4.2 Electromagnetically Induced Transparency  
in  $\Lambda$ -Type Atoms*

*4.3 Pulse Propagation in EIT Media*

*4.4 Storage & Retrieval of Dark-State Polaritons*

*4.5 Discussion*

# *5   Two-Photon Excitation in a High-Intensity Beam*

## *5.1   Introduction*

In keeping with the theme of atom-light interactions beyond linear regimes, in this chapter we present a theoretical study of the interaction of a high- intensity beam with a thermal vapour of rubidium. Specifically, we investigate fluorescence from high-level states, observed in scans across the D<sub>2</sub> spectral lines. Recent experimental work<sup>40</sup> found dramatic enhancement of this fluorescence above a critical density, indicating an increase in population transfer from the ground state to the higher 5d states.

The high intensity of the beam makes invalid any recourse to the weak probe approximation and necessitates the consideration of the significant mechanisms of power broadening and hyperfine optical pumping. We must also in our model take into account Doppler broadening due to the motion of thermal atoms in the cell.

The combination of hyperfine pumping and the finite transit time of non-stationary atoms in the beam also prevents us from simply taking the steady-state atomic response: we must solve for quantum evolution of the atomic system via the density matrix. The computational model

here developed to study the system dynamics uses an exponential series solver for the Lindblad master equation (2.29) over the many-level basis of hyperfine angular momentum sublevels, along with parallel computation across the range of detunings.

## 5.2 Description of the Experiment

A high-intensity cw laser beam, near-resonant with the D2 lines, was incident on a thermal vapour cell of rubidium atoms in their natural isotopic abundances. The D2 lines represent resonant transitions from the  $5^2S_{1/2}$  ground state of the atom to the  $5^2P_{3/2}$  excited state manifold. The Pyrex cell had a length of 2 mm in the propagation direction  $z$  and sat in a thermal oven. The beam had a waist (*i.e.*  $1/e^2$  radius) of  $6.6 \pm 0.2 \mu\text{m}$  and a power of 80 mW, providing a peak beam intensity of  $1.2 \times 10^5 \text{ W cm}^{-2}$ .<sup>40</sup>

A lens was used to image fluorescence onto a multi-mode fibre connected to a spectrometer. This revealed fluorescence from excited states that cannot be accessed energetically from individual photon excitations near-resonant with the D2 transitions. In order to investigate this fluorescence further, side-imaging was used in conjunction with a blue bandpass filter to remove other optical wavelengths and to select only the blue fluorescence from the vapour cell. The selected blue fluorescence was then focussed using a lens onto a calibrated photo-diode that had a large gain over the visible spectrum.

By spectral analysis it was determined that the source of the fluorescence was decay from the  $6^2P_{1/2}$  and  $6^2P_{3/2}$  excited state doublet.

The high-intensity excitation laser was then scanned over the D2 lines, with hyperfine saturated absorption spectroscopy used to calibrate the

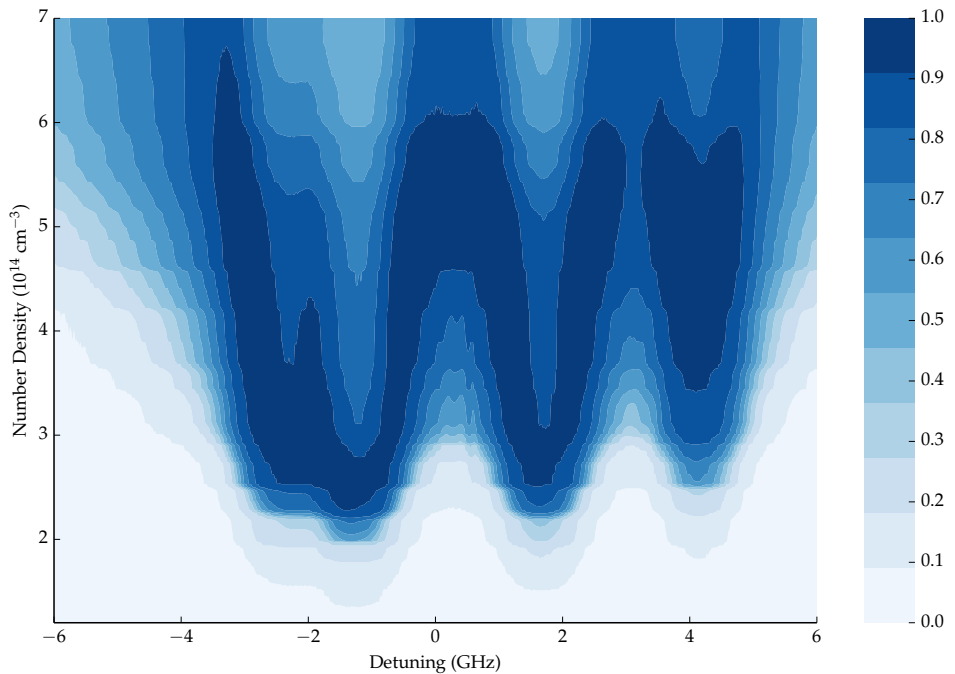


FIGURE 5.1 Normalised experimental fluorescence from the  $6^2P_{1/2}$  and  $6^2P_{3/2}$  transitions, recorded for light input across a GHz detuning range covering the D2 lines, and over a range of number densities  $N$  (and thus temperatures  $T$ ).

detuning. A non-overlapping weak cw probe was simultaneously incident on the vapour cell in order to measure the atomic number density as a function of the cell temperature.

In figure 5.1 we see the spectral dependence of the measured fluorescence as the laser is scanned over a 12 GHz frequency range covering the D2 lines, with the zero centred on the centre-of-mass transition of the fine structure manifolds. The fluorescence is shown normalised as a function of detuning (on the horizontal axis) and number density (on the vertical).

Even from the lowest number densities measured we observe fluorescence, but the striking feature of these results is the the sudden and dramatic increase in fluorescence at around  $2 \times 10^{14} \text{ cm}^{-3}$  across the fluorescence peaks. Our aim in the theoretical work of this chapter is

determine whether the dependence of the fluorescence on the number density can be understood with a description based on the response of individual atoms, or if we must consider collective effects like energy pooling,<sup>41–43</sup> where inelastic collisions between excited atoms results in transfer to states with higher energies, or cooperative effects arriving from dipole-dipole interactions.<sup>44,45</sup>

### 5.3 Theoretical Model

We wish to investigate population of the 6P doublet states which lie close to two-photon resonance as the high-intensity laser is scanned across the D<sub>2</sub> lines. We will need to consider light coupling the 5<sup>2</sup>S<sub>1/2</sub> ground state to the 5<sup>2</sup>P<sub>1/2</sub> and 5<sup>2</sup>S<sub>3/2</sub> states, and then coupling those intermediate states up to the 5<sup>2</sup>D<sub>3/2</sub> and 5<sup>2</sup>D<sub>5/2</sub> via two-photon excitation. The model will then incorporate the 6<sup>2</sup>P<sub>1/2</sub> and 6<sup>2</sup>P<sub>3/2</sub> levels after decay from the 5D states. Decay from the 6P doublet back down to the 5<sup>2</sup>S<sub>1/2</sub> ground state is the channel responsible for the blue fluorescence.

The fine structure manifolds included in the model and their hyperfine levels are illustrated in figure 5.2. Experimentally measured values for the transition frequencies to these manifolds from the ground state are listed in table 5.1.

In order to investigate the cause of the fluorescence at the scanning resolution of the experiment, as well as to include the effect of pumping mechanisms, our state basis must include the hyperfine structure and magnetic substructure of these fine structure manifolds, consisting of  $2F + 1$  degenerate sublevels  $m_F = -F, -F + 1, \dots, F - 1, F$  within each hyperfine level.

The classical description of the high-intensity field is as we saw for a

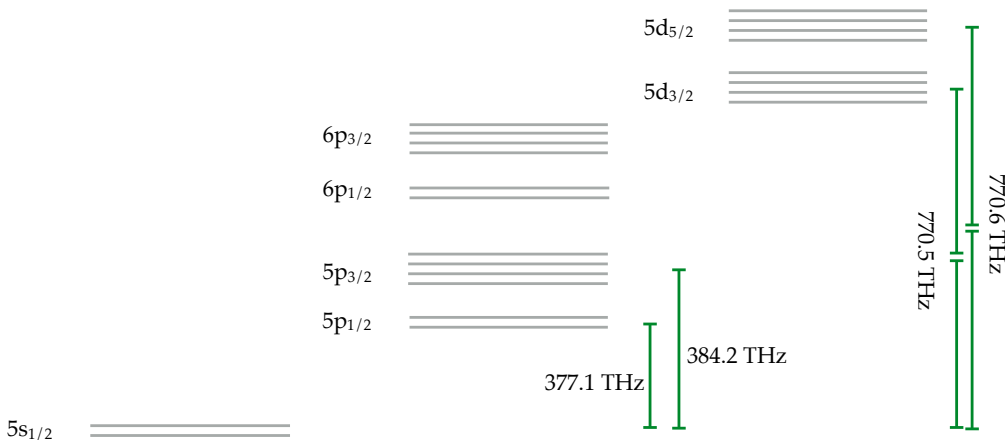


FIGURE 5.2 Hyperfine structure of selected manifolds of rubidium 87. Frequencies of the  $5^2S_{1/2} \rightarrow 5^2P_{1/2}$  (D1) and  $5^2S_{1/2} \rightarrow 5^2P_{3/2}$  (D2) transitions are shown, along with the  $5^2S_{3/2} \rightarrow 5^2D_{3/2}$  and  $5^2S_{3/2} \rightarrow 5^2D_{5/2}$  transitions, close to two-photon resonance on D2.

Manifold ( $J'$ )	Energy	$A_{hf}$ for $^{87}\text{Rb}$	$A_{hf}$ for $^{85}\text{Rb}$
$5^2S_{1/2}$	0.0	3,417.34	1,011.91
$5^2P_{1/2}$	377.1074	406.20	120.53
$5^2P_{3/2}$	384.2304	84.85	25.00
$6^2P_{1/2}$	710.9602	132.56	39.12
$6^2P_{3/2}$	713.2839	27.70	8.16
$5^2D_{3/2}$	770.4827	14.43	4.18
$5^2D_{5/2}$	770.5715	7.44	-2.19

TABLE 5.1 Experimental values of transition frequencies (in  $2\pi$  THz) for selected energy levels of rubidium, along with hyperfine constants  $A_{hf}$  (in  $2\pi$  MHz) for the 85 and 87 isotopes. See equation (5.3) for the definition of  $A_{hf}$ . Values are from NIST data, recorded in Sansonetti, 2006.<sup>46</sup>  $A_{hf}$  values are from Arimondo, 1977 and Banerjee, 2007.<sup>47,48</sup>

two-level atomic model in chapter 2, consisting of a monochromatic electric field

$$\mathbf{E}(z, t) = \frac{1}{2} \hat{\mathbf{x}} \left[ \mathcal{E}(z, t) e^{i(kz - \omega t)} + \mathcal{E}^*(z, t) e^{-i(kz - \omega t)} \right] \quad (5.1)$$

where once again  $\hat{\mathbf{x}}$  is the polarisation vector of the fields and the envelope  $\mathcal{E}(z, t)$  is a complex function.

As in the case of the two- and three-level systems described in chapters 2 and 3, in order to solve for the time evolution of the atomic system during interaction with the field of equation (5.1), we must define the dipole operator by determining the transition dipole matrix elements coupling states of the atomic basis. First we will define the atomic basis and the bare Hamiltonian with the inclusion of atomic angular momentum structure.

### 5.3.1 Angular Momentum Structure

The bare atomic Hamiltonian for the hydrogenic description of a rubidium atom represents the state of the valence electron prior to interaction with the optical field.

The bare atomic Hamiltonian for the hydrogenic description of a rubidium atom represents the state of the valence electron prior to interaction with the optical field.

Our basis consists of the set of all hyperfine sublevels contained in the fine structure manifolds in the model, indexed by quantum numbers  $n$  and  $J$ . The bare atomic Hamiltonian in the hyperfine basis is then given by the sum of projection operators for those hyperfine sublevels, result-

ing in a diagonal operator

$$\mathcal{H}_0 = \hbar \sum_{Fm_F} \delta\omega_F |Fm_F\rangle \langle Fm_F| + \hbar \sum_{n'J'} \sum_{F'm'_F} (\omega_{nJ} + \delta\omega_{n'J',F'}) |F'm'_F\rangle \langle F'm'_F| \quad (5.2)$$

where  $F$  and  $m_F$  index the ground state hyperfine sublevels and  $\delta\omega_F$  values represent the energy shifts of the hyperfine levels relative to the centre of gravity of the ground state manifold. Similarly,  $F'$  and  $m'_F$  index the excited state hyperfine sublevels and  $\delta\omega_{n'J',F'}$  represent the energy shifts relative to the the centre of gravity of those excited state manifolds given by  $\omega_{n'J'}$ , the transition frequency from the ground state manifold to each state, listed in table 5.1.

The energy shifts  $\delta\omega_{n'J',F'}$  express coupling between the total electronic angular momentum  $\mathbf{J}$  and the nuclear angular momentum  $\mathbf{I}$ , and to first order can be expressed via

$$\delta\omega_{n'J',F'} = \frac{A_{\text{hf}}}{\hbar^2} (\mathbf{I} \cdot \mathbf{J}) \quad (5.3)$$

where the values  $A_{\text{hf}}$  are (magnetic dipole) hyperfine constants, also listed in table 5.1. We shall neglect higher-order corrections, including electric quadrupole coupling, in this model as the energy shifts are relatively small.

Figure 5.3 illustrates the hyperfine structure coupled by the field and gives hyperfine energy level splittings for the  $5^2S_{1/2}$ ,  $5^2P_{1/2}$ ,  $5^2P_{3/2}$  and  $5^2D_{3/2}$  levels coupled by the fields for both naturally occurring isotopes:  $^{85}\text{Rb}$  and  $^{87}\text{Rb}$ . We assume in this model that no static electric or magnetic fields are present to break the degeneracy of the magnetic sublevels.

Coupling this atom to a field of frequency  $\omega$ , we as usual choose to transform to the frame rotating with the field. For conciseness we will index the fine structure manifolds directly coupled by the field so that

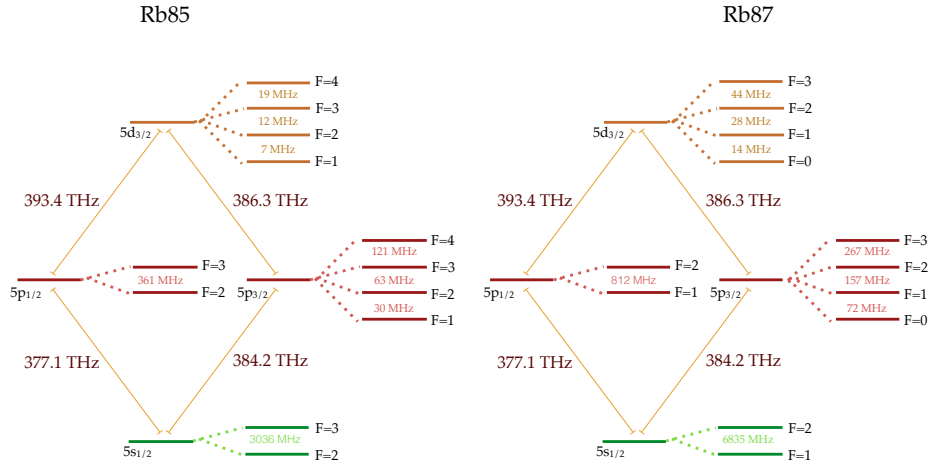


FIGURE 5.3 Hyperfine splittings of the  $5^2S_{1/2}$ ,  $5^2P_{1/2}$ ,  $5^2P_{3/2}$  and  $5^2D_{3/2}$  levels in rubidium, for both isotopes, 85 and 87, showing the two-photon coupling and transition frequencies. Each hyperfine level consists of  $2F + 1$  degenerate sublevels. These splittings are determined from the experimental values given and referenced in table 5.1.

$|F_0 m_{F_0}\rangle$  labels states the  $5^2S_{1/2}$  ground state,  $|F_1 m_{F_1}\rangle$  labels the  $5^2P_{3/2}$  intermediate states,  $|F_2 m_{F_2}\rangle$  labels the  $5^2D_{3/2}$  excited states and  $|F_3 m_{F_3}\rangle$  represents states in the other member of the excited doublet,  $5^2D_{5/2}$ .

We then write the bare Hamiltonian in the rotating frame as

$$\begin{aligned} \mathcal{H}'_0 = & \hbar \sum_{F_0 m_{F_0}} \delta\omega_{F_0} |F_0 m_{F_0}\rangle \langle F_0 m_{F_0}| + \hbar \sum_{F_1 m_{F_1}} (\delta\omega_{F_1} - \Delta_{01}) |F_1 m_{F_1}\rangle \langle F_1 m_{F_1}| + \\ & \hbar \sum_{F_2 m_{F_2}} (\delta\omega_{F_2} - (\Delta_{01} + \Delta_{12})) |F_2 m_{F_2}\rangle \langle F_2 m_{F_2}| + \\ & \hbar \sum_{F_3 m_{F_3}} (\delta\omega_{F_3} - (\Delta_{01} + \Delta_{13})) |F_3 m_{F_3}\rangle \langle F_3 m_{F_3}| \end{aligned} \quad (5.4)$$

where we define  $\Delta_{01} = \omega - \omega_{01}$  as the detuning from resonance of the lower transition;  $\Delta_{12} = \omega - \omega_{12}$  and  $\Delta_{13} = \omega - \omega_{13}$  as the detunings from resonance of the upper transitions.

The manifolds involved in direct coupling are illustrated in figure 5.4. In the rotating frame description, eigenstates in the other manifolds are

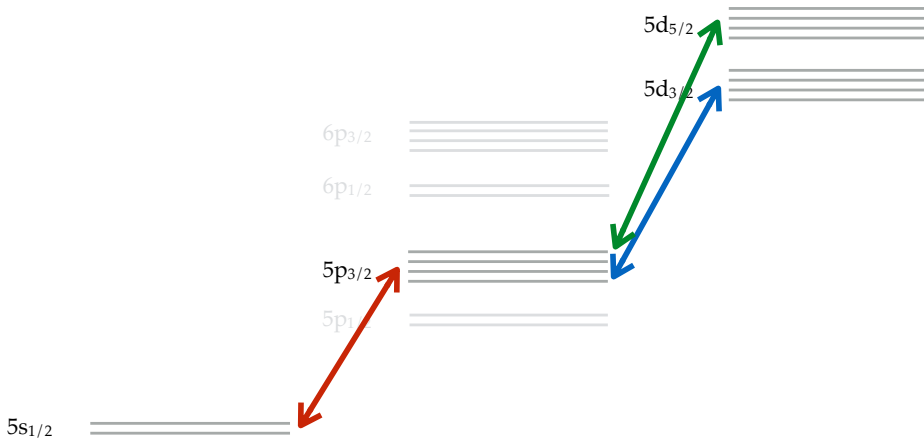


FIGURE 5.4 Couplings of hyperfine manifolds included in the model. The laser is scanned across the  $5^2S_{1/2} \rightarrow 5^2P_{3/2}$  (D2) transition (red). The D1 transition is too far from resonance and so is not coupled in the model. The same D2 laser frequency couples  $5^2P_{3/2} \rightarrow 5^2D_{3/2}$  and  $5^2P_{3/2} \rightarrow 5^2D_{5/2}$  upper transitions.

given zero energies, as they are not involved in the atom-light interaction part of the Hamiltonian. Note in particular that this includes the  $5^2P_{1/2}$  intermediate manifold. When we are near resonance with the D2 transition, we assume that the D1 resonance coupling frequency is far enough from resonance to be neglected.

We see that this model is similar to a three-level system in the  $\Xi$  (ladder) configuration, but with a fourth level introducing an additional excited state manifold, forming a Y configuration. And of course in this case we have the added complexity of hyperfine structure included.

The ladder is constrained in that it is the same field coupling the lower and upper transitions, so that the detunings only differ by constants.

These are simply expressed as  $\Delta_{12} = \Delta_{01} + \eta_2$  and  $\Delta_{13} = \Delta_{01} + \eta_3$ , where  $\eta_2 := (\omega_2 - \omega_1) - (\omega_1 - \omega_0) = \omega_2 - 2\omega_1$  and  $\eta_3 := (\omega_3 - \omega_1) - (\omega_1 - \omega_0) = \omega_3 - 2\omega_1$ .

### 5.3.2 Reducing the Transition Dipole Matrix Elements

Now that we have defined a Hilbert space basis and expressed the bare atomic Hamiltonian, the next step is to formulate the dipole operator. In order to do this we must compute the transition dipole matrix elements  $\langle Fm|d|F'm'_F\rangle$  coupling individual basis states.

Calculating these matrix elements by integrating over the eigenstate wavefunctions explicitly is a computationally-intensive task. Fortunately, the spherical symmetry of the single-electron atom model allows us to use the spherical basis to factor out the angular part of the problem into coefficients that can be calculated much more quickly.

The spherical vector basis for 3D space is often more convenient than the Cartesian basis when dealing with angular momentum and spherical harmonics. The position vector  $\mathbf{r}$  is given in this basis as

$$\mathbf{r} = r_- \hat{\mathbf{e}}_- + r_0 \hat{\mathbf{e}}_0 + r_+ \hat{\mathbf{e}}_+ \quad (5.5)$$

where the basis unit vectors  $\hat{\mathbf{e}}_-$ ,  $\hat{\mathbf{e}}_0$  and  $\hat{\mathbf{e}}_+$  are constructed as a complex linear combination of the Cartesian unit vectors

$$\hat{\mathbf{e}}_- = \frac{\mathbf{e}_x - i\mathbf{e}_y}{\sqrt{2}}, \quad (5.6)$$

$$\hat{\mathbf{e}}_0 = \mathbf{e}_z, \quad (5.7)$$

$$\hat{\mathbf{e}}_+ = \frac{-\mathbf{e}_x - i\mathbf{e}_y}{\sqrt{2}}. \quad (5.8)$$

forming a complete orthonormal basis.

The vector coordinates we then get from substitution, as

$$r_- = \frac{x + iy}{\sqrt{2}} \quad (5.9)$$

$$r_0 = z \quad (5.10)$$

$$r_+ = \frac{-x + iy}{\sqrt{2}}. \quad (5.11)$$

We label the components  $r_-, r_0, r_+$  via the index  $q \in \{-1, 0, 1\}$ .

The Wigner-Eckart theorem,<sup>49,50</sup> with the dipole operator a tensor of rank one, allows us to factor out the angular part of the dipole matrix elements such that they can be written in terms of Wigner symbols. Our derivation of the reduced dipole matrix elements will follow that given in Steck, 2007.<sup>51</sup>

Firstly the matrix elements can be factored such that the dependence on the  $m_F$  and  $m'_F$  quantum numbers is entirely within a Wigner 3-j factor, via the expression

$$\begin{aligned} \langle Fm_F | d_q | F'm'_F \rangle &= \langle F | e\mathbf{r} | F' \rangle \\ &\times (-1)^{F'-1+m_F} \sqrt{2F+1} \begin{pmatrix} F' & 1 & F \\ m'_F & q & -m_F \end{pmatrix} \end{aligned} \quad (5.12)$$

where  $\langle Fm_F | d_q | F'm'_F \rangle$  is now the reduced hyperfine dipole matrix element.

We can go one step further in the reduction as the hyperfine transition couples states corresponding to different  $\mathbf{F} = \mathbf{J} + \mathbf{I}$ , but the dipole operator depends only on the position of the electron, not the nuclear state  $|Im_I\rangle$ . We may thus factor out again

$$\begin{aligned} \langle F | e\mathbf{r} | F' \rangle &= \langle J | e\mathbf{r} | J' \rangle \\ &\times (-1)^{F'+J+1+I} \sqrt{(2F'+1)(2J+1)} \left\{ \begin{array}{ccc} J & J' & 1 \\ F' & F & I \end{array} \right\} \end{aligned} \quad (5.13)$$

where now the dependence on  $F$  and  $F'$  is also factored out of the reduced fine structure matrix element  $\langle J | e\mathbf{r} | J' \rangle$  and the angular dependence of the dipole matrix element is given by the Wigner 6-j coefficient, which can be calculated easily.

The reduced fine structure matrix element must be calculated theoretically by integrating over the radial parts of the atomic wavefunction in a

$nL_J$	$n'L'_{J'}$	$\Gamma_{J,J'}$	$\langle J \parallel e\mathbf{r} \parallel J' \rangle$
$5S_{1/2}$	$5P_{1/2}$	5.750	3.007
$5S_{1/2}$	$5P_{3/2}$	6.067	4.245
$5P_{1/2}$	$5D_{3/2}$	0.4756	1.143
$5P_{3/2}$	$5D_{3/2}$	0.1068	0.3935
$5P_{3/2}$	$5D_{5/2}$	0.6266	1.167
$6P_{1/2}$	$5D_{3/2}$	0.209	12.87
$6P_{3/2}$	$5D_{3/2}$	0.03770	4.103
$6P_{3/2}$	$5D_{5/2}$	0.2273	12.31

TABLE 5.2 Spontaneous Decay Lifetimes (ns) and reduced transition dipole matrix elements ( $ea_0$ ) for fine structure transitions relevant to the model. Decay lifetimes are from Safronova, 2011 and Sansonetti, 2006<sup>46,52</sup> and transition dipole matrix elements are calculated from the lifetimes via equation (5.14).

suitable basis for the required accuracy. Alternatively, and better for our purposes, it can be determined experimentally via the relation<sup>15</sup>

$$\Gamma_{J,J'} = \frac{\omega_0^3}{3\pi\epsilon_0\hbar c^3} \frac{2J+1}{2J'+1} |\langle J \parallel e\mathbf{r} \parallel J' \rangle|^2 \quad (5.14)$$

where  $\Gamma_{J,J'}$  is the spontaneous decay rate from the fine structure manifold  $J'$  to a lower state  $J$ . The factor  $(2J+1)/(2J'+1)$  accounts for the degeneracy of the fine structure manifolds. These decay rates may be measured and thus used to derive transition dipole matrix elements. Lifetimes and dipole matrix elements for the transitions relevant to our model are listed and referenced in table 5.2.

### 5.3.3 Selection Rules

An additional benefit of the Wigner-Eckart theory is that the coefficients vanish unless certain conditions are met, meaning that forbidden transi-

tions can be identified without time-consuming calculation.

In particular, the 3-j symbol in equation (5.12) is zero if the magnetic quantum numbers do not satisfy the relation  $m_F = m'_F + q$  for  $q \in \{-1, 0, 1\}$ . The full hyperfine selection rules are

$$\begin{aligned} F' &= F \text{ or } F' = F \pm 1 \\ m'_F &= m_F \text{ or } m'_F = m_F \pm 1 \\ F' &\neq F \text{ if } m'_F = m_F. \end{aligned} \tag{5.15}$$

### 5.3.4 The Interaction Hamiltonian

Now that we have expressed the transition dipole matrix elements, we can put together the dipole operator and form the interaction Hamiltonian.

To begin with we will consider a single fine structure transition, coupling a lower energy manifold  $nJ$  to a higher energy manifold  $n'J'$ . This could for example represent coupling just on the D2 transition from  $5^2S_{1/2}$  to  $5^2P_{3/2}$ . We will be able to extend the analysis to further levels later.

The projection operators for the sublevels in a given manifold can now be summed over the hyperfine quantum numbers and the magnetic sublevel indices, and expressed as

$$\begin{aligned} P &= \sum_{Fm_F} |Fm_F\rangle \langle Fm_F| \\ P' &= \sum_{F'm'_F} |F'm'_F\rangle \langle F'm'_F|. \end{aligned} \tag{5.16}$$

Our restricted Hilbert space then consists of the two coupled manifolds.

The identity is  $P + P'$  and the dipole operator is then given by

$$d_q = (P + P')d_q(P + P') \quad (5.17)$$

$$= Pd_qP' + Pd_qP' \quad (5.18)$$

$$= d_q^{(+)} + d_q^{(-)}. \quad (5.19)$$

We then expand these terms with (5.16) to find

$$\begin{aligned} d_q^{(+)} &= Pd_qP' \\ &= \sum_{Fm_F F'm'_F} \langle Fm | d_q | F'm'_F \rangle | Fm_F \rangle \langle F'm'_F | \end{aligned} \quad (5.20)$$

and then introduce the reduced dipole matrix element from (5.13) to obtain

$$\begin{aligned} d_q^{(+)} &= \sum_{Fm_F F'm'_F} \langle J \| e\mathbf{r} \| J' \rangle (-1)^{F'+J+1+I} \sqrt{(2F+1)(2J+1)} \left\{ \begin{array}{ccc} J & J' & 1 \\ F' & F & I \end{array} \right\} \\ &\times \langle Fm_F | F'm'; 1q \rangle | Fm_F \rangle \langle F'm'_F |. \end{aligned} \quad (5.21)$$

Applying the same for  $d_q^{(-)}$  one can show that

$$d_q^{(-)} = (-1)^q (d_q^{(+)})^\dagger. \quad (5.22)$$

It is useful to define a weighted lowering operator to account for the angular dependence factors

$$\begin{aligned} \Sigma_q &= \sum_{Fm_F F'm'_F} (-1)^{F'+J+1+I} \sqrt{(2F+1)(2J+1)} \left\{ \begin{array}{ccc} J & J' & 1 \\ F' & F & I \end{array} \right\} \\ &\times \langle Fm_F | F'm'; 1q \rangle | Fm_F \rangle \langle F'm'_F | \end{aligned} \quad (5.23)$$

which then allows us to write the dipole operator as

$$\begin{aligned} d_q &= d_q^{(+)} + d_q^{(-)} \\ &= \langle J \| e\mathbf{r} \| J' \rangle [\Sigma_q + (-1)^q \Sigma_{-q}^\dagger] \end{aligned} \quad (5.24)$$

The interaction Hamiltonian, in the same way we derived in chapter 2 for the two-level description, becomes

$$\mathcal{H}_\Omega = - \left( \mathbf{d}^{(+)} \cdot \mathcal{E}^{(-)} + \mathbf{d}^{(-)} \cdot \mathcal{E}^{(+)} \right). \quad (5.25)$$

We define the fine structure manifold Rabi frequency as

$$\Omega_q := \frac{\langle J \| e\mathbf{r} \| J' \rangle E_q^+(0)}{\hbar} \quad (5.26)$$

such that the interaction Hamiltonian can be written in the simple form

$$\mathcal{H}_\Omega = \frac{\hbar}{2} \sum_q \left[ \Omega_q^* \Sigma_q + \Omega_q \Sigma_q^\dagger \right] \quad (5.27)$$

Now for the two-photon Y-configuration, we have more than one transition to consider, as was illustrated in figure 5.4. Using the same indexing as before, with levels  $\{5^2S_{1/2}, 5^2P_{3/2}, 5^2D_{3/2}, 5^2D_{5/2}\}$  represented by  $i = 0, 1, 2, 3$  respectively, we can write the total interaction part of the Hamiltonian as

$$\mathcal{H}_\Omega = \frac{\hbar}{2} \sum_q \left[ \Omega_{01,q}^* \Sigma_{01,q} + \Omega_{12,q}^* \Sigma_{12,q} + \Omega_{13,q}^* \Sigma_{13,q} + \text{h.c.} \right] \quad (5.28)$$

The total Hamiltonian is then given by

$$\mathcal{H} = \mathcal{H}'_0 + \mathcal{H}_\Omega. \quad (5.29)$$

### 5.3.5 Spontaneous Decay and the Master Equation

At this point we have defined all the necessary parameters required to follow coherent evolution of the atomic system during the atom light interaction. We recall that the set of equations we hope to solve are those defined by the Lindblad master equation, derived in appendix A,

$$i\hbar \frac{\partial \rho}{\partial t} = [\mathcal{H}, \rho] + \mathcal{L} \{\rho\} \quad (5.30)$$

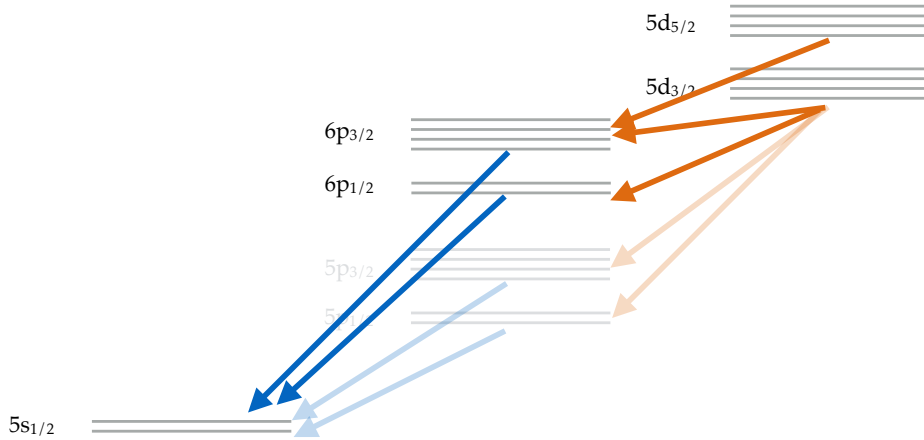


FIGURE 5.5 Decay channels of selected hyperfine manifolds in rubidium. Blue fluorescence is from the decay from  $6^2P_{1/2}$  and  $6^2P_{3/2}$  to the  $5S$  ground state. The  $6P$  states in this model are populated via decay from the  $5^2D_{3/2}$  and  $5^2D_{5/2}$  states. Branching from  $5^2D_{3/2}$  down to the  $5P$  states and from the  $5P$  states to the  $5S$  ground state are also included in the model.

where the Lindblad term accounting for dissipation is given by

$$\mathcal{L}\{\rho\} = \sum_j C_j \rho C_j^\dagger - \frac{1}{2} (\rho C_j^\dagger C_j + C_j^\dagger C_j \rho). \quad (5.31)$$

Our remaining task is to define the set of collapse operators  $C_j$  for the system defining spontaneous decay of excited states to lower states, including the included angular momentum structure. We are able to use the same lowering operator  $\Sigma_q$  to account for the branching factors to each hyperfine sublevel, and the collapse operators are then given by

$$C_{J' \rightarrow J} = \sqrt{\Gamma_{J,J'}} \left( \frac{2J'+1}{2J+1} \right) \sum_q \Sigma_q \quad (5.32)$$

for each decay channel  $J' \rightarrow J$  allowed by fine structure selection rules.

The allowed decay channels for the manifolds included in our model are illustrated in figure 5.5. It is important to note that the  $6P$  states in fact have decay channels to states other than the ground state  $5^2S_{1/2}$  which

are not included in this model. We here assume that all of the 6P population decays via a single channel to the ground state. The decay widths  $\Gamma_{J,J'}$  are given in table 5.2.

#### 5.4 Numerical Results

#### 5.5 Discussion

# *6 Propagation of Short Pulses in V-Type Atoms*

## *6.1 Introduction*

In previous chapters we have investigated a subset of the fascinating array of phenomena that have been studied in the propagation of resonant optical beams in three-level media. We looked at the extension of the well-known effect of SIT and optical solitons to multtons in V-type media in chapter 3, and the propagation of dark-state polaritons under EIT conditions in  $\Lambda$ -type media in chapter 4.

In this chapter we return our attention to the propagation of light through atoms in the V-type system. Our motivation for this theoretical investigation is recent experimental work at Durham into coherent atomic dynamics on the sub-nanosecond timescale in thin (on the order of a micron in length) vapour cells.<sup>53</sup> The experiment is designed to investigate the effect on susceptibility of a medium with respect to a probe beam when significant population has been transferred into an excited state via a second, strong pulse.

If the two pulses were of the same wavelength, addressing the same transition, it would be experimentally difficult to separate detection of the probe signal in order to determine how its propagation had

been affected. In addition, the decay time of the excited state (on the order of nanoseconds) is too short for the pulses to be well-separated in time while maintaining the required population transfer in the medium. Thus, a second laser on a separate wavelength is used for the coupling field.

Similar systems have been designed to transfer population on the order of nanoseconds in rubidium vapours, using the  $\Xi$  (ladder) scheme to couple an excited state to a higher Rydberg state.<sup>54,55</sup> However, the optical power required is prohibitively large due to the weak transition strength, so the experiment makes use again of the V-type configuration, coupling the ground state of rubidium to a pair of non-degenerate excited states.

In the next section we shall briefly describe the experiment and present results, before we go on to describe the theoretical model.

## 6.2 Description of the Experiment

A dense thermal vapour of rubidium atoms in their natural isotopic abundances, contained in a thin cell on the order of a micron in length, is addressed with two co-propagating monochromatic lasers, forming the V-type excitation scheme illustrated in figure 6.1(a). The probe laser is resonant with the D1 transition from the  $5^2S_{1/2}$  ground state to the  $5^2P_{1/2}$  excited state and the coupling laser is resonant with the D2 transition coupling the ground state to the  $5^2P_{3/2}$  excited state.<sup>47,48</sup> The beams are linearly polarised and orthogonal, and following propagation they are separated by a polarising beam splitter.

The  $5^2S_{1/2}$  ground state in rubidium is a doublet state split on the order of GHz,<sup>47</sup> as shown in figure 6.1(b) for  $^{85}\text{Rb}$ . The experimental carrier

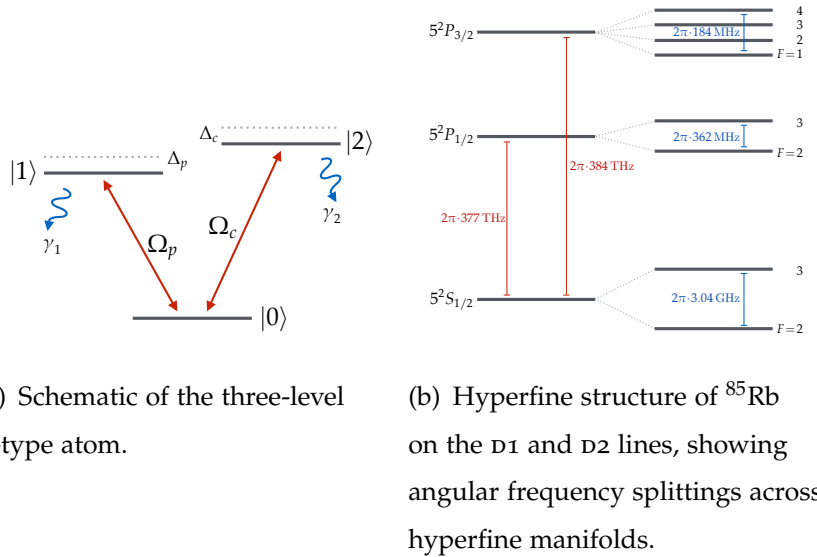


FIGURE 6.1 V configuration level diagrams.

frequencies are tuned resonant with transitions from the  $|5^2\text{S}_{1/2} F=3\rangle$  level for  $^{85}\text{Rb}$  and so are far-detuned from the other energy level in the doublet. The coupling beam is focused to a waist of  $\sim 20 \mu\text{m}$  while the probe beam is focused more tightly to a waist of  $\sim 10 \mu\text{m}$ , which minimises variation of the coupling intensity for atoms in the probe beam.<sup>53</sup>

Transmission of the beams through the medium is detected using a fast photodiode with a bandwidth of 8 GHz input to a 12 GHz bandwidth oscilloscope with an effective sampling rate of  $\sim 400 \text{ GS/s}$ . The oscilloscope is sampling rather than real-time, so the data must be averaged over many cycles. Systematic noise is recorded by taking measurements with the probe laser off and later removing the background from the measured signal.

The cell windows alter the focusing region of the beams, and so spectroscopic measurements are needed to establish accurate Rabi frequencies. The Rabi frequency of the coupling beam atom-light interaction is measured using the Autler-Townes splitting of the ground states. The Rabi frequency of the probe beam is then estimated using the coupling beam

as a guide.

Results were taken over a range of peak intensities for the coupling pulse of 10 to 100 mW and over a vapour temperature range of 200 to 300 °C. In all cases the coupling pulse is shaped to a short Gaussian profile with a FWHM of 0.8 ns. This shaping is performed by a Pockels cell placed between two crossed Glan-Taylor prisms to rapidly rotate the polarisation of the beam.

The experiments were performed and results taken by Kate A. Whitaker and James Keaveney. Further details of the experimental setup may be found in Keaveney, 2013.<sup>53</sup>

### 6.2.1 Experimental Results

In figure 6.2 we see an example result for probe field transmission from the experiment described. The change in signal detected is plotted against time. In this case the temperature  $T = 200\text{ }^{\circ}\text{C}$  and the cell length  $L = 2\text{ }\mu\text{m}$ . The coupling pulse has a peak power of 82 mW and is centred at  $t = 0$ . The coupling pulse plotted is an average of many shots, but there is practically no variation in the pulse shape from shot to shot.

We see the probe transmission peak sharply around 0.5 ns before the maximum of the coupling pulse, which suggests a superluminal propagation effect, perhaps due to a negative refractive index in the medium.<sup>56</sup> There is a brief, smaller oscillation before the transmission returns to its original level. The input pulse profile applied in the experiment has an additional ‘bump’ as an artefact of the way the pulse is shaped (this can be seen in the grey pulse shape).

In figure 6.3 we show the recorded change in signal over a range of temperatures from 200 °C to 290 °C. The coupling pulse has a peak optical power of 82 mW and is centred at  $t = 0$ . For clarity the data has been

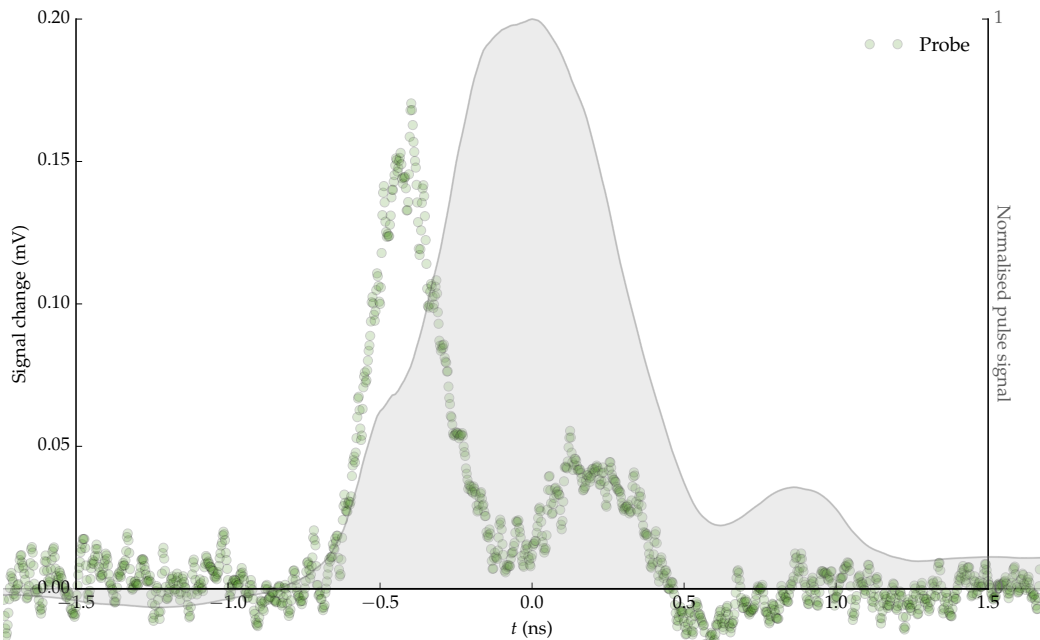


FIGURE 6.2 Recorded probe transmission against time (green circles). The resonant coupling pulse intensity (grey filled area), shown after it has passed through the medium, has a FWHM  $t_w = 0.8 \text{ ns}$ , a peak power of  $82 \text{ mW}$  and is centred at zero. The temperature  $T = 200^\circ\text{C}$  and the cell length  $L = 2 \mu\text{m}$ .

smoothed using a moving average with a triangular weighting function.

We see that over the range of temperatures investigated at this power, the steep early response is consistent in time and that the peak of the response increases with temperature in an approximately linear way, with possible saturation of that increase at  $290^\circ\text{C}$ .

In order to understand the distinctive response profile of the signal and determine the physical principles underlying these results, we will now begin building up a theoretical model for the system.

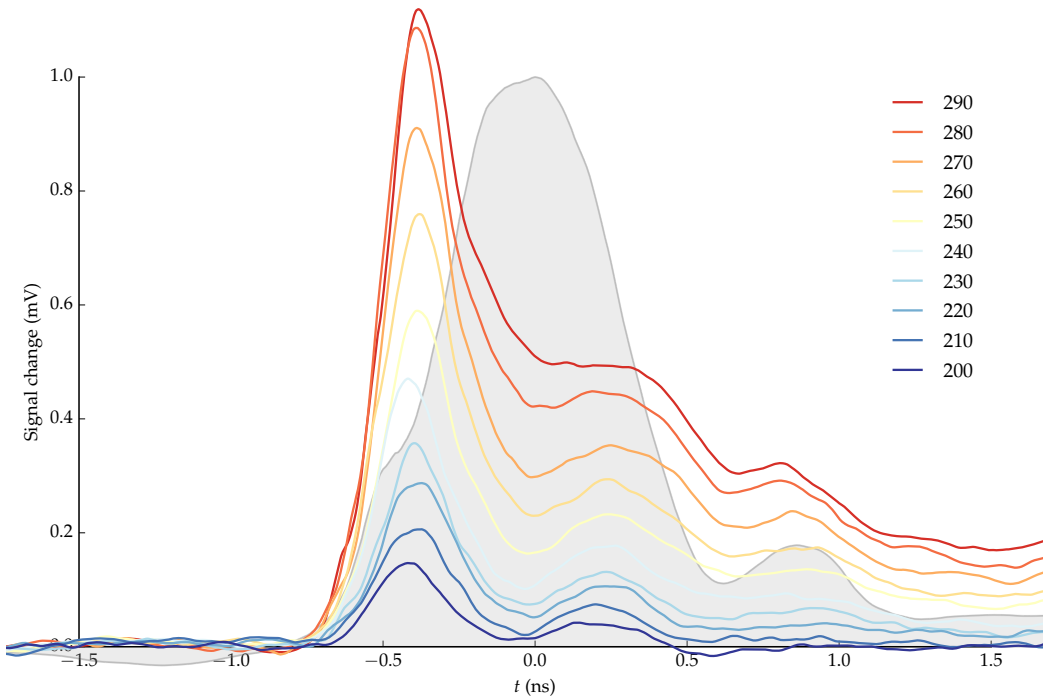


FIGURE 6.3 Recorded probe signal against time (coloured lines) over a range of temperatures from  $T = 200\text{ }^{\circ}\text{C}$  to  $290\text{ }^{\circ}\text{C}$ . The resonant input coupling pulse intensity, shown for the experiment at  $T = 200\text{ }^{\circ}\text{C}$  (grey filled area) in each case has a width  $t_w = 800\text{ ps}$ , is centred at zero and has a peak optical power of 82 mW. The pulse is shown here normalised for time reference.

### 6.3 Theoretical Model

We start with a quantised three-level atom as illustrated in figure 6.1(a). The probe beam couples the ground state  $|0\rangle$  to an excited state  $|1\rangle$  while an orthogonal coupling beam couples  $|0\rangle$  to an adjacent excited state  $|2\rangle$ . The transition  $|1\rangle$  to  $|2\rangle$  is dipole-forbidden, completing the definition of the V-type atom. With this simplified model of the atomic system, we are neglecting the hyperfine structure of the  $5^2\text{S}_{1/2}$ ,  $5^2\text{P}_{1/2}$  and  $5^2\text{P}_{3/2}$  states. We will discuss this approximation further in section 6.6.

The total electric field vector for the two laser beams is described by

$$\mathbf{E}(z, t) = \left[ \frac{1}{2} \hat{\mathbf{x}}_p \mathcal{E}_p(z, t) e^{i(k_p z - \omega_p t)} + \frac{1}{2} \hat{\mathbf{x}}_c \mathcal{E}_c(z, t) e^{i(k_c z - \omega_c t)} + \text{c.c.} \right] \quad (6.1)$$

where  $\hat{\mathbf{x}}_p$  and  $\hat{\mathbf{x}}_c$  are orthogonal polarisation of the vectors of the fields and the envelopes  $\mathcal{E}_p$  and  $\mathcal{E}_c$  are in general complex functions. We define corresponding Rabi frequencies  $\Omega_p = d_{01}\mathcal{E}_p/\hbar$  and  $\Omega_c = d_{02}\mathcal{E}_c/\hbar$  where  $d_{0j}$  is the dipole moment between levels  $|0\rangle$  and  $|j\rangle$ , which we take parallel to its respective field polarisation.

The Hamiltonian for the V-type three-level atom interacting with these two classical fields is

$$\mathcal{H}_V = -\hbar(\Delta_p \sigma_{11} + \Delta_c \sigma_{22}) - \frac{\hbar}{2} [(\Omega_p \sigma_{10} + \Omega_c \sigma_{20}) + \text{h.c.}] \quad (6.2)$$

within the dipole approximation and in the frame rotating with the frequencies of the optical fields. Here  $\sigma_{ij} := |i\rangle \langle j|$  is the transition operator. Along with accounting for off-resonant fields, the inclusion of detunings  $\Delta_p$  and  $\Delta_c$  allows us to consider Doppler broadening via an atom distribution  $P(\Delta)$  as described in chapter 2.

Armed with this Hamiltonian we can apply the semiclassical Maxwell-Bloch propagation models described in chapter 2 to solve for the electric fields  $\mathcal{E}_{p,c}$  and atomic density operator  $\rho$  over  $z$  and  $t$  as the fields move through the medium.

The temporal profile of the cw probe and Gaussian pulsed coupling input at the front of the medium ( $z=0$ ) constitute the necessary boundary condition on the fields.

Switching on the cw probe field instantaneously from zero to  $\Omega_{p0}$  would introduce a discontinuity and thus spurious ringing due to the Gibbs phenomenon.<sup>18</sup> We thus construct a switch-on function which

ramps up smoothly. We take a real-valued  $\Omega_p$  function

$$\Omega_p(z=0, t) = \begin{cases} \Omega_{p0} \exp \left[ -4 \log 2 \left( \frac{t-t_0}{t_w} \right)^2 \right] & t < t_0 \\ \Omega_{p0} & t \geq t_0 \end{cases} \quad (6.3)$$

where  $t_0$  is the point at which the function reaches its peak  $\Omega_{p0}$ . The duration of the ramp-on is governed by  $t_w$ , which is the full width at half maximum (FWHM) of a Gaussian. We also require an initial condition for the atomic states, where it is reasonable to assume negligible population in either of the excited states.

The interaction Hamiltonian allows us to follow coherent evolution of pure atomic states. To our analysis we will also include the interaction of atoms with the environment via spontaneous decay of excited states. We'll still be considering coupling pulses much shorter than the decay time associated with this decay as discussed in chapter 3.

The spontaneous decay effect is included in the model via collapse operators  $C_j$  in the Lindblad equation (2.29) describing time evolution of the atomic states. For the V configuration atom we have  $C_j = \sqrt{\Gamma_{0j}}\sigma_{0j}$  for  $j \in \{1, 2\}$  representing spontaneous decay of the excited states, where  $\Gamma_{0j}$  are the decay rates.

### 6.3.1 Simulation Results

With this theoretical model, we are now in a position to set up and run numerical simulations of the physical system using the Maxwell-Bloch propagation algorithm described in Appendix C.

We present results of an example simulation in figures 6.4, 6.5 and 6.6. In this example we take a rubidium cell of length  $L = 2 \mu\text{m}$  at a temperature  $T = 230^\circ\text{C}$ , which translates to absorption coefficients of  $Ng_{01} = 2\pi 66.7 \Gamma/\text{L}$  and  $Ng_{02} = 2\pi 128 \Gamma/\text{L}$  (see chapter 2 for a de-

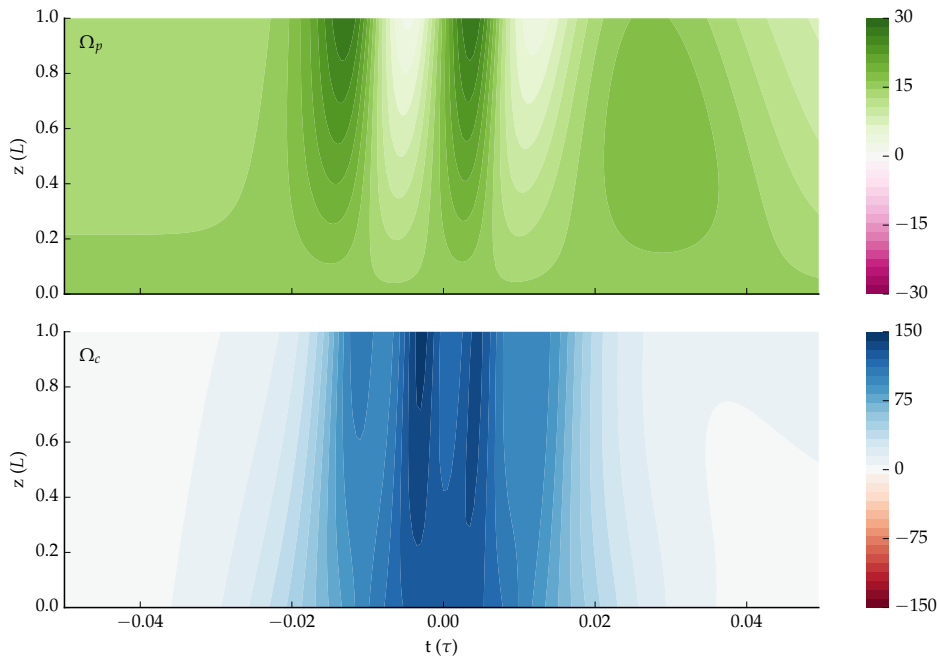


FIGURE 6.4 Real parts of the complex Rabi frequencies  $\Omega_p$  (top) and  $\Omega_c$  (bottom) in the simulated pulse/cw scheme. The coupling pulse has width  $t_w = 0.029 \tau$  and peak  $\Omega_c$  of  $2\pi 130 \Gamma$ . The absorption coefficients are  $Ng_{01} = 2\pi 66.7 \Gamma/L$  and  $Ng_{02} = 2\pi 128 \Gamma/L$ .

scription of the absorption coefficients). Given the decay time  $\tau = 1/\Gamma_{01}$ , the input ( $z = 0$ ) coupling pulse has a FWHM of  $t_w = 0.029 \tau$ , (equivalent to 0.80 ns), a peak of  $\Omega_c = 2\pi 130 \Gamma$  ( $2\pi 748$  MHz) and is centred at  $t = 0$ . The cw probe is ramped up to  $\Omega_p = 2\pi 15 \Gamma$  ( $2\pi 86$  MHz) long enough before the pulse (at  $t = -1.5 \tau$ ) for the system to reach a steady state.

In figure 6.4 we look at the evolution of the fields, as described by the real part of the complex Rabi frequencies  $\Omega_p$  and  $\Omega_c$ , in the time window around the pulse. The contoured colour maps correspond to the real parts of  $\Omega_p$  and  $\Omega_c$  according to the colour scale on the right, with local time  $t'$  on the  $x$ -axis (these results are displayed in the co-moving reference frame) and the distance  $z$  that the fields travel through the medium on the  $y$ -axis. The input boundary conditions are thus represented by a horizontal slice at  $z=0$ .

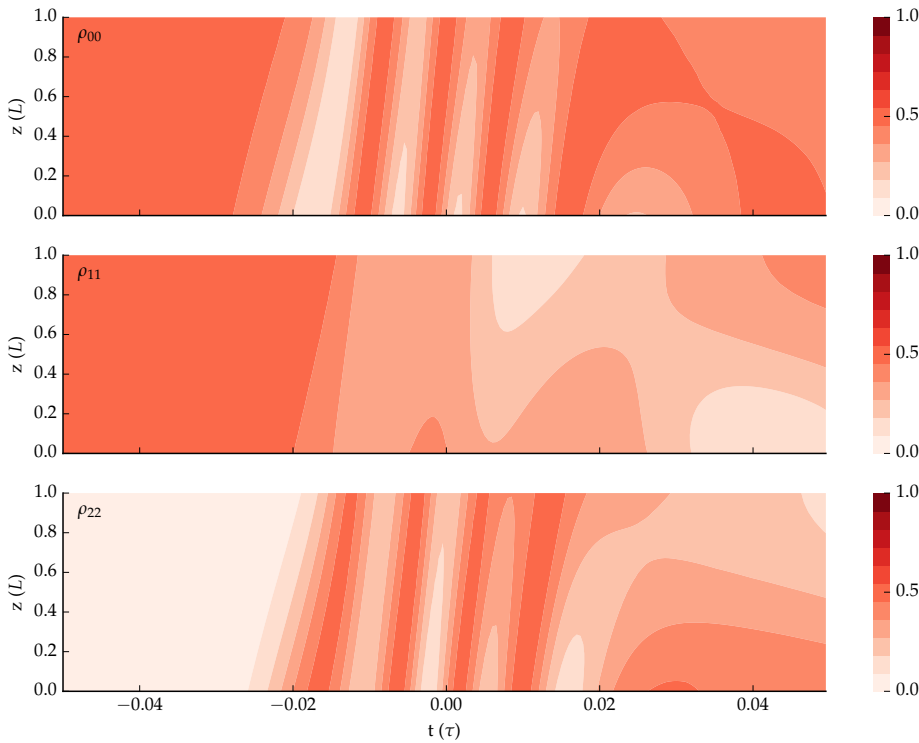


FIGURE 6.5 Populations of the ground state  $\rho_{00}$  (top) and excited states  $\rho_{11}$  (middle) and  $\rho_{22}$  (bottom) over  $z$  and  $t'$  in the simulated pulse/cw scheme, with parameters as those in figure 6.4.

We see that the coupling pulse (bottom) is not attenuated over this distance, but in fact is shaped and is indeed amplified and split around the centre ( $t = 0$ ). A long-time tail emerges towards the end of the medium ( $z = L$ ).

Before the pulse, the cw probe field (top) is attenuated as it progresses through the medium, as we would expect from the usual Beer law of absorption. This behaviour is abruptly disturbed by the coupling pulse, however. In response to the arriving pulse, the probe field is first amplified over a period of about  $0.01 \tau$  and then strongly attenuated, and this process repeats twice over the duration of the pulse. After the pulse the field returns to its initial state.

In figure 6.5 we look at the evolution of the atomic populations of the

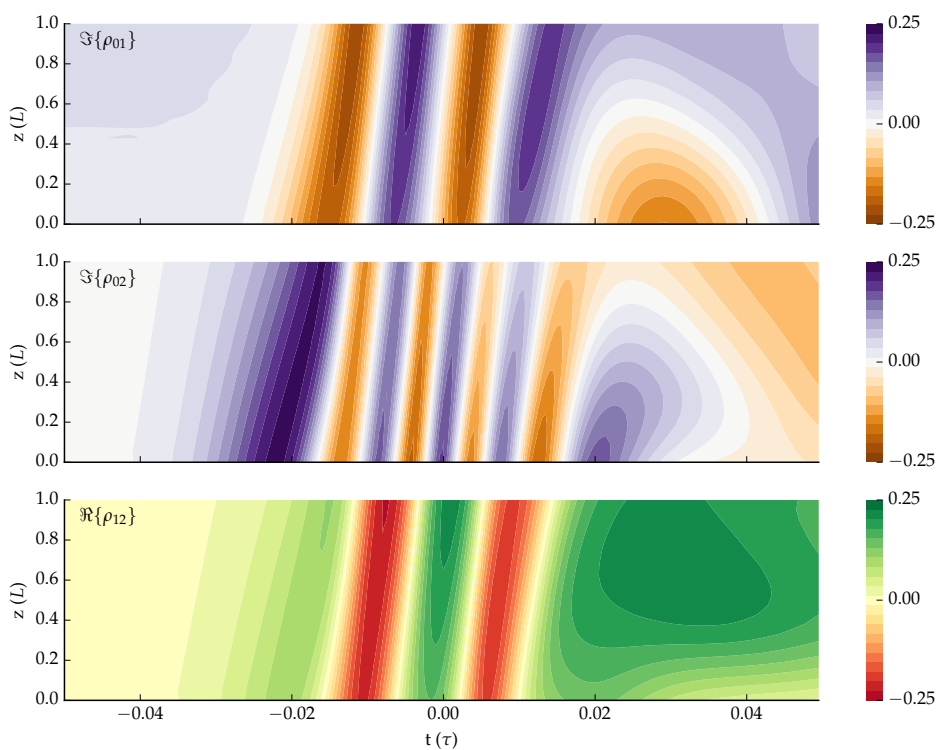


FIGURE 6.6 Selected coherences of the atomic density matrix. The imaginary parts of  $\rho_{01}$  (top) and  $\rho_{02}$  (middle) and the real part of  $\rho_{12}$  (bottom) over  $z$  and  $t'$  in the simulated pulse/cw scheme, with parameters as those in figure 6.4.

states  $|0\rangle$ ,  $|1\rangle$  and  $|2\rangle$  during the same window as figure 6.4, with local time  $t'$  on the  $x$ -axis and the distance  $z$  that the fields travel through the medium on the  $y$ -axis. These diagonal elements of the density matrix are real and must sum to unity as expressed in equation (A.4), and so the colour scale is from zero to one on each plot.

We see that the population is initially divided evenly between  $\rho_{00}$  (top) and  $\rho_{11}$  (middle), with no population in the  $|2\rangle$  state, as expected since initially the medium is in the steady state driven on resonance by the cw probe field. During the pulse population is driven between  $\rho_{00}$  and  $\rho_{22}$  (bottom). The population in  $\rho_{11}$  is reduced during the pulse. The small positive slope of these features on each of the colour maps shows the pulse arriving later in time relative to the speed-of-light frame as the fields move through the medium. This corresponds to a slow-light refractive index (see chapter 4).

In figure 6.6 we look at the evolution of the off-diagonal density matrix elements during the same window. Some interesting behaviour of the system is demonstrated here. The top two subplots with orange-to-purple colour maps, show imaginary parts of coherences  $\rho_{01}$  and  $\rho_{02}$  between the ground state and the two excited states. The bottom subplot, with red-to-green colour map, shows the real part of the  $\rho_{12}$  coherence between the two excited states, corresponding to phase coherence between these states.

Firstly, we note that the  $\Im\{\rho_{02}\}$  coherence (middle) makes around four complete oscillations during the pulse, corresponding to the strong driving field. Secondly,  $\Im\{\rho_{01}\}$  (top) makes around two oscillations but out-of-phase with  $\Im\{\rho_{02}\}$  such that it is first driven negative. Finally,  $\Re\{\rho_{12}\}$  (bottom) is nonzero such that there is a real coherence between the two excited states despite them not being coupled directly. This oscillates on the same timescale as  $\Im\{\rho_{01}\}$ .

The fact that we see such strong early amplification of the probe field in figure 6.4 suggests that this model includes the cause of the pulse steepening observed in experiment, however there are some important physical mechanisms we should include in order to simulate the system accurately, and we will consider these now.

### 6.3.2 Inhomogeneous Broadening

As the experiments described in section 6.2 involved thermal atoms, in order to compare these results with our numerical simulations we need to include some important averaging and dephasing effects due to the motion of the atoms.

Due to the Doppler effect the motion of the atoms along the  $z$ -axis results in a 1D Maxwell-Boltzmann probability distribution function over detuning<sup>13, 14</sup>

$$f(\Delta) = \frac{1}{u\sqrt{\pi}} e^{-(\Delta/u)^2} \quad (6.4)$$

where the thermal width  $u = kv_w$ . Here  $k$  is again the wavenumber of the quasi-monochromatic field and  $v_w = 2k_B T / m$  is the most probable speed of the Maxwell-Boltzmann distribution for a temperature  $T$  and atomic mass  $m$ .<sup>57</sup>

To include this effect in the field propagation equations, as described in chapter 2, we replace the atomic coherence factor by an integral over the convolution of  $P(\Delta)$  with the atomic coherence now a function of detuning, so that

$$\frac{\partial \Omega_p}{\partial \zeta}(\zeta, \tau) = iN g_{01} \int_{-\infty}^{\infty} \rho_{01}(\zeta, \tau, \Delta) f(\Delta) d\Delta, \quad (6.5a)$$

$$\frac{\partial \Omega_c}{\partial \zeta}(\zeta, \tau) = iN g_{02} \int_{-\infty}^{\infty} \rho_{02}(\zeta, \tau, \Delta) f(\Delta) d\Delta. \quad (6.5b)$$

### 6.3.3 Collision Dephasing

We also consider that a thermal cloud of atoms is randomly distributed and that moving atoms will collide with one another. Transient dipole-dipole interactions between colliding atoms leads to a dephasing of dipoles and an additional broadening. We account for this effect by defining a *self-broadening* coefficient  $\beta$  and a parameter known as the Weisskopf radius<sup>58</sup>

$$r_W = \sqrt{\frac{\beta}{2\pi\bar{v}}} \quad (6.6)$$

where

$$\bar{v} = 2\sqrt{\frac{2}{\pi}}v_w \quad (6.7)$$

is the expected relative speed of a pair of atoms. We may make a *binary approximation*, considering that all collisions involve only two atoms, on the condition that<sup>59</sup>

$$\frac{4\pi}{3}Nr_W^3 < 1 \quad (6.8)$$

which means that in a sphere around any given atom with a radius  $r_W$ , we will expect to find at most one other atom. This dephasing effect is then included via additional off-diagonal decay terms

$$\Gamma_{col,j} = N\beta_j = N\frac{d^2}{3\hbar\varepsilon_0}\sqrt{\frac{2J'+1}{2J+1}} \quad (6.9)$$

where  $2J + 1$  and  $2J' + 1$  are the fine structure multiplicities of the ground and excited states.<sup>45,58</sup> Collision broadening thus has the effect of increasing uncertainty in the off-diagonal terms.

For rubidium thermal vapour we have  $\beta_{D1} = 2\pi 0.73 \text{ MHz } \mu\text{m}^3$  and  $\beta_{D2} = 2\pi 1.03 \text{ MHz } \mu\text{m}^3$  for the D line transitions.<sup>45</sup> The binary approximation then breaks down only at a density of  $N \approx 10^{17} \text{ cm}^{-3}$  corresponding to a temperature of  $T = 360^\circ\text{C}$ , and so is a good approximation across the temperature range of the experiment.

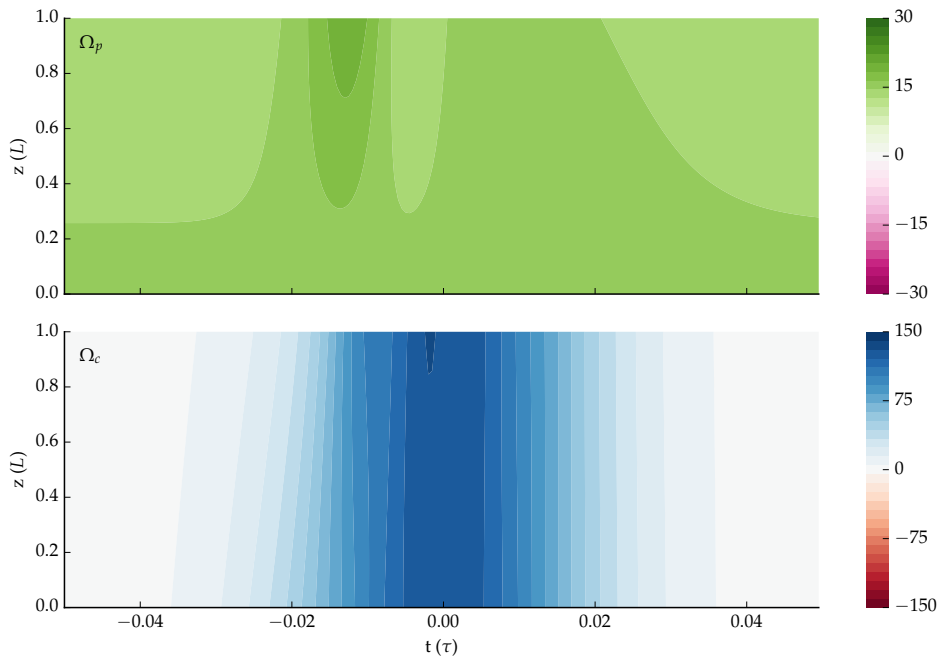


FIGURE 6.7 Real parts of the complex Rabi frequencies  $\Omega_p$  (top) and  $\Omega_c$  (bottom) in the simulated pulse/cw scheme for the parameter set in figure 6.4, with the inclusion of motional effects of Doppler and collision broadening.

In figure 6.7 we again show the evolution of the real part of the complex Rabi frequencies  $\Omega_p$  and  $\Omega_c$  for the model in figure 6.4, but this time with the inclusion of the motional effects described.

We no longer see the level of amplification and splitting on the coupling pulse that we saw in figure 6.4, with the pulse maintaining its profile through the medium. The strong amplification and attenuation on the cw probe field has also been damped significantly, particularly on the second oscillation. The periods of attenuation return the field Rabi frequency to the level observed without the pulse over this distance.

### 6.3.4 Hyperfine Pumping

The final physical mechanism we include in our model is that of optical *hyperfine pumping*, which will affect the propagation of both fields.<sup>60–62</sup>

A rubidium atom with nuclear spin  $I$  has two angular momentum values for the ground state:  $F = I \pm 1/2$ . The hyperfine splitting of this ground state is on the order of GHz, whereas the splitting on the 5P excited states is on the order of MHz, as shown in figure 6.1(b).

If the monochromatic field is tuned to the transition from the lower ground state to the excited state manifold, the higher ground state is far from resonance and so does not couple significantly. The mechanism of decay via spontaneous emission to the higher ground state will then remove atoms from the probe and coupling system.<sup>63</sup>

Atoms that have decayed to the lower ground state are *dark* to the optical fields until they are transferred via collision into the higher ground state. The transit time of atoms in the beam is shorter than the timescale of this transfer by collision so the dark ground state is a sink for atomic population, reducing the effective number density and thus absorption of the fields.<sup>64</sup>

To account for hyperfine pumping, we will add a fourth level as a sink to the three-level system and adjust our initial condition to evenly populate the two ground states. The decay rates  $\Gamma_{01}$  and  $\Gamma_{02}$  to the ground state are then split by branching ratios

$$B_{F \rightarrow J'} = \frac{\sum_{F'} S_{F \rightarrow F'}}{2J' + 1} \quad (6.10)$$

where  $J, F$  are the orbital and hyperfine angular momentum numbers for the ground state and  $J', F'$  are those of the excited state, and the hyperfine strength factors  $S_{F \rightarrow F'}$  are given by<sup>65</sup>

$$S_{F \rightarrow F'} = (2F' + 1)(2J + 1) \begin{Bmatrix} J & J' & 1 \\ F' & F & I \end{Bmatrix}^2. \quad (6.11)$$

In figure 6.8 we compare results from models with and without the addition of hyperfine pumping to a sink state, for the transmission ob-

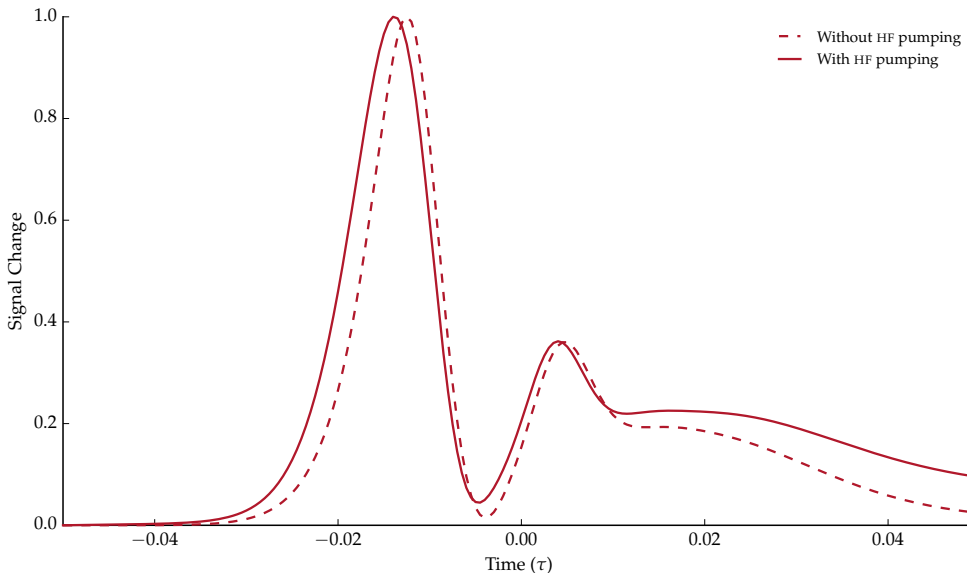


FIGURE 6.8 Simulated transmission intensity at the end of the medium,  $z = 1L$  as the probe responds to the input coupling pulse, without hyperfine pumping (red dashed) and with (solid).

served at the end of the medium,  $z = 1L$ . With the inclusion of pumping, we observe that during the simulation the absorptive power of the medium decreases as population is trapped in the off-resonant dark ground state. This results in an increase in the baseline transmitted signal after the pulse with respect to that beforehand. The peak with the inclusion of HF pumping is slightly earlier, as the slow-light effect of the medium is reduced with the depopulation of the resonant states.

## 6.4 Comparison of Simulation Results with Data

In the previous section we built up a theoretical model for the physical system, including the significant effects of motion and atomic structure, and presented numerical simulations using parameters matching those of the experiment described in section 6.2. We'll now compare the results of those simulations with the experimental data.

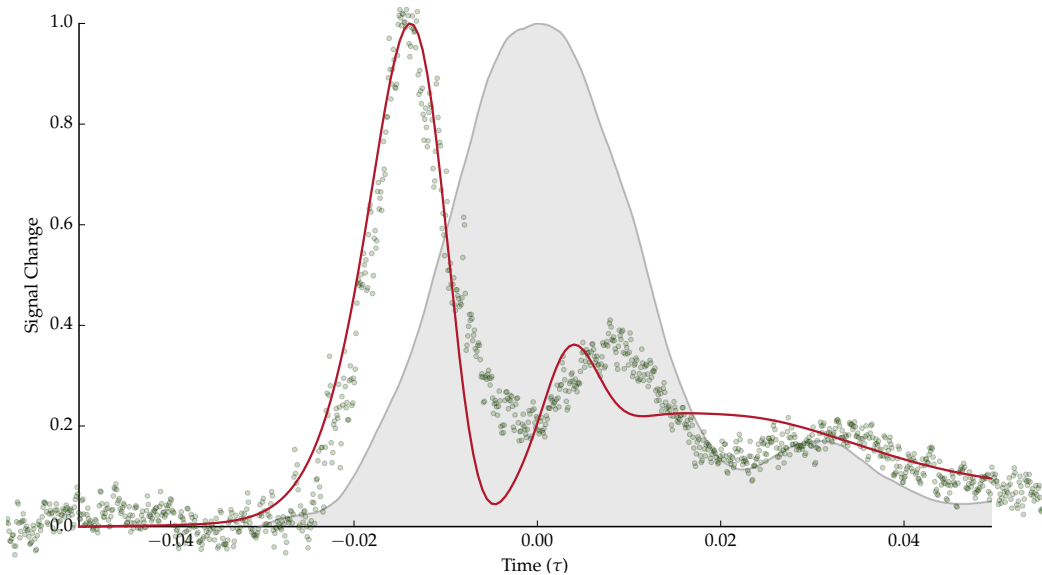


FIGURE 6.9 Comparison of normalised probe transmission profiles from the laboratory data (green circles) and simulation results (red line) for an experiment in the cw/pulse scheme. The measured input coupling pulse intensity (grey filled area) has a width  $t_w = 0.80\text{ ns} \equiv 0.029\tau$ , a peak power of 85 mW and is centred at zero. In this example  $T = 230^\circ\text{C}$  and  $L = 2\mu\text{m}$ .

In figure 6.9 we present again an example of the response in the probe signal (green circles) as a result of the medium being disturbed by the coupling pulse (grey filled area). In this case the temperature  $T = 230^\circ\text{C}$ , the length of the vapour cell  $L = 2\mu\text{m}$  and the peak pulse power is 85 mW. In contrast to figure 6.2, the probe signal is normalised to unity. Overlaid on the data for comparison this time is the simulation result (red line). The simulated coupling pulse matches the experimental width of  $t = 0.029\tau$ .

The only fitted parameter in the simulation is the peak Rabi frequency of the coupling pulse envelope. As we shall see when we look at power dependence, the peak Rabi frequency of the coupling pulse determines the arrival time of the signal response. We here use the arrival time of the experimental signal to fit a simulated peak Rabi frequency  $\Omega_c = 2\pi 130\Gamma$ .

A low-pass filter is applied to the simulation result to account for a limit in resolution of the photon detector of  $2\pi \cdot 8$  GHz. This is effected by a Fourier transform of the intensity profile in the time domain to the frequency domain and removal of frequencies  $|\omega| > \omega_c$  before an inverse transform is made back to the time domain. A sharp cutoff would introduce discontinuities, so instead we apply a convolution with a roll-off frequency curve

$$f(\omega) = \frac{1}{\sqrt{1 + \left(\frac{\omega}{\omega_c}\right)^2}}. \quad (6.12)$$

We see good qualitative agreement with the data. The simple three-level model result shows the distinctive steep rise in the probe transmission, the early peak around  $t = -0.015\tau$  followed by a subsequent, smaller oscillation. The smaller peak arrives early in the simulation, and is narrower than in the data. Both experiment and simulation show the signal returning to its original level beyond  $t = 0.04\tau$ .

The additional ‘bump’ in the pulse profile is the likely cause of a following oscillation in the probe signal. This artefact is not included in the simulation is not observed in the probe signal tail.

#### 6.4.1 Power Dependence

In figure 6.10 we present results for the probe transmission signal over a range of experimental coupling pulse powers from 20 mW to 100 mW. The input pulse in each case has a FWHM of 0.80 ns, equivalent to  $\tau_w = 0.029\tau$  in the natural unit system.

As discussed in section 6.2, the effective probe and coupling Rabi frequencies for the atom-light interaction in the cell is difficult to determine due to the focussing effect of the cell windows. The peak Rabi frequency in the simulation is therefore fitted for that of the 100 mW data,

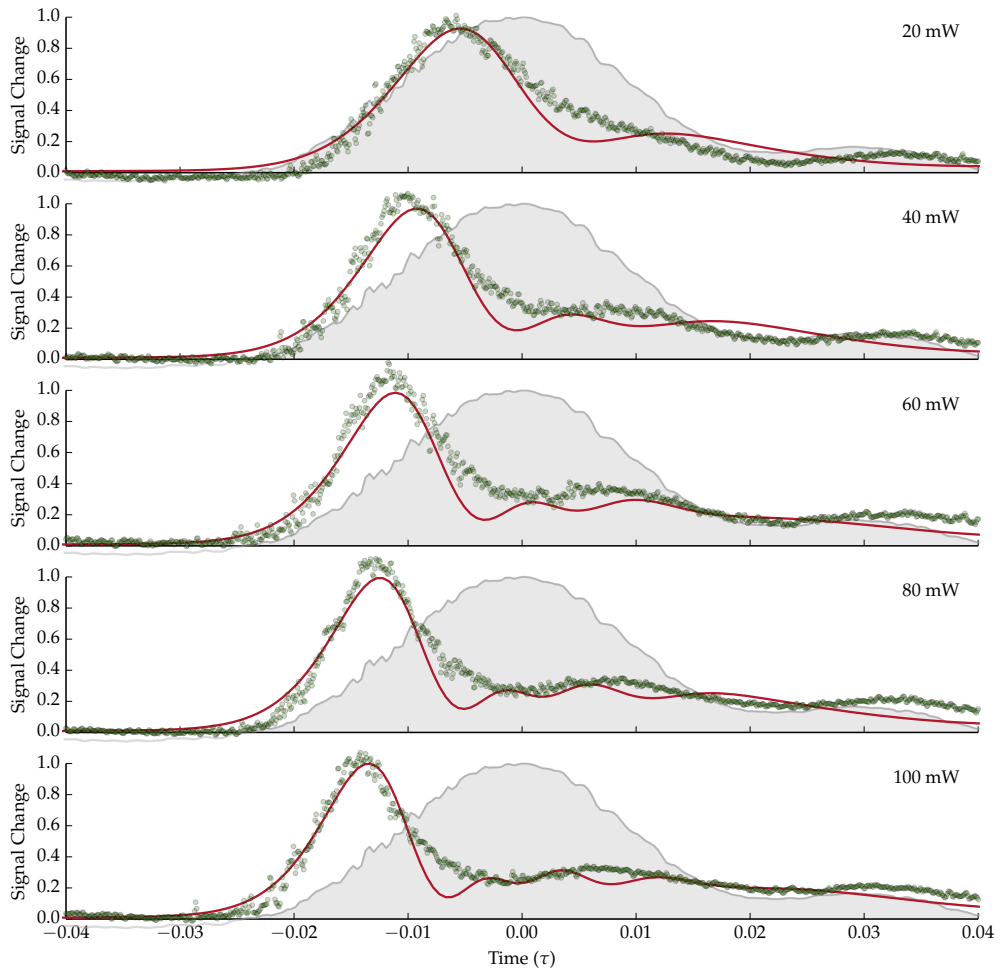


FIGURE 6.10 Comparison of numerical results (red) with experimental data (green circles) for the normalised transmitted probe signal at  $L = 2 \mu\text{m}$  over a range of peak coupling pulse powers. The measured coupling pulse signal (grey filled area) has a width  $\tau_w = 0.80 \text{ ns} \equiv 0.029 \tau$  in each case, and the 100 mW pulse envelope is shown in each subfigure. The temperature is fixed at 200 °C.

at  $\Omega_c = 2\pi 140 \Gamma$ . This value is approximately half of that which we calculate directly from the laser power, beam waist and transition dipole matrix element for  $^{85}\text{Rb}$ . The difference is reasonable if we take into account our uncertainty in the field amplitude at the site of the atoms due to beam focussing as well as the effective TDME due to hyperfine degeneracy (we will discuss this in section 6.6). The Rabi frequencies for other input intensities are derived from the 100 mW value, following the relationship  $\Omega \propto \sqrt{I}$ .

The simulation and experimental data are normalised to the peak intensity in response to the 100 mW run. The response peaks at lower powers are reduced in the data, to 0.93 in the 20 mW run. This is matched in the simulation. The key feature of increasing power is to *push the response peak earlier* relative to the coupling pulse, from around  $-0.08 \tau$  for the 20 mW run to  $-0.15 \tau$  for the 100 mW run, and to *steepen* the peaks. The simulation results also match this behaviour over the power range investigated.

#### 6.4.2 Temperature Dependence

In figure 6.11 we present numerical results for the probe transmission signal in the time window around the pulse ( $t = 0$ ) over a range of temperatures from 200 °C to 282 °C. These simulated results are shown on top of the experimental data for comparison, and the measured coupling pulse for each run is shown (normalised) for reference on the time axis.

We see that there is good qualitative agreement between the simulated result and experimental data across the temperature range. The increase in temperature does not significantly affect the peak time of the response signal, but does linearly increase the peak intensity, and this is

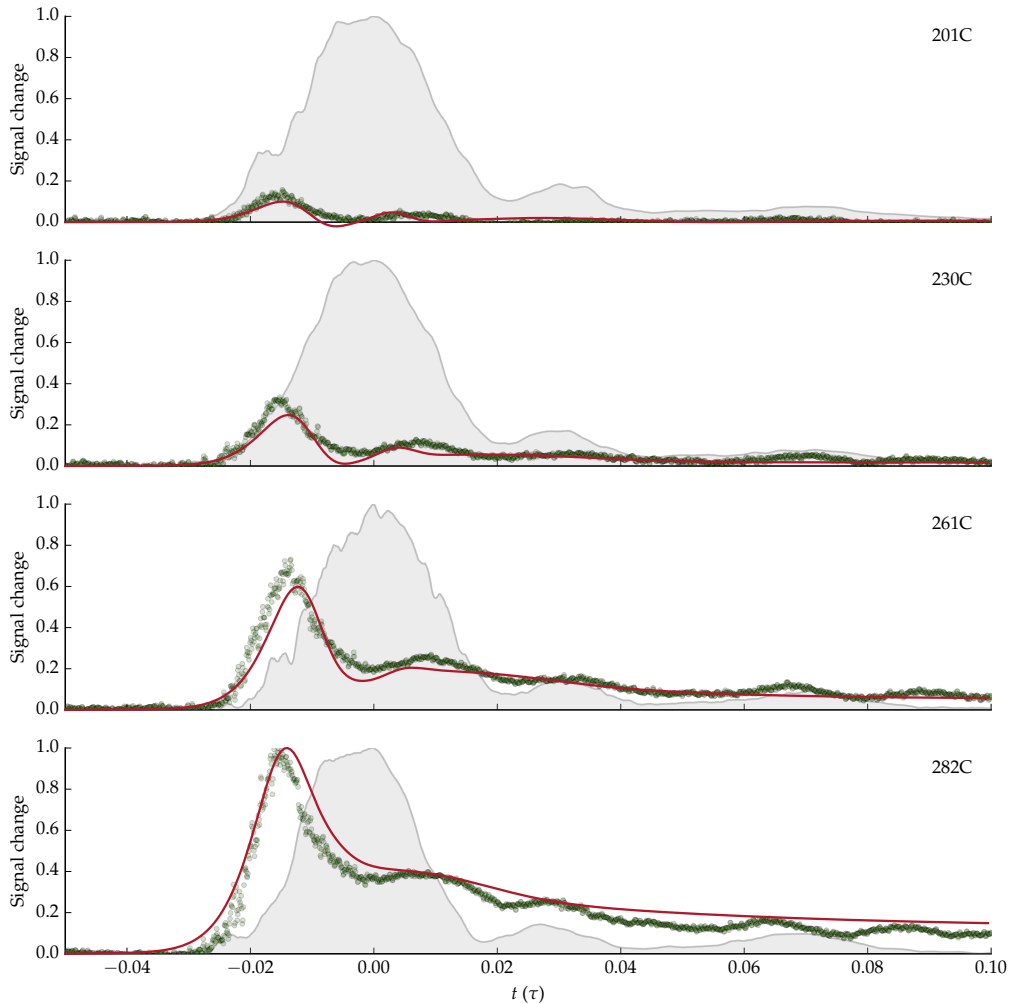


FIGURE 6.11 Comparison of numerical results (red) with experimental data (green circles) for the transmitted probe signal at  $L = 2 \mu\text{m}$  over a range of temperatures from  $200^\circ\text{C}$  to  $282^\circ\text{C}$ . The signals are normalised to the peak of the  $282^\circ\text{C}$  data. The normalised measured coupling pulse signal (grey filled area), shown for comparison, has a width  $\tau_w = 0.80 \text{ ns} \equiv 0.029 \Gamma$  in each case. The coupling pulse power is  $85 \text{ mW}$ .

matched in the simulation. The behaviour of the probe after the pulse has passed is also in reasonable agreement, though there are clear oscillations in the data which are not matched in the simulation.

#### 6.4.3 A Recap

At this point we have built up a theoretical model based on propagation of the fields through a V-type three-level medium, considering important physical effects of inhomogeneous broadening, binary collisions and hyperfine pumping. We've chosen appropriate parameters to compare simulation results with the experimental data and observe a good qualitative fit across the power and temperature parameter space covered in the laboratory study.

Having some trust that our model is useful in matching the experiment, we'd like to gain physical insight into the underlying mechanisms responsible for the observed data. We begin by looking more closely into the response of an individual atom to the applied fields.

### 6.5 Analysis of the Evolution of a Single Atom

In order to understand the steep, early response in the cw probe signal observed in the experiment and matched in the numerical simulations, we turn in this section from the fields to focus on the evolution of the density matrix of a single atom as it is addressed by the probe and subsequently disturbed by the coupling pulse.

As discussed in appendix A, the density matrix  $\rho$  is used to describe the state of an open quantum system such as an atom interacting both with coherent fields and with a stochastically modelled environment. We follow the evolution of  $\rho$  using the Lindblad master equation (A.8).

The Hamiltonian for the V-type atom was given in equation (6.2). In the case of the pulsed coupling scheme, at the front of the medium we have input time-dependent fields  $\Omega_p(t)$  and  $\Omega_c(t)$  and thus a time-dependent Hamiltonian  $\mathcal{H}_V(t)$ . We can solve the Lindblad equation numerically given an initial condition.

We imagine the cw probe having plenty of time to equilibrate before the pulse, so we first find the steady state solution with the probe on and the coupling pulse off. This steady state constitutes the initial condition.

In figure 6.12 we show the time evolution of density matrix populations and coherences for an example Gaussian pulse profile of peak  $100\Gamma$  and width  $0.02\tau_\Gamma$ , where here we'll assume  $\Gamma := \Gamma_{01} = \Gamma_{02}$  and define  $\tau_\Gamma := 1/\Gamma$  as the reciprocal lifetime. The cw probe Rabi frequency is  $50\Gamma$ . Before the pulse, the steady state population is an even split between  $\rho_{00}$  and  $\rho_{11}$ . As the pulse ramps on we see it coherently drive population transfer such that it oscillates between populations  $\rho_{11}$  and  $\rho_{22}$ . This is accompanied by a positive real coherence  $\rho_{12}$ , and an imaginary coherence  $\rho_{01}$  which oscillates first negative and then positive. After the pulse we see damped oscillation of  $\rho_{00}$  and  $\rho_{11}$ , and at long times we expect the system to return to its steady state.

The behaviour of the imaginary part of  $\rho_{01}$  is of particular interest as we know that the macroscopic consequence of this atomic coherence is polarisation of the medium with respect to the probe field, and resulting attenuation or amplification of that field. From the observed evolution we can then predict that during the pulse, without the populations  $|0\rangle$  and  $|1\rangle$  being inverted, we will find reduced absorption and possibly gain in the probe field.

To understand this time evolution, we write out the components of equation (2.29) for the V configuration to get a set of differential equa-

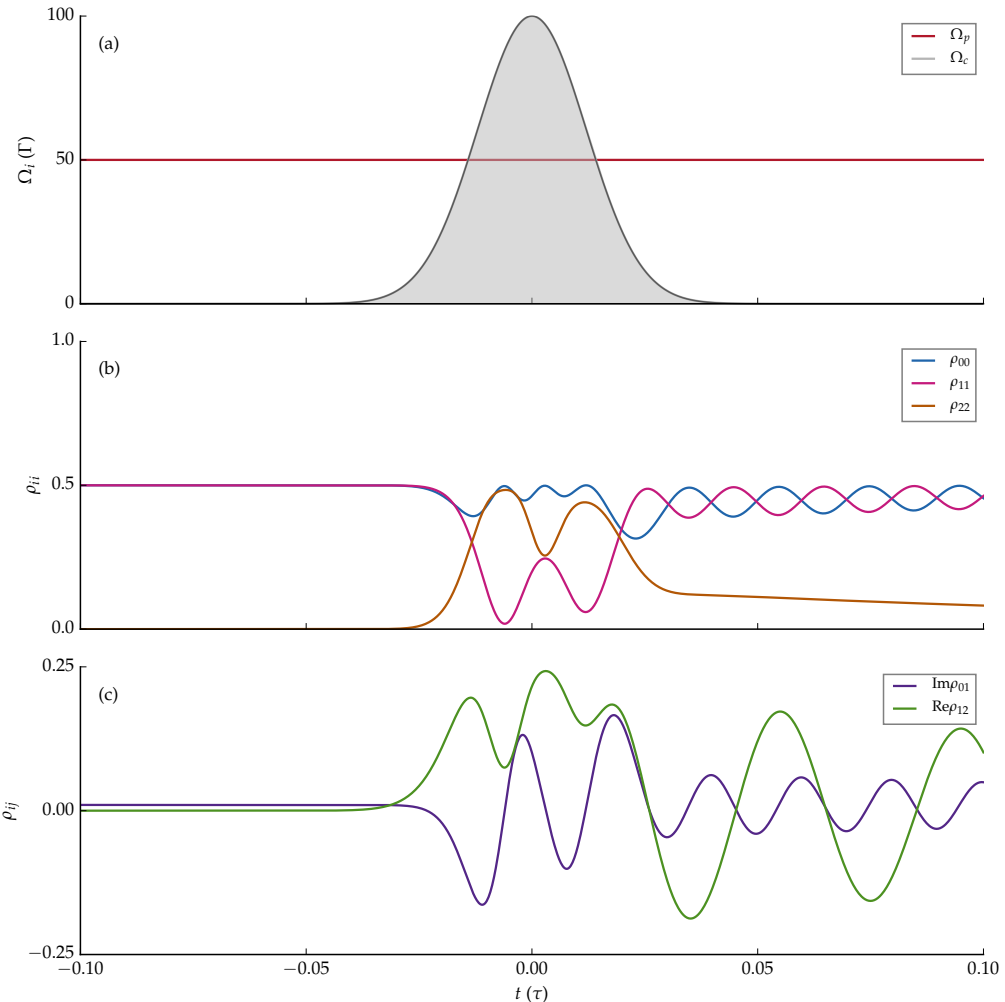


FIGURE 6.12 Time evolution of the density matrix elements from numerical solution of the master equation for the V configuration atom. (a) Rabi frequency profiles of the two fields: a cw probe  $\Omega_p$  (red) and Gaussian pulsed coupling  $\Omega_c$  (grey) with amplitude  $2\pi \times 100\Gamma$  and width  $t_w = 0.02\tau_\Gamma$ . (b) Populations of the atomic eigenstates. (c) The imaginary part of coherence  $\rho_{01}$  (purple) and the real part of coherence  $\rho_{12}$  (green).

tions for the density matrix elements

$$\frac{\partial \rho_{00}}{\partial t} = \Gamma_{01}\rho_{11} + \Gamma_{02}\rho_{22} + \frac{i}{2} \left[ \Omega_p(\rho_{01} - \rho_{10}) + \Omega_c(\rho_{02} - \rho_{20}) \right] \quad (6.13a)$$

$$\frac{\partial \rho_{01}}{\partial t} = -\frac{\Gamma_{01}}{2}\rho_{01} - i\Delta_1\rho_{01} + \frac{i}{2} \left[ \Omega_p(\rho_{00} - \rho_{11}) - \Omega_c\rho_{21} \right] \quad (6.13b)$$

$$\frac{\partial \rho_{02}}{\partial t} = -\frac{\Gamma_{02}}{2}\rho_{02} - i\Delta_2\rho_{02} + \frac{i}{2} \left[ -\Omega_p\rho_{12} + \Omega_c(\rho_{00} - \rho_{22}) \right] \quad (6.13c)$$

$$\frac{\partial \rho_{11}}{\partial t} = -\Gamma_{01}\rho_{11} - \frac{i}{2}\Omega_p(\rho_{01} - \rho_{10}) \quad (6.13d)$$

$$\frac{\partial \rho_{12}}{\partial t} = -\frac{\Gamma_{01}}{2}\rho_{12} - \frac{\Gamma_{02}}{2}\rho_{12} + i(\Delta_1 - \Delta_2)\rho_{12} - \frac{i}{2}(\Omega_p\rho_{02} - \Omega_c\rho_{10}) \quad (6.13e)$$

$$\frac{\partial \rho_{22}}{\partial t} = -\frac{\Gamma_{02}}{2}\rho_{22} - \frac{i}{2}\Omega_c(\rho_{02} - \rho_{20}). \quad (6.13f)$$

Note that  $\rho_{10} = \rho_{01}^\dagger$  and  $\rho_{20} = \rho_{02}^\dagger$ .

Starting with equation (6.13e) we see that in the case of two-photon resonance ( $\Delta_1 = \Delta_2 = 0$ ) and in the steady state at the start of the pulse

$$\frac{\partial \rho_{12}(t_0)}{\partial t} \approx \frac{i}{2}\Omega_c(t_0)\rho_{10}(t_0). \quad (6.14)$$

The steady state  $\rho_{10}$  for the two-level system is positive imaginary, thus  $\rho_{12}$  is initially driven real and positive by the pulse.

If we next look at equation (6.13b), we see that again on resonance and in the steady state with  $\rho_{11} = \rho_{00}$

$$\frac{\partial \rho_{01}(t_0)}{\partial t} \approx -\frac{i}{2}\Omega_c\rho_{21} \quad (6.15)$$

such that with  $\rho_{21}$  real and positive  $\rho_{01}$  is driven imaginary and negative. This is consistent with the behaviour observed in the evolution of coherences in figure 6.12.

### 6.5.1 Coherent Population Trapping

We may gain further insight into the transient effect of the pulse on the system by considering the eigenstates of the atom dressed by the fields,

that is the eigenvectors of  $\mathcal{H}_V$ .<sup>4,27</sup> If we consider equal detunings  $\Delta := \Delta_p = \Delta_c$  and solve for  $\mathcal{H}_V |\psi\rangle = \hbar\lambda |\psi\rangle$  we find eigenvalues

$$\lambda_0 = -\Delta \quad (6.16a)$$

$$\lambda_{\pm} = \frac{-\Delta \pm \bar{\Omega}}{2} \quad (6.16b)$$

where  $\bar{\Omega} = \sqrt{\Omega_p^2 + \Omega_c^2 + \Delta^2}$ . These eigenvalues have corresponding normalised eigenstates

$$|D\rangle = \frac{1}{\sqrt{N_0}} (-\Omega_c |1\rangle + \Omega_p |2\rangle) \quad (6.17a)$$

$$|B_{\pm}\rangle = \frac{1}{\sqrt{N_{\pm}}} (-2\lambda_{\mp} |0\rangle + \Omega_p |1\rangle + \Omega_c |2\rangle) \quad (6.17b)$$

where  $N_0 := \Omega_p^2 + \Omega_c^2$  and  $N_{\pm} := N_0 + 4\lambda_{\mp}^2$ .

Note that the energy eigenvalue  $\lambda_0$  is zero on resonance, such that it is decoupled from the fields. For this reason, its corresponding eigenstate  $|D\rangle$ , which does not contain any component of the ground state, is known as a dark state. Any population entering the dark state cannot be driven out again by the coherent fields, it can only decay spontaneously. This phenomenon is known as coherent population trapping (CPT).<sup>66</sup> The states  $|B_{\pm}\rangle$ , which are coupled to the fields, are known as bright states.

We can transform from the bare state density matrix  $\rho$  to the similar CPT state density matrix  $\rho'$  via

$$\rho' = \mathcal{T}^{-1} \rho \mathcal{T} \quad (6.18)$$

where  $\mathcal{T}$  is the unitary transform defined by equations (6.17).

In figure 6.18, we show the time evolution of the populations of the CPT states  $|D\rangle$  and  $|B_{\pm}\rangle$  during the pulse shown in figure 6.12 for the bare states. We see that during the pulse, a significant amount of population is driven into the dark state  $|D\rangle$ , where it will be trapped. This suggests the effects of the pulse will be counteracted after a short time period.

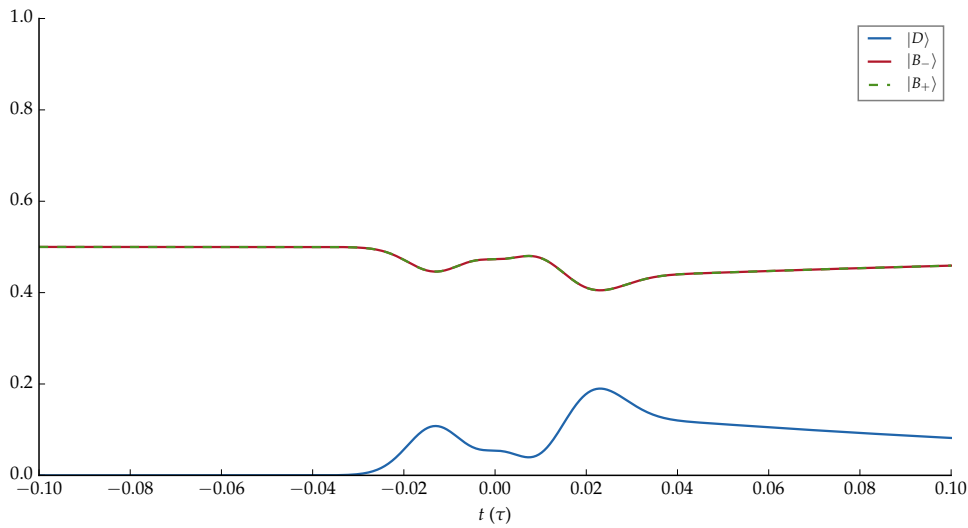


FIGURE 6.13 Time evolution of the populations of the CPT state populations  $|D\rangle$  (blue),  $|B_-\rangle$  (red) and  $|B_+\rangle$  (green dashed) for the V-type atom addressed by a coupling pulse with amplitude  $100\Gamma$  and width  $t_w = 0.02\tau_\Gamma$ .

In summary, in this section we have analysed the time evolution of the atomic states in both the bare and CPT basis during the pulse. We found that the strong pulse drives an oscillation, first negative, in the imaginary part of  $\rho_{01}$ , which we expect to cause a reduction in absorption or even amplification of the probe beam due to the relation of this coherence to the macroscopic polarisation of the medium.

Looking at the CPT basis, we also find that the pulse results in population trapping in the dark state, which does not interact with the fields, and so we expect the reduction in absorption to be short-lived.

These findings are consistent with the observed signal increase in the probe beam during the early part of the pulse. It does not, however, explain the increase in the signal response with increased temperature. For a complete understanding of the behaviour, we will next move on to considering the effects of pulse propagation and investigate what would happen if we extend the simulations to longer propagation distances.

## 6.6 Simulating Longer Propagation Distances

Thus far we have considered the behaviour of the atomic medium as addressed by the cw probe and disturbed by the strong pulse over the propagation distance of the thin cell. The restricted propagation distance is a limit of the current experimental setup, but in our numerical simulations we are not subject to the same constraint. We may extend the propagation medium arbitrarily far to observe what happens to both the atoms and the propagating fields. This will complete our analysis of the observed signal response, and also allow us to make predictions for future laboratory studies.

### 6.6.1 Propagation in the Coupling Pulse Scheme

We will first consider some demonstration cases, before looking at the specific parameters for the experimental system. We know from the study of two- and three-level media in chapter 3 that a key property in the propagation of short pulses in nonlinear systems is the pulse area  $\theta$  defined in equation 3.4. Thus we'll design simulations with fixed input pulse areas, rather than specifying the peak intensities as we have done so far. Of course, for a given Gaussian pulse width, these definitions are interchangeable.

We will for now neglect the motional and hyperfine pumping effects we added to the model in section 6.3, as we seek to gain physical insight into the specific effects of propagation.

In figure 6.14 we present numerical results for the cw probe, coupling pulse scheme in a medium with absorption coefficients set at  $Ng_{01} = Ng_{02} = 2\pi 10^3 \Gamma/L$ . This is an order of magnitude larger than those representing the thin cell experiments, and therefore represents a longer

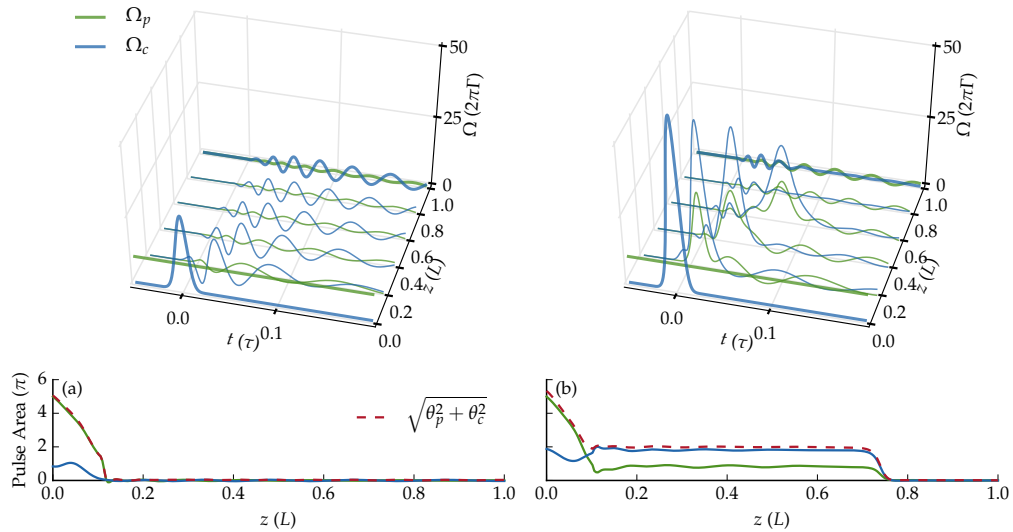


FIGURE 6.14 Propagation of (a)  $0.8\pi$  and (b)  $1.8\pi$  coupling pulses (blue) through a medium addressed by a  $10\Gamma$  cw probe (green), showing (top) profiles of the real part of the complex Rabi frequencies  $\Omega(z, \tau)$  and (bottom) pulse areas  $\theta(z)$ .

distance of propagation. The coupling input pulses are Gaussians of width  $\tau_w = 0.01\tau_\Gamma$  and have pulse areas of (a)  $0.8\pi$  (corresponding to a peak  $\Omega_c = 2\pi 28\Gamma$ ) and (b)  $1.8\pi$  (a peak  $\Omega_c = 2\pi 62\Gamma$ ). In both cases the cw probe is strong with Rabi frequency  $\Omega_p = 2\pi 10\Gamma$ .

In figure 6.14(a) we see that for the  $0.8\pi$  pulse both the cw probe and the coupling pulse are absorbed close to the front of the medium, with the pulse area dissipated by around  $z = 0.1L$ . From then on the only remnant of the fields is the fast ringing.

In figure 6.14(b) we see that for the  $1.8\pi$  pulse, the large coupling pulse kicks up a pulse from the cw field, consistent with our analysis of a period of reduced absorption. Of interest in this long distance simulation is that the resultant probe pulse is able to form its own steady-state soliton, as described in the study of matched pulses in chapter 3. Rather than dissipating entirely, the probe pulse area  $\theta_p$  (bottom, green) is held abruptly at around  $z = 0.1L$  to a value of around  $1\pi$ . The simultane-

ous propagating pulses first steepen toward the sech shape, but then broaden and slow due to the spontaneous decay. We see the large area of the cw probe decreases but doesn't disappear, and the combined pulse area  $\theta = \sqrt{\theta_p^2 + \theta_c^2}$  (bottom, red dashed) finds its steady state at  $2\pi$ . The pulses do not reach the end of the medium in the duration of the simulation, propagating a distance of  $z = 0.7L$ .

We may ask: what does it mean to define a pulse area for an input cw field? For our purposes, we may take it to be arbitrarily large. Numerically, we integrate the Rabi frequency envelope over the duration of the simulation. The key point is that in the case that the combined pulse area is large enough to support simultaneous propagation, this arbitrarily large pulse area does not dissipate but is held.

What happens for stronger pulses? In figures 6.15 and 6.16 we present results for larger-area pulses input on the same medium with the same cw probe field of  $\Omega_p = 10\Gamma$ . The coupling input pulses are again Gaussians of width  $\tau_w = 0.01\tau_\Gamma$ .

In figure 6.15, for the  $4.5\pi$  pulse, we see the coupling pulse break apart as we've seen previously. Again we see that the pulse kicks up a simultaneous pulse in the probe field as the absorption is initially reduced, which allows a small pulse area to move through, and this is carried on by the first resultant  $2\pi$  pulse.

We may understand the reason that only one pulse propagates in the probe field by considering the evolution of the off-diagonal matrix elements we presented in figure 6.6. For every two oscillations in  $\rho_{02}$ , the system evolves through one oscillation in  $\rho_{01}$ . This oscillation forms the probe component of a pulse that matches with the first coupling pulse and propagates as a simulton.

In figure 6.16, for the  $6.5\pi$  pulse, we see that the coupling pulse breaks

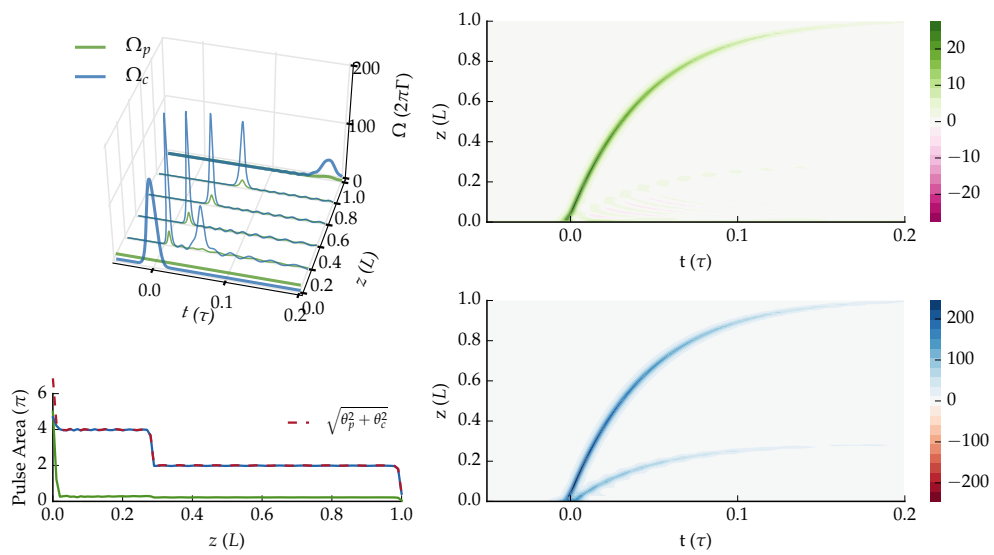


FIGURE 6.15 Propagation of a Gaussian  $4.5\pi$  input coupling pulse with width  $0.01\tau_F$  through a V-type medium addressed by a  $10\Gamma$  cw probe. (Top left) Propagation profile of the probe (green) and coupling (blue) fields. (Bottom left) Pulse areas of the fields and the total area (red dashed). (Right) Colourmaps of the real part of the complex Rabi frequencies  $\Omega_p$  and  $\Omega_c$ .

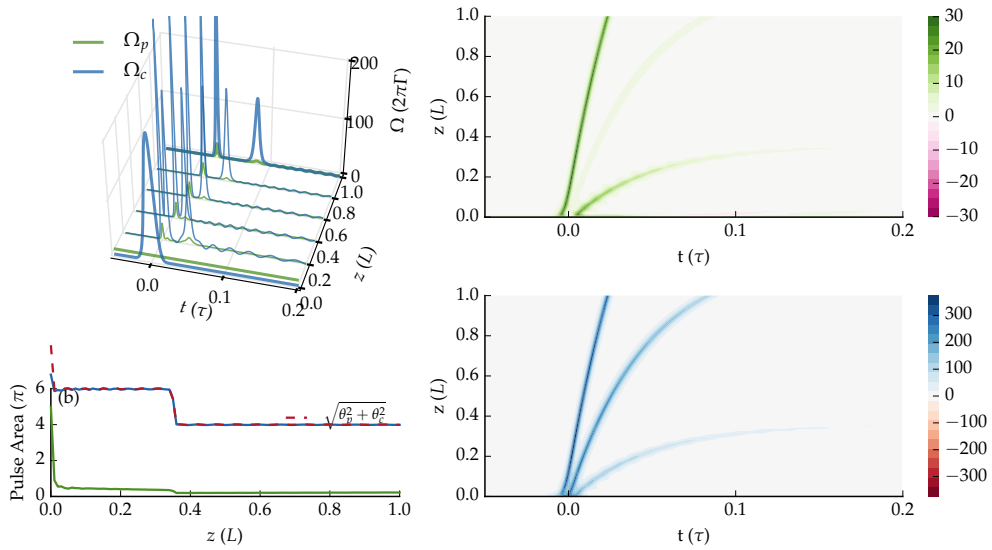


FIGURE 6.16 Propagation of a Gaussian  $6.5\pi$  input coupling pulse with width  $0.01\tau_T$  through the V-type medium addressed by a  $10\Gamma$  cw probe. (Top left) Propagation profile of the probe (green) and coupling (blue) fields. (Bottom left) Pulse areas of the fields and the total area (red dashed). (Right) Colourmaps of the real part of the complex Rabi frequencies  $\Omega_p$  and  $\Omega_c$ .

into three resultant pulses as we'd expect and the kicked up pulse area in the probe field is carried mostly by the first and third resultant  $2\pi$  pulses.

These demonstrative simulations provide an interesting result: a portion of the cw probe field is in fact picked up by the strong pulse and carried along as one or more simultaneous pulses with the same width, at the same velocity, and capable of propagating over long distances.

### 6.6.2 Comparison with Experimental Data

The discovery that a strong coupling pulse has the effect of causing a long-distance propagating soliton in the cw probe leads us to consider the experimental results from the thin cell, using the parameters of section 6.2, but imagining that the cell is longer. Recall that in the case of

transitions on the the rubidium D1 and D2 lines we have distinct values for  $g_{01}$  and  $g_{02}$ , as they are proportional to the square of the respective dipole moments,  $d_{0j}^2$ . This may affect the ability of the pulses to match and propagate.

In figure 6.17 we present again the comparison of numerical result and experimental data shown in figure 6.9. In the experiment the temperature  $T = 230^\circ\text{C}$ , and the peak pulse power is 85 mW, and the same parameters are simulated. We again present the real part of  $\Omega_p$  and  $\Omega_c$  but continue the simulation over a longer distance, imagining that the cell is much longer at  $50 \mu\text{m} \equiv 25 L$ . This will allow us to predict the long-distance behaviour.

The coupling pulse has a large pulse area  $\theta_c = 9.1\pi$ , and so over the longer distance we start to see the same pulse break-up we saw in figures 6.15 and 6.16. Again it is the earliest resultant pulse which carries along a pulse in the probe field, rising before the centre of the pulse at  $t = 0$ . The later resultant pulses in the coupling field are unable to propagate far into the medium due to the dephasing effect of collision broadening.

The simulated result of the field propagation over longer-distances thus gives us an understanding of the mechanism behind the observed transmission profiles in the probe field when the system is disturbed by the strong coupling pulse. We see that *it is the formation of this nascent soliton* in the probe field which causes the steep early in the experimental signal as the probe field is shaped towards a sech-shaped soliton.

It also explains why the peak intensity increases with temperature and number density as observed in figure 6.11, as we are in the nascent stage when the pulse is being shaped. We expect it to saturate as the sech-shape reaches its steady state, and this may be what we see in figure 6.3 at the highest temperature investigated of  $T = 290^\circ\text{C}$ .

### 6.6.3 Hyperfine Structure & Degeneracy

A complete account of the electronic energy level structure of rubidium would include fine and hyperfine structure, as considered for the model in chapter 5. Approximating the rubidium vapour as a three- or four-level atomic medium appears to be justified here on the basis that the simulated transmission profiles provide a good qualitative fit to the data along with physical insight into the underlying coherent mechanism.

The discovery, however, that pulse propagation effects are significant means that the physical structure of the atomic energy levels requires further consideration. This is clear if we consider the pulse area, introduced in chapter 3, which is given by

$$\Theta(z) = \int_{-\infty}^{\infty} \Omega(z, t) dt = \frac{d}{\hbar} \int_{-\infty}^{\infty} \mathcal{E}(z, t) dt. \quad (6.19)$$

This quantity is well-defined only if the atomic levels coupled have a uniquely specified dipole moment  $d$ . We understand that the physical system in fact has this deeper hyperfine structure due to coupling of the electron's orbital angular momentum  $L$ , spin  $S$  and the nuclear spin  $I$ , as shown in figure 6.1(b). An additional concern is that, in the absence of an applied magnetic field, the  $2F + 1$  sublevels of these hyperfine  $F$  levels are spatially degenerate such that there is no straightforward way for these  $m_F$  states to be addressed separately.

The couplings between these degenerate sublevels will then have different dipole matrix elements  $\langle Fm_F | \mathbf{e}\mathbf{r} | F'm'_F \rangle$  and therefore different Rabi frequencies  $\Omega$ , and this can be expected to suppress the formation of coherent optical solitons.

However, in the case of the experimental study of this chapter, the shortness of pulse duration is such that its spectral width is on the order of  $\sim 2\pi$  1 GHz. The hyperfine manifolds of the  $5^2P_{1/2}$  and  $5^2P_{3/2}$  levels are

spread over an energy range on the order of  $\sim 2\pi 100 \text{ MHz}$ , so the pulse interacts with the full manifold of excited state hyperfine levels  $J \rightarrow J'$ , and this excited hyperfine structure is not accessible.

Taking just a single  $J \rightarrow J'$  transition for now, the effective dipole moment for a particular ground state sublevel  $|Fm_F\rangle$  is then found by summing the coupling to all of these excited state sublevels. In general for  $J = 1/2$ ,<sup>67</sup> and in the case of linearly-polarised light coupling levels such that the angular momentum difference  $q = m'_F - m_F = 0$ , we have<sup>65</sup>

$$\sum_{F'} (2F' + 1) (2J + 1) \left\{ \begin{matrix} J & J' & 1 \\ F' & F & I \end{matrix} \right\}^2 |\langle F m_F | F' 1 m_F 0 \rangle|^2 = \frac{1}{3} \quad (6.20)$$

independent of the particular values of  $F$  and  $F'$  such that the effective dipole moment is given by

$$d = \sqrt{\frac{1}{3}} \langle J || e\mathbf{r} || J' \rangle. \quad (6.21)$$

for *every* sublevel  $|Fm_F\rangle$ , where  $\langle J || e\mathbf{r} || J' \rangle$  is the reduced dipole operator for the fine structure transition, which is known experimentally from the natural linewidth.

This factor of  $\sqrt{1/3}$  can be understood as due to spherical symmetry, by considering that the linearly polarised light will interact with only one of the spherical components of the dipole operator.

Then what about the orthogonal, linearly-polarised beam? As we have defined the first transition to be the  $\pi$  ( $q = 0$ ) transition, the orthogonal beam is defined by a polarisation vector  $(\sigma_+ + \sigma_-) / \sqrt{2}$ , a symmetric combination of photons either adding or subtracting a quantum of angular momentum to the atom. By making a summation as in equation (6.20) for the  $q = 1, -1$  transitions, we find the same  $1/\sqrt{3}$  factor, which we would expect again by considering the symmetry of the system.

The result is then for the system to respond as if there were indeed a

unique dipole moment, but one which must take into account the symmetry factor in equation (6.21) and we are justified in applying the simple three-level model.

#### 6.6.4 Weak Probe Fields

Thus far we have considered examples of propagation in the cw probe scheme in which the field is strong. Such strong fields were required in the experiment in order to achieve good detection on the fast photon counter employed. Theoretically, however, we are inclined to consider weak pulses as they may be useful in applications such as quantum information processing and storage.

As described in chapter 3, the pulse area theorem in the case of three-level V-type systems applies not to the individual pulse areas, but to their sum in quadrature. This suggests that if the coupling pulse applied on the adjacent transition is strong, we may be able to consider the scheme for propagation of weak probe through a medium to which it would normally be opaque.

In figure 6.18 we present numerical results which indicate that this is indeed the case. The input Gaussian has a pulse area of  $2.2\pi$ , while the cw probe field has a Rabi frequency of only  $0.001\Gamma$ .

Before the pulse, the probe field is absorbed immediately by the medium. We see that as for the strong probe field, the coupling pulse allows transmission of the probe field. We observe that this weak probe, despite being weak enough to excite only a tiny fraction of the atomic population to the  $\rho_{11}$  state, is able to propagate simultaneously with the coupling pulse just as the strong probe was. The three-level pulse area is nearly all in the coupling field, but the induced pulse in the probe field is not attenuated as it would be were the coupling field not present.

Some high-frequency ringing is seen in the probe field.

Figure 6.19 shows the populations of the atomic states. We see propagation of a  $2.2\pi$  Gaussian input coupling pulse with width that the propagation of the induced pulse in the probe field occurs despite negligible population transfer to the  $|1\rangle$  excited state. The population is nearly entirely transferred from the ground state  $|0\rangle$  to the  $|2\rangle$  excited state.

## 6.7 Discussion

The results presented early on in this chapter, from experiments on a thermal vapour of rubidium atoms addressed by two co-propagating lasers in a vee-type scheme, are certainly intriguing. Over a range of temperatures and powers we observe an early, steep peak in response of the cw probe on the D1 transition when disturbed by a strong, short pulse on the D2 transition.

In order to understand this response behaviour, we designed a theoretical model for the system based on a three-level Maxwell-Bloch description for semiclassical propagation. We included significant physical effects of inhomogeneous Doppler broadening, dephasing due to collisions between moving atoms and hyperfine pumping to a far-detuned state in the ground state doublet. This simple model provides a good qualitative fit to the data over the range of temperatures and powers investigated experimentally, accounting for the peak times of the response relative to power and the relative height of the peak relative to atomic density.

By considering the behaviour of a single atom addressed by the co-propagating fields, both in the bare atomic state basis and the coherent population trapping (CPT) basis, we gain important physical insight

into the transient reduction of absorption in the scheme. Looking then into the effects of non-linear propagation over longer distances, we determine that the steepening of the response is in fact due to the ability of the coupling field to sculpt the pulse toward a sech-shaped soliton. Over longer distances the simulations demonstrate that this probe soliton would propagate simultaneously with the resultant coupling pulse. The tendency of the pulses to separate, having different velocities due to the distinct absorption strengths of the transitions, is overcome by pulse locking.

Notably, the area theorem as applied to multtons allows the propagation even of a weak probe field in this scheme through media it would ordinarily find opaque. Our simulations of weak probes here show such propagation.

In single-field SIT the field must be strong for the propagation of solitons to overcome the weak non-linearity of the medium. But combining this approach with the CPT effect as described here suggests a way around this, and a novel approach to achieving transparent propagation of single or few photon pulses distinct from, but related to, both SIT and EIT.

It should be stressed that the results of the thin cell experiment show the nascent formation of solitons in the cw probe, but for conclusive evidence of multton propagation further investigation is required over longer distances. Balancing the requirement of low collision dephasing widths and high optical depth required may be difficult but we suggest is certainly worth attempting.

Theoretically, for modelling few photon propagation we might wish to look at a quantised field method. An interesting development of the scheme might be in coupling to Rydberg states to introduce interactions between multtons, with applications in quantum information processing.<sup>68–70</sup>

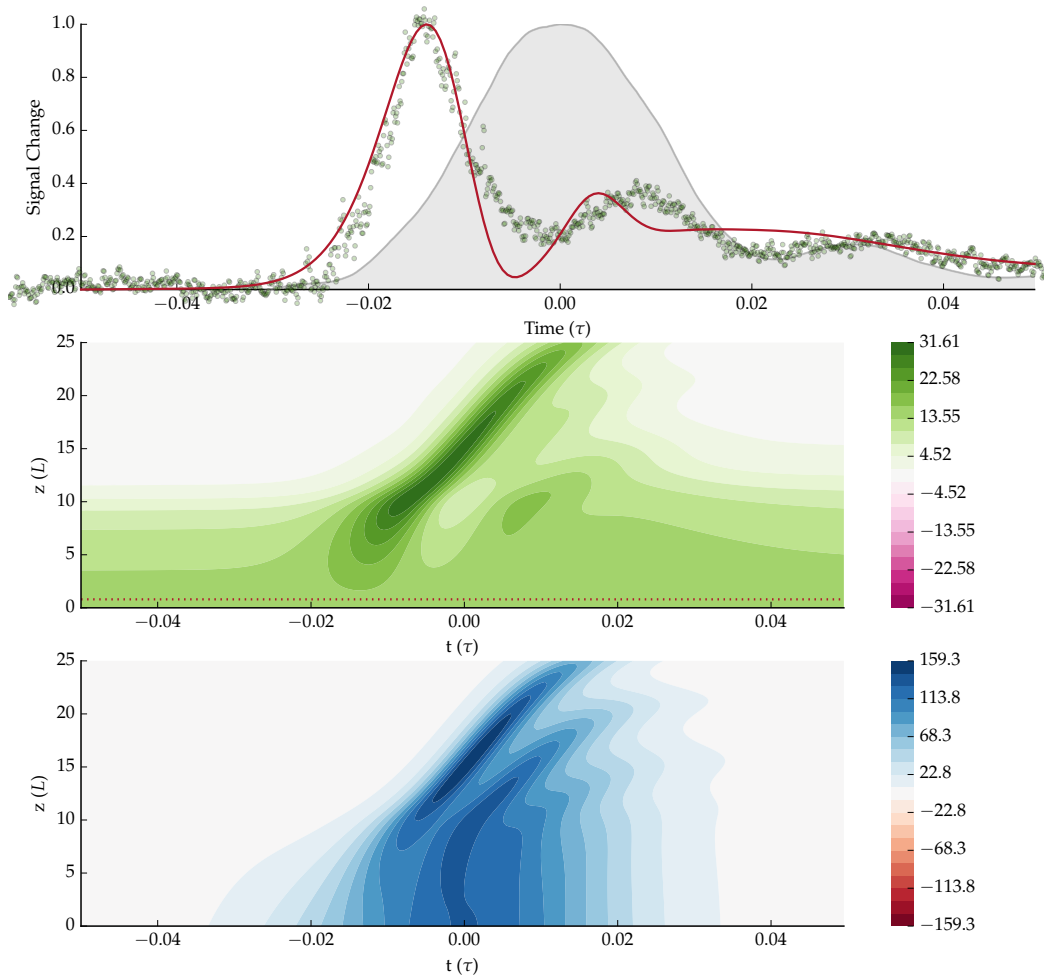


FIGURE 6.17 (Top) Comparison of numerical results (red) with experimental data (blue circles) for the normalised transmitted probe signal. The measured coupling pulse signal (grey filled area) has a width  $\tau_w = 0.80\text{ ns} \equiv 0.029\Gamma_\tau$  in each case. The temperature is  $230^\circ\text{C}$ . (Middle) Colour map of the real part of the complex Rabi frequency for the probe field. The red dotted line marks  $z = 1L$ . (Bottom) Colour map of the real part of the complex Rabi frequency for the coupling pulse.

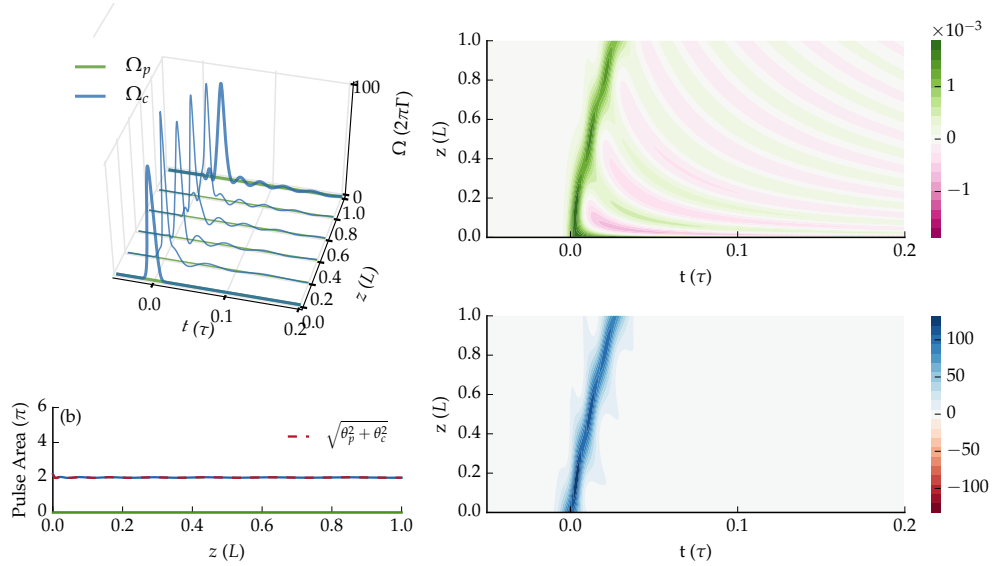


FIGURE 6.18 Propagation of a  $2.2\pi$  Gaussian input coupling pulse with width  $0.01\tau$  through the V-type medium addressed by a weak  $\Omega_p = 0.001\Gamma$  cw probe field. The number density is such that  $N_g = 2\pi 10^3 \Gamma/L$ . (Top left) Propagation profile of the probe (green) and coupling (blue) fields. (Bottom left) Pulse areas of the fields and the total area (red dashed). (Right) Colourmaps of the real part of the complex Rabi frequencies  $\Omega_p$  and  $\Omega_c$ .

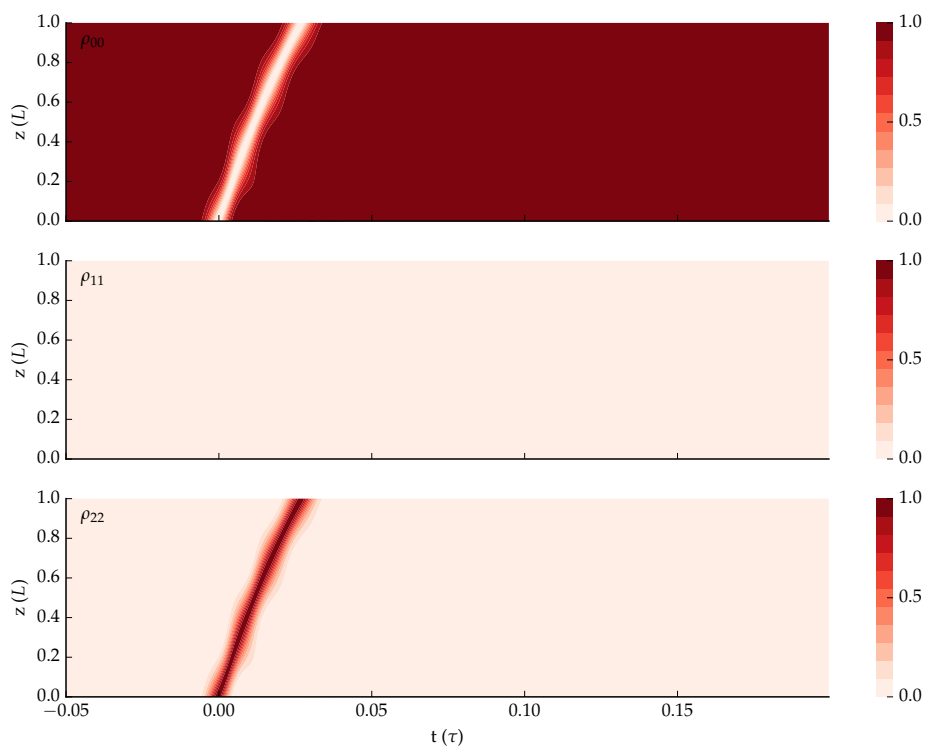


FIGURE 6.19 Populations of the ground state (top)  $\rho_{00}$  and excited states  $\rho_{11}$  (middle) and  $\rho_{22}$  (bottom) over  $z$  and  $t$  during the  $0.01\tau$  through the V-type medium addressed by a weak  $\Omega_p = 0.001\Gamma$  cw probe field, as shown in figure 6.18.

## 7 *Conclusions*

# *A Dynamics of Open Quantum Systems*

## *A.1 The Density Operator*

We typically describe the state of a quantised atomic system via its state vector

$$|\psi\rangle = \sum_j c_j |j\rangle, \quad (\text{A.1})$$

a linear superposition of the eigenstates  $|j\rangle$ . There are many physical situations, however, in which there is significant coupling to an external environment the state evolution of which we cannot follow.

Atom-light interactions are one such system. While the processes of absorption and stimulated emission (of photons from and to the applied field) can be described within a *closed quantum system*, the process of spontaneous decay due to interaction with vacuum fluctuations surrounding an atom cannot.

For such *open quantum systems* it is useful to generalise the concept of  $|\psi\rangle$  to that of the *density operator*  $\rho$ . A *pure state* is one that can be represented by a linear superposition as in (A.1), for which the density matrix is defined as  $\rho = |\psi\rangle\langle\psi|$ . This is clearly equivalent in information to  $|\psi\rangle$ . The usefulness of the density operator  $\rho$  is that it can be generalised in a

statistical way to represent incoherent superpositions of wavefunctions. We assume we have a mixture of states  $|\psi_s\rangle$  each with different expansions in the eigenbasis  $|j\rangle$ , contained in the ensemble with probabilities  $P(s) \geq 0$ . The density operator for this general *mixed state* is then defined as

$$\rho = \sum_s P(s) |\psi_s\rangle \langle \psi_s| \quad (\text{A.2})$$

where for proper normalisation

$$\sum_s P(s) = 1. \quad (\text{A.3})$$

We may consider that  $|\psi\rangle$  describes the intrinsic Heisenberg uncertainty required by quantum mechanics, where  $\rho$  is also able to describe additional uncertainty representing our state of knowledge of the system.<sup>51</sup>

The matrix representation of the density operator in a particular basis is also known as the density matrix. The off-diagonal elements  $\rho_{jk} = \langle j | \rho | k \rangle$  depend on relative phase of the coefficients and are known as *coherences*. The diagonal matrix elements  $\rho_{jj} = \langle j | \rho | j \rangle$  represent the probability of a measurement finding the system in state  $|j\rangle$  and are known as *populations*. These populations form a probability distribution and so must be normalised such that

$$\text{Tr} [\rho] = \sum_j \rho_{jj} = 1. \quad (\text{A.4})$$

The expectation value of an operator  $A$  in the density matrix formalism is given by

$$\langle A \rangle = \text{Tr} [A \rho]. \quad (\text{A.5})$$

## A.2 The Master Equation

By substituting the density operator  $\rho$  into the standard Schrödinger equation for motion of the quantum state

$$i\hbar \frac{\partial}{\partial t} |\psi\rangle = \mathcal{H} |\psi\rangle$$

we obtain the *von Neumann equation* for unitary evolution

$$i\hbar \frac{\partial \rho}{\partial t} = [\mathcal{H}, \rho] \quad (\text{A.6})$$

which for pure states is equivalent to the Schrödinger equation.

We wish to extend the formalism to mixed states and derive an equation of motion for the open quantum system interacting with an environment. The observed effect of interaction with an unmonitored environment is to introduce non-deterministic transitions between eigenstates and dephasing between them.

We start by expanding the model to include the environment, such that the total system is closed and described by (A.6). In order to meet this requirement, we must consider the Hilbert space of the total system, and a total Hamiltonian operating over that space

$$\mathcal{H}_\Sigma = \mathcal{H} + \mathcal{H}_E + \mathcal{H}_C \quad (\text{A.7})$$

where  $\mathcal{H}$  is the Hamiltonian of the system,  $\mathcal{H}_E$  is the Hamiltonian of the environment, and  $\mathcal{H}_C$  is the Hamiltonian describing the interaction between the system and the environment.

As we're only concerned with the dynamics of  $\mathcal{H}$ , we then make a partial trace over the environment degrees of freedom in (A.6) to obtain a master equation for time evolution of the system. The *Lindblad master equation* is a general, trace-preserving and positive form for the reduced density matrix  $\rho$ , given by

$$i\hbar \frac{\partial \rho}{\partial t} = [\mathcal{H}, \rho] + \mathcal{L} \{\rho\} \quad (\text{A.8})$$

where the Lindblad term given by

$$\mathcal{L}\{\rho\} = \sum_j C_j \rho C_j^\dagger - \frac{1}{2} \left( \rho C_j^\dagger C_j + C_j^\dagger C_j \rho \right) \quad (\text{A.9})$$

is a superoperator describing the system interaction with its environment via collapse operators  $C_j$  coupling states. For example, to account for a stochastic interaction with the environment representing the decay of a system from state  $|k\rangle$  to state  $|j\rangle$  with rate  $\Gamma_{jk}$ , we include a collapse operator

$$C_j = \sqrt{\Gamma_{jk}} |j\rangle \langle k|$$

in the Linblad term.

For the Lindblad equation (A.8) to be applicable as a master equation for the system, a couple of approximations must be justified. Firstly, the Born approximation requires that the environment is sufficiently large that it is not much affected by interaction with the system. We may write this as

$$\rho_\Sigma \approx \rho \otimes \rho_E. \quad (\text{A.10})$$

Secondly, the Markov approximation requires that the time evolution depends on  $\rho(t)$  and not any past history — this is also called a ‘short-memory environment’.

*B Numerical Integration of the  
Lindblad Master Equation for  
Large Density Matrices*

# C Numerical Integration of the Maxwell-Bloch Equations

In this appendix we describe the design and implementation of numerical methods to solve the coupled Maxwell-Bloch (MB) equations describing the nonlinear propagation of near-resonant light through thermal atomic vapours. The derivation of the MB equations is given in chapter 2 and simulated results from the scheme here described are presented throughout the thesis.

## C.1 Formulating the Problem

The MB equations are together equations (2.47) and (2.29), which we will restate here for completeness. They are the first-order Maxwell wave equation with the slowly-varying envelope approximation

$$\frac{\partial}{\partial z} \mathcal{E}(z, t') = i \frac{k}{2\epsilon_0} N(z) \sum_{i \neq j} d_{ij} \int_{-\infty}^{\infty} \rho_{ij}(z, t; v) f(v) dv.$$

describing propagation of the field envelope and the Lindblad master equation

$$i\hbar \frac{\partial \rho}{\partial t} = [\mathcal{H}, \rho] + \mathcal{L}\{\rho\}$$

describing the time-evolution of the atomic density matrix interacting with that field.

We describe the problem in the natural unit system defined in section ??, in terms of the length of the medium  $L$ , the natural linewidth of the transition  $\Gamma$  (specifically the probe transition in the case of schemes with multiple field modes) and its reciprocal natural decay time  $\tau = 1/\Gamma$ . Our goal is to solve the MB equations over a domain in 1D space  $z \in [0, 1]$  and co-moving time  $t' \in [t_{\min}, t_{\max}]$ .

We begin by setting up a discrete lattice over  $z$  and  $t'$ , with  $N_z$  equal spacesteps of length  $h_z = 1/N_z$ , such that  $z_j = j \cdot h_z \forall j \in \{0, 1, 2, \dots, N_z\}$  and  $N_t$  equal timesteps of duration  $h_t = 1/N_t$ , such that  $t_k = k \cdot h_t \forall k \in \{0, 1, 2, \dots, N_t\}$ .

The overall strategy is then to calculate values for the discretised electric field  $\mathcal{E}_{j,k}$  across the lattice, for which we must determine the macroscopic polarisation  $\mathcal{P}_{j,k}$  of the atoms, which in turn is derived from the density matrix  $\rho_{j,k}$ . A self-consistent algorithm is required for computation. Note that the electric field and polarisation envelopes in general consist of multiple modes, representing polarisations and wavelengths resonant with different transitions. For clarity in describing the scheme we will present only a single mode  $\mathcal{E}_{j,k}$ , but describe how the algorithm is extended to multiple modes later on.

We define a discrete set of detunings  $\{\Delta_l\}$ , representing atoms across a range of Doppler-shifted velocity classes. This range should be broad enough to cover the Maxwell-Boltzmann probability distribution and dense enough to accurately map the spectral absorption window. We will discuss those accuracy requirements in section C.3.

Any formulation of an integration scheme for partial differential equations is complete only with the definition of appropriate boundary conditions. Here we take a boundary condition for the field at the front of the medium (*i.e.*  $j = 0$ ) defining the field profile over time input on the medium  $\mathcal{E}_{j=0,k}$ . In a typical simulation of experiment this might be a

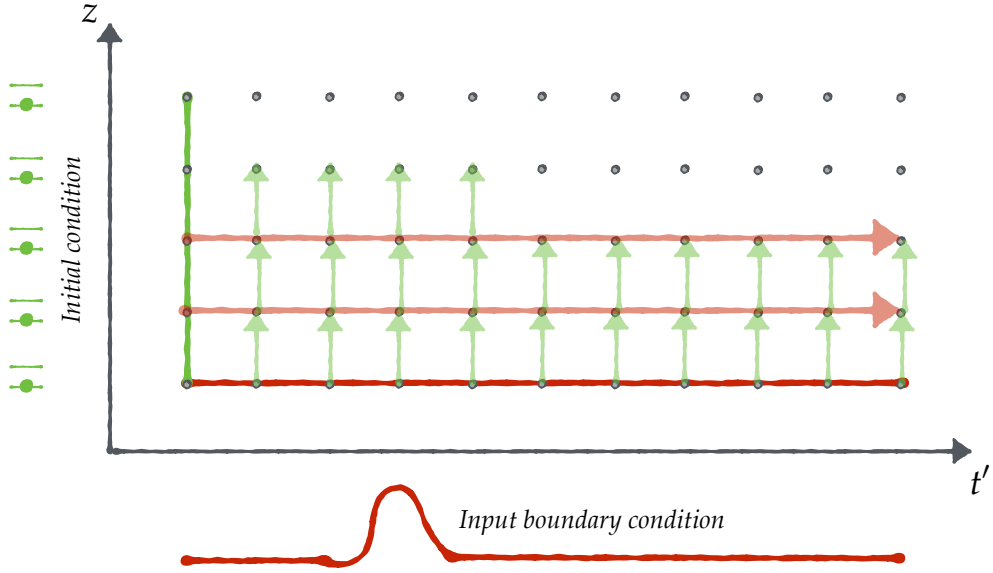


FIGURE C.1 Finite difference integration scheme for the Maxwell-Bloch equations.

The equations are solved for a discrete lattice over space  $z$  and co-moving time  $t'$ . At each lattice point  $(z_j, t'_k)$  we wish to solve for the electric field  $\mathcal{E}(z_j, t'_k)$  and the atomic density matrix  $\rho(z_j, t'_k)$ . The initial condition is illustrated by the two-level icons on the left. The boundary condition defining the electric field pulse profile over time input on the medium is illustrated by the sketched pulse at the bottom.

pulse or a ramp-on to a cw field. We must also specify an initial condition for the density matrix  $\rho_{j,k=0}$ . Typically we set this such that all population starts off in the atomic ground state.

## C.2 Computational Scheme

The finite difference scheme is illustrated in figure C.1 and sketched out with pseudocode in algorithm 1. For each spacestep index  $j$  in the medium, we take the field  $\mathcal{E}_{j,k}$  arriving on that step for all timesteps  $t'_k$ . For the first spacestep ( $j = 0$ ) this is the input boundary condition, il-

---

**Algorithm 1** Maxwell-Bloch integration.

---

```

1: for  $j = 2$  to  $N_z$  do                                 $\triangleright$  Loop over spacesteps
2:   for  $l = 0$  to  $N_\Delta$  do                       $\triangleright$  Loop over velocity classes
3:      $\rho_j^l = \text{solve\_lindblad}(\rho_{\text{init}}, \mathcal{E}_j, \Delta_l)$ 
4:   end for
5:   for  $k = 0$  to  $N_t$  do                       $\triangleright$  Loop over timesteps
6:      $\mathcal{P}_{j,k} = \mathcal{N}_z \sum_{a \neq b} \int_l d_{ab} \rho_{j,k}^l [a, b] f(\Delta_l, u) d\Delta$ 
7:      $\mathcal{E}_{j+1,k} = \mathcal{E}_{j+1,k} + i h_z \frac{k}{2\varepsilon_0} \left[ \frac{3}{2} \mathcal{P}_{j,k} - \frac{1}{2} \mathcal{P}_{j-1,k} \right]$        $\triangleright$  The AB step
8:   end for
9: end for

```

---

lustrated in red in figure C.1. Next (lines 2–4 in the pseudocode) we loop over the velocity classes  $l$  and pass the detuning  $\Delta_l$ , the field profile  $\mathcal{E}_{j,k}$  and an initial condition ( $\rho_{\text{init}}$ ) to the Lindblad solver described in Appendix B. That solver contains an implicit loop through the  $N_t$  timesteps, and integrates the Lindblad equation to find the density matrix at each of those timesteps  $t'_k$ .

At this point we have solved for the density matrix  $\rho_j^l$  at the spacestep  $z_j$  for each time  $t_k$  and for atoms in each velocity class  $l$ . In a loop over the timestep index  $k$  (lines 5–8) we then perform an average of the density matrix coherences over detuning, weighted by the Maxwell-Boltzmann probability distribution for a defined width  $u$ , and sum them to find (line 6) the polarisation  $\mathcal{P}_{j,k}$  at that point in space  $z_j$  and time  $t_k$ .

Once we have computed the polarisation, and still within the loop over timesteps, we can advance the field at that timestep to the next spacestep  $\mathcal{E}_{j+1,k}$  in the medium for each  $k$  using a second-order Adams-Bashforth method. Note then that this method is not strictly chronological, but is self-consistent in the co-moving frame of reference.

### C.2.1 Details of the Algorithm

The pseudocode above describes the general calculation scheme, but omits a number of details that we will now describe.

First, we have considered only a single field mode. For multiple modes, we must input all of those modes to the Lindblad solver (in line 3). We must also calculate polarisations for each mode separately from its coupled transitions (line 6) and advance the fields for each mode (line 7).

Second, note that we started the spacestep loop (line 1) at  $j=2$ . The two-step Adams-Bashforth method requires two starting points to begin. We therefore use an explicit Euler step to take the input field at  $j=0$  to the next step at  $j=1$ . As the local error in the Euler step is of order  $\mathcal{O}(h_z)$ , we use a smaller step to avoid introducing a large global error. The second step is then a two-step Adams-Bashforth with different stepsizes.

The correct difference formula for this step (D.6) is derived in Appendix D. The remaining steps use the standard two-step Adams-Bashforth step as shown in the pseudocode.

Third, the Lindblad solver (line 3) requires the electric field envelope  $\mathcal{E}_j$  to be passed as a function of time, rather than an array, as the adaptive method may choose different inner stepsizes (*i.e.* steps between  $t'_k$  and  $t'_{k+1}$  for any  $k$ ) that we do not know in advance. We construct this function for arbitrary points in the time domain using quadratic spline interpolation.<sup>71,72</sup>

Fourth, the complex values for the field envelopes  $\mathcal{E}_{j,k}$  and atomic density matrix  $\rho_{j,k}$  across the lattice is saved to disc in binary format, such that the results of each simulation can be loaded without needing the calculation to be repeated. To optimise storage and memory requirements, a data resolution in  $z_h$  and  $t_k$  may be specified, sufficient for analysis and visualisation without needing to record all of the steps that

may be required for stability and accuracy.

Spectral analysis of the results is performed using a discrete Fourier transform of the complex field.<sup>71</sup>

### C.2.2 Code Implementation

The algorithm for solving the MB equations was implemented in Python using the SciPy scientific computing stack.<sup>73,74</sup>

The code uses the OB class of the OpticalBloch package described in appendix B in order to define the atom-light interaction and solve the Lindblad equation for instances representing various atomic systems, with few-level or with full angular momentum structure. The QuTiP library<sup>75</sup> is used for quantum state and operator objects and its master equation solver for dynamics of open quantum systems.

## C.3 Convergence & Accuracy

We check the accuracy of the method with a quantitative measurement of the convergence of results for a particular system with increased number of spacesteps and velocity classes. We wish the results to be as accurate as possible, but with an awareness of the trade-off that the computational complexity (and thus running time) scales with  $\mathcal{O}(N_z)$  and  $\mathcal{O}(N_\Delta)$  where  $N_\Delta$  is the number of velocity classes.

In figure C.2 we show the results of convergence of the integrated solutions for different numbers of spacesteps  $N_z$  between 10 and 500. The convergence is measured relative to a benchmark at 10,000 spacesteps — a number which ensures high accuracy but is too slow for performing many calculations. The maximum value of the absolute difference

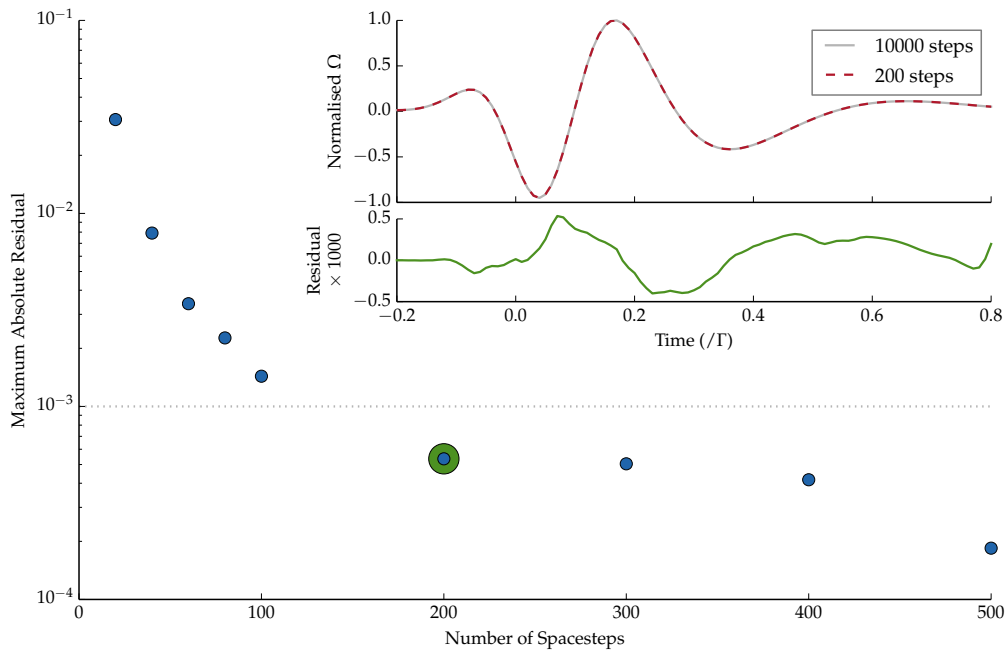


FIGURE C.2 Convergence of an example integrated solution, for a weak pulse in a medium with  $\mathcal{N}g = 2\pi 100$  MHz, for different numbers of spacesteps  $N_z$ . (Main plot) The minimum absolute residual between an integrated solution  $N_z$  and a benchmark solution with 10,000 steps (blue circles), plotted on a logarithmic  $y$ -axis. The dotted line represents a chosen accuracy requirement of  $10^{-3}$  and the green circled data point is the lowest number of steps tested which meets this requirement, in this case  $N_z = 200$ . (Inset) Normalised  $\Omega$  against time at the final spacetime step  $j = N_z$  for both the benchmark and the  $N_z = 200$  run, with the residual shown underneath.

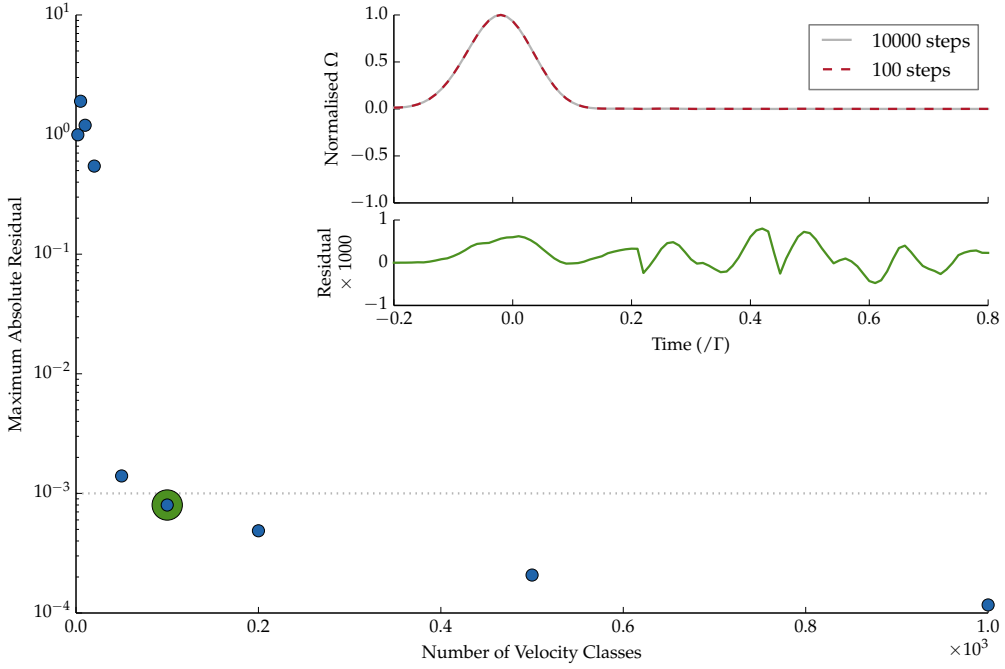


FIGURE C.3 Convergence of an example integrated solution, for a weak pulse in a medium with  $\mathcal{N}g = 2\pi 100 \Gamma/\text{L}$  and a thermal width of  $2\pi 10 \Gamma$ , for different numbers of velocity classes  $N_\Delta$ . (Main plot) The minimum absolute residual between an integrated solution  $N_\Delta$  and a benchmark solution with 10,000 velocity classes, plotted on a logarithmic  $y$ -axis. The dotted line represents a chosen accuracy requirement of  $10^{-3}$  and the green circled data point is the lowest number of steps tested which meets this requirement, in this case  $N_\Delta = 100$ . (Inset) Normalised  $\Omega$  against time at the final spacestep  $j = N_j$  for both the benchmark and the  $N_\Delta = 100$  run, with the residual shown underneath.

(residual) between the benchmark and each run is plotted. We see that the maximum absolute residual decreases with the number of steps  $N_z$  down to 200 steps, after which the increase in accuracy for an increased number of steps is reduced. If we choose a tolerance for the maximum absolute residual of  $10^{-3}$  (shown by the dotted line), the first tested run within that tolerance is  $N_z = 200$ . Running simulations with this number of spacesteps would therefore reduce calculation many times over the benchmark while keeping a sufficient level of accuracy.

In figure C.3 we show a similar figure for results of convergence for the integrated solutions for different numbers of velocity classes  $N_\Delta$  between 1 and 1,000 spread over a width of  $2\pi 40\Gamma$ .

The convergence is measured relative to a benchmark at 10,000 velocity classes. We see that the maximum absolute residual is large for few velocity classes, around 1. If we again choose a tolerance for the maximum absolute residual of  $10^{-3}$  (shown by the dotted line), the first tested run within that tolerance is  $N_z = 100$ . The ‘return on investment’ for additional velocity classes is reduced from then on, with  $N_z = 1,000$  not providing an order of magnitude improvement in accuracy.

In picking a range of velocity classes for an accurate simulation, there are two important considerations. First, it is important to cover the Maxwell- Boltzmann distribution. We check the integration width is sufficient by using a simple trapezoidal integration over the discrete Maxwell-Boltzmann distribution to ensure it is close to unity. In each of the calculations above we used an evenly-spaced sampling over four times the FWHM. The integral is far from unity until around 20 detuning steps (when it reaches 0.995), which explains why we don’t see convergence in the first few samples. Second, it is important to sample accurately the Lorentzian resonance window, which is typically much smaller than the thermal width (in our case it is specified to be  $2\pi 1\Gamma$ ). In order to achieve both of these goals with an optimised number of detuning steps, we use a non-evenly spaced grid with a denser number of velocity classes around resonance, which can improve accuracy without requiring as many velocity classes.

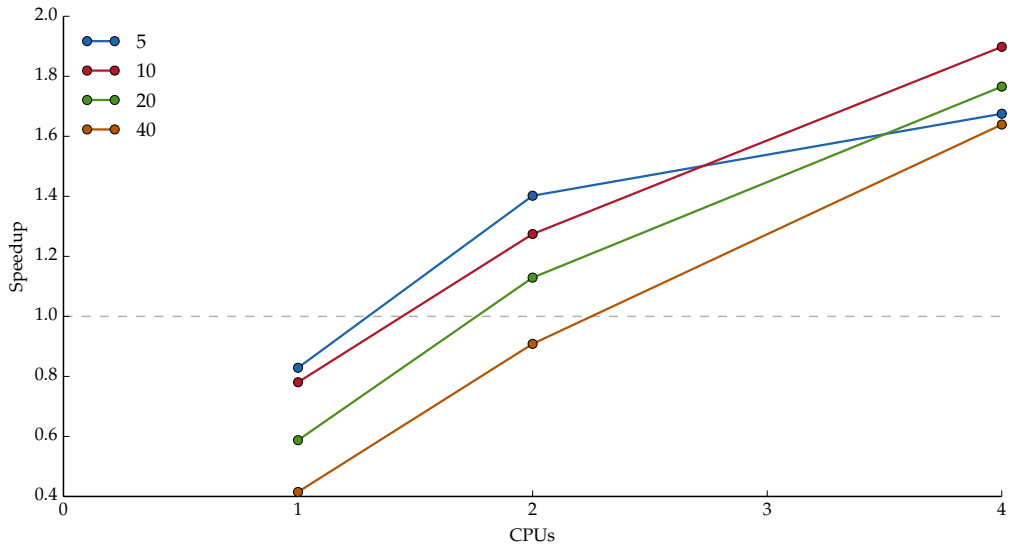


FIGURE C.4 Speedup of parallelised computation versus number of CPUs for different numbers of velocity classes  $N_\Delta = \{5, 10, 20, 40\}$ , relative to the serial algorithm. Each data point is ‘best of two’ to avoid times where the CPUs might otherwise be used by the operating system.

## C.4 Parallelisation & Performance

The pseudocode in algorithm 1 contains a number of nested loops, which leads us to consider if any parts of the implementation may readily be parallelised.

The iterations of the outermost loop over spacesteps  $z_j$  (algorithm 1, line 1) are not independent (*i.e.* the field at a point in space  $j$  is dependent on the previous space points  $0, 1, \dots, j - 1$ ) which necessitates that these be processed in serial. However, the iterations of the inner loop over velocity classes  $\Delta_l$  (algorithm 1, line 2), calculate the evolution of atoms subject to different Doppler shifts with respect to the fields along  $z$ . The evolution of each class is completely independent of the others so these may be processed in parallel, with the weighted average calculated at the end.

In figure C.4 we present measured speedup of parallelised computation with increasing number of CPU for example simulations using 5, 10, 20 and 40 velocity classes, relative to the serial code.

We see that, for all numbers of velocity classes tested, using the parallel code but only allowing use of a single CPU incurs a slowdown due to the overhead of passing objects into the parallelised functions.

In general the speedup decreases with the number of velocity classes, which indicates that there is significant overhead in parallelisation. With 2 CPUs we have speedup up to the case of 20 velocity classes. With 4 CPUs, the parallel algorithm results in significant speedup, above 60% in each case. The speedup for 5 velocity classes with 4 CPUs or more is obviously limited.

The Lindblad solver routine in the velocity class loop represents the most computationally-intensive part of the whole algorithm, so it is certainly useful to be able to make use of multiple core computers to perform these calculations. For the work described in this thesis we made use of an Intel Core i7 with up to 4 CPU cores, and for the most intensive calculations we used Durham University's *Hamilton* HPC Cluster with up to 12 CPU cores for each simulation.

Another process which could be computed in parallel is the iteration over timesteps  $t_k$  (algorithm 1, line 7), which performs the weighted average over density matrix coherences to determine the polarisation of the medium at that time, and advances the field via the AB step. However, for the number of timesteps used in calculations we saw negligible speedup due to the high overhead required for this loop in passing arrays containing the polarisations and fields. In fact, for systems where less than  $N_k = 1000$  timesteps are required for the necessary accuracy, this overhead caused the parallel implementation to be slower than the serial. It was therefore not used.

For fields with many modes, loops over these modes could be parallelised for computing polarisation. In this work we have only needed to consider systems of one or few modes, so it was not appropriate to implement parallelisation here.

## *D The Two-Step Adams-Bashforth Method with Varying Stepsize*

Adams-Bashforth integration methods have a well-known derivation but we are not aware of a reference for the two-step method in the case that the two stepsizes are different, so we present the result here. This numerical method is used in solving the MB equations as described in chapterC. The two-step method requires two initial points, and the second point is calculated using a Euler step, which we wish to keep small to avoid introducing a large global error. The third point is then calculated with the Adams-Bashforth method with different step sizes. From then on the standard Adams-Bashforth method can be used.

We take an ordinary differential equation  $y' = f(z, y(z))$  with an initial condition  $y(z_0) = y_0$  that we wish to solve numerically. If we know  $y(z)$  at a time  $z_n$  and want to know what  $z$  is at a later time  $z_{n+1}$ , the fundamental theorem of calculus tells us that we find it by integrating  $y'$  over the time interval

$$y(z_{n+1}) = y(z_n) + \int_{z_n}^{z_{n+1}} y'(z) dz = y(z_n) + \int_{z_n}^{z_{n+1}} f(z, y(z)) dz. \quad (\text{D.1})$$

The idea behind any ODE integrator is to compute the right-hand-side integral for some numerical approximation of  $f$ . The problem is then computed over a series of steps  $n = 1, 2, \dots, N$  to give a sequence of points  $z_n$  which approximate  $y(z)$  to some order of accuracy as a func-

tion of the stepsize. The method is consistent if the local error (*i.e.* the error from step  $n$  to step  $n + 1$ ) goes to zero faster than the stepsize  $(z_{n+1} - z_n)$  goes to zero.

Where the Euler method takes the slope  $f$  to be a constant on the interval  $[z_n, z_{n+1}]$ , the idea behind Adams-Bashforth methods is to approximate  $f$  by a Lagrange interpolating polynomial<sup>76</sup>

$$P(z) = \sum_{j=1}^m P_j(z) \quad (\text{D.2})$$

where

$$P_j(z) = y_j \prod_{\substack{k=1 \\ k \neq j}}^m \frac{z - z_k}{z_j - z_k}. \quad (\text{D.3})$$

Here  $P(z)$  is the polynomial of degree  $\leq (m - 1)$  that passes through the  $m$  points  $(z_1, y_1 = f(z_1)), (z_2, y_2 = f(z_2)) \dots (z_m, y_m = f(z_m))$ . We'll take the linear ( $m = 2$ ) interpolant on the point  $z_n$  and an earlier point  $z_{n-1}$ , so we have

$$P(z) = f(z_n, y_n) \frac{z - z_{n-1}}{z_n - z_{n-1}} + f(z_{n-1}, y_{n-1}) \frac{z - z_n}{z_{n-1} - z_n}. \quad (\text{D.4})$$

Now if we substitute this approximating polynomial into the integral in (D.1), we find

$$\begin{aligned} \int_{z_n}^{z_{n+1}} f(z, y(z)) dz &\approx \int_{z_n}^{z_{n+1}} P(z) dz \\ &= \int_{z_n}^{z_{n+1}} \left[ f(z_n, y_n) \frac{z - z_{n-1}}{z_n - z_{n-1}} + f(z_{n-1}, y_{n-1}) \frac{z - z_n}{z_{n-1} - z_n} \right] dz \end{aligned}$$

into which we may then put in the limits to obtain

$$\begin{aligned} \int_{z_n}^{z_{n+1}} f(z, y(z)) dz &\approx \frac{(z_n - z_{n+1})}{2(z_{n-1} - z_n)} \left[ f(z_n, y_n)(z_n + z_{n+1} - 2z_{n-1}) \right. \\ &\quad \left. - f(z_{n-1}, y_{n-1})(z_n - z_{n+1}) \right]. \quad (\text{D.5}) \end{aligned}$$

If we let  $h_1 := z_n - z_{n-1}$  and  $h_2 := z_{n+1} - z_n$  then

$$\int_{z_n}^{z_{n+1}} P(z) dz = \frac{h_2}{2h_1} [(2h_1 + h_2)f(z_n, y_n) - h_2 f(z_{n-1}, y_{n-1})].$$

Putting this back into the approximation of (D.1), we get

$$y(z_{n+1}) \approx y(z_n) + \frac{h_2}{2h_1} [(2h_1 + h_2)f(z_n, y_n) - h_2 f(z_{n-1}, y_{n-1})]$$

and our sequence of approximation points  $y_n$  is calculated as

$$y_{n+1} = y_n + \frac{h_2}{2h_1} [(2h_1 + h_2)f(z_n, y_n) - h_2 f(z_{n-1}, y_{n-1})] \quad (\text{D.6})$$

for  $n = 1, 2, \dots, N$ . This is the correct second-order Adams-Bashforth finite difference step in the case that the stepsizes are different.

If the steps are of equal size, i.e.  $h := h_1 = h_2$  we find

$$y_{n+1} = y_n + \frac{3}{2}hf(z_n, y_n) - \frac{1}{2}hf(z_{n-1}, y_{n-1}) \quad (\text{D.7})$$

which is the standard two-step Adams-Bashforth method.<sup>77,78</sup>

## *Acknowledgements*

I would like to thank...

## Bibliography

- <sup>1</sup> J D Jackson. *Classical Electrodynamics*. Wiley, 1998.
- <sup>2</sup> R W Boyd. *Nonlinear Optics*. Nonlinear Optics Series. Elsevier Science, 2008.
- <sup>3</sup> E Hecht. *Optics*. Pearson Education, 2015.
- <sup>4</sup> P Lambropoulos and D Petrosyan. *Fundamentals of Quantum Optics and Quantum Information*. Springer, 2007.
- <sup>5</sup> D J Griffiths. *Introduction to Electrodynamics*. Prentice Hall, 1999.
- <sup>6</sup> Mary B. James. Why the speed of light is reduced in a transparent medium, 1992.
- <sup>7</sup> R P Feynman, R B Leighton, and M L Sands. *The Feynman Lectures on Physics*. Number v. 1 in The Feynman Lectures on Physics. Addison-Wesley, 1963.
- <sup>8</sup> B H Bransden and C J Joachain. *Physics of Atoms and Molecules*. Pearson Education. Prentice Hall, 2003.
- <sup>9</sup> G Grynberg, A Aspect, C Fabre, and C Cohen-Tannoudji. *Introduction to Quantum Optics: From the Semi-classical Approach to Quantized Light*. Cambridge University Press, 2010.

- <sup>10</sup> C Cohen-Tannoudji, J Dupont-Roc, and G Grynberg. *Atom-photon interactions: basic processes and applications*. Wiley-Interscience publication. J. Wiley, 1992.
- <sup>11</sup> Charles S. Adams and Erling Riis. Laser Cooling and Manipulation of Neutral Particles. pages 1–39, 1997.
- <sup>12</sup> A. Icsevgi and W. E. Lamb. Propagation of light pulses in a laser amplifier. 1429, 1964.
- <sup>13</sup> C J Foot. *Atomic physics*. Oxford master series in physics. Oxford University Press, 2005.
- <sup>14</sup> J. Gea-Banacloche, Yong-qing Li, Shao-zheng Jin, and Min Xiao. Electromagnetically induced transparency in ladder-type inhomogeneously broadened media: Theory and experiment. *Physical Review A*, 51(1):576, 1995.
- <sup>15</sup> R Loudon. *The Quantum Theory of Light*. OUP Oxford, 2000.
- <sup>16</sup> L Allen and Joseph H Eberly. *Optical Resonance and Two-level Atoms*. Dover books on physics and chemistry. Dover, 1975.
- <sup>17</sup> a. V. Durrant. Some basic properties of stimulated and spontaneous emission: A semiclassical approach. *American Journal of Physics*, 44(7):630, 1976.
- <sup>18</sup> Edwin Hewitt and Robert E. Hewitt. The Gibbs-Wilbraham phenomenon: An episode in fourier analysis. *Archive for History of Exact Sciences*, 21(2):129–160, 1979.
- <sup>19</sup> Paul Siddons, Charles S. Adams, Chang Ge, and Ifan G. Hughes. Absolute absorption on rubidium D lines: comparison between theory and experiment. *Journal of Physics B: Atomic, Molecular and Optical Physics*, 41(15):155004, aug 2008.

- <sup>20</sup> S.L. McCall and E.L Hahn. Self-Induced Transparency. *Physical Review*, 183, 1969.
- <sup>21</sup> GL Lamb. Analytical descriptions of ultrashort optical pulse propagation in a resonant medium. *Reviews of Modern Physics*, 43(2), 1971.
- <sup>22</sup> Y S Kivshar and G Agrawal. *Optical Solitons: From Fibers to Photonic Crystals*. Elsevier Science, 2003.
- <sup>23</sup> L Matulic and Joseph H Eberly. Analytic study of pulse chirping in self-induced transparency. *Phys Rev A*, 6, 1972.
- <sup>24</sup> R. E. Slusher and H. M. Gibbs. Self-induced transparency in atomic rubidium. *Physical Review A*, 5(4):1634–1659, 1972.
- <sup>25</sup> G G Grigoryan and Y Pashayan. Propagation of pulses in a three-level medium at exact two-photon resonance. *Physical Review A*, 64(1):013816, 2001.
- <sup>26</sup> R. Unanyan, Michael Fleischhauer, B.W. Shore, and K. Bergmann. Robust creation and phase-sensitive probing of superposition states via stimulated Raman adiabatic passage (STIRAP) with degenerate dark states. *Optics Communications*, 155(1-3):144–154, 1998.
- <sup>27</sup> V.R. Blok and G.M. Krochik. Lasing Without Inversion. *Digest on Nonlinear Optics: Materials, Phenomena and Devices*, 7, 1990.
- <sup>28</sup> A Imamolu and Stephen E. Harris. Lasers without inversion: interference of dressed lifetime-broadened states. *Optics letters*, 14(24):1344–1346, 1989.
- <sup>29</sup> Marlan O. Scully, Shi Yao Zhu, and Athanasios Gavrielides. Degenerate quantum-beat laser: Lasing without inversion and inversion without lasing. *Physical Review Letters*, 62(24):2813–2816, 1989.

- <sup>30</sup> Marlan O Scully. Enhancement of the index of refraction via quantum coherence. *Physical Review Letters*, 67(14):1855–1858, 1991.
- <sup>31</sup> J. Eberly, A. Rahman, and R. Grobe. Index of Refraction for an Optical Medium with Clamped Quantum Phase. *Physical Review Letters*, 77(9):1912–1912, 1996.
- <sup>32</sup> Jonathan D Pritchard, Daniel T Maxwell, a Gauguet, Kevin J. Weatherill, M P A Jones, and Charles S. Adams. Cooperative Atom-Light Interaction in a Blockaded Rydberg Ensemble. *Physical Review Letters*, 105(19):1–4, nov 2010.
- <sup>33</sup> M J Konopnicki and Joseph H Eberly. Simultaneous propagation of short different-wavelength optical pulses. *Physics Letters A*, 24(5):2567, 1981.
- <sup>34</sup> M.J. Konopnicki, P.D. Drummond, and Joseph H Eberly. Theory of lossless propagation of simultaneous different-wavelength optical pulses, 1981.
- <sup>35</sup> A Kujawski. Soliton properties of optical multistates. 43(5):375–377, 1982.
- <sup>36</sup> G L Lamb. *Elements of soliton theory*. Pure and applied mathematics. Wiley, 1980.
- <sup>37</sup> Joseph H Eberly. Transmission of dressed fields in three-level media. *Quantum and Semiclassical Optics: Journal of the European Optical Society Part B*, 7(3):373–384, 1999.
- <sup>38</sup> Ashiqur Rahman and Joseph H Eberly. Theory of shape-preserving short pulses in inhomogeneously broadened three-level media. *Physical Review A*, 58(2):R805–R808, 1998.
- <sup>39</sup> Ashiqur Rahman and Joseph H Eberly. Numerical experiments with optical pulses in V-type media. *Optics express*, 4(3):133–138, 1999.

- <sup>40</sup> Lee Weller, R. J. Bettles, C. L. Vaillant, Mark A Zentile, R. M. Potvliege, Charles S. Adams, and Ifan G. Hughes. Cooperative Enhancement of Energy Transfer in a High-Density Thermal Vapor. *arXiv preprint arXiv: ...*, pages 1–8, 2013.
- <sup>41</sup> G. Bearman and J. Leventhal. Ionization and Energy Pooling in Laser-Excited Na Vapor, 1978.
- <sup>42</sup> R. H. Hill and H A Schuessler. Inelastic-Collisions between Selectively Excited Rubidium Atoms and Ground-State Rubidium Atoms. *Bulletin of the American Physical Society*, 24(9):1177–1177, 1979.
- <sup>43</sup> R. Namiotka, J. Huennekens, and M. Allegrini. Energy-pooling collisions in potassium. *Physical Review A*, 56(1):514–520, 1997.
- <sup>44</sup> James Keaveney, a. Sargsyan, Ulrich Krohn, Ifan G. Hughes, D. Sarkisyan, and Charles S. Adams. Cooperative Lamb Shift in an Atomic Vapor Layer of Nanometer Thickness. *Physical Review Letters*, 108(17):1–5, apr 2012.
- <sup>45</sup> Lee Weller, Robert J Bettles, Paul Siddons, Charles S. Adams, and Ifan G. Hughes. Absolute absorption on the rubidium D 1 line including resonant dipole-dipole interactions. *Journal of Physics B: Atomic, Molecular and Optical Physics*, 44(19):195006, oct 2011.
- <sup>46</sup> J. E. Sansonetti. Wavelengths, transition probabilities, and energy levels for the spectra of rubidium (Rb I through Rb XXXVII). *Journal of Physical and Chemical Reference Data*, 35(1):301–421, 2006.
- <sup>47</sup> Ennio Arimondo, M. Inguscio, and P. Violino. Experimental determinations of the hyperfine structure in the alkali atoms. *Reviews of Modern Physics*, 49(1):31–75, 1977.

- <sup>48</sup> A Banerjee, D Das, and V Natarajan. Absolute frequency measurements of the D<sub>1</sub> lines in <sup>39</sup>K, <sup>85</sup>Rb, and <sup>87</sup>Rb with  $\sim 0.1$  ppb uncertainty, 2007.
- <sup>49</sup> E P Wigner and J J Griffin. *Group Theory and Its Application to the Quantum Mechanics of Atomic Spectra*. Pure and applied Physics. Academic Press, 1959.
- <sup>50</sup> Carl Eckart. The Application of Group theory to the Quantum Dynamics of Monatomic Systems. *Rev. Mod. Phys.*, 2(3):305–380, jul 1930.
- <sup>51</sup> Daniel Adam Steck. Quantum and Atom Optics. page 932, 2007.
- <sup>52</sup> M. S. Safronova and U. I. Safronova. Critically evaluated theoretical energies, lifetimes, hyperfine constants, and multipole polarizabilities in <sup>87</sup>Rb. *Physical Review A*, 83(5):052508, may 2011.
- <sup>53</sup> James Keaveney. *Cooperative interactions in dense thermal Rb vapour confined in nm-scale cells*. PhD thesis, 2013.
- <sup>54</sup> B. Huber, T. Baluktsian, M. Schlagmüller, a. Kölle, H. Kübler, R. Löw, and T. Pfau. GHz Rabi flopping to Rydberg states in hot atomic vapor cells. *Physical Review Letters*, 107(24):1–4, 2011.
- <sup>55</sup> T. Baluktsian, B. Huber, R. Löw, and T. Pfau. Evidence for strong van der Waals type Rydberg-Rydberg interaction in a thermal vapor. *Physical Review Letters*, 110(12):1–4, 2013.
- <sup>56</sup> James Keaveney, Ifan G. Hughes, a. Sargsyan, D. Sarkisyan, and Charles S. Adams. Maximal Refraction and Superluminal Propagation in a Gaseous Nanolayer. *Physical Review Letters*, 109(23):233001, dec 2012.
- <sup>57</sup> D V Schroeder. *An Introduction to Thermal Physics*. Addison Wesley, 2000.

- <sup>58</sup> E.L. Lewis. Collisional relaxation of atomic excited states, line broadening and interatomic interactions, 1980.
- <sup>59</sup> A Thorne, U Litzén, and S Johansson. *Spectrophysics: Principles and Applications*. Springer, 1999.
- <sup>60</sup> K. Razdan. Demonstrating optical saturation and velocity selection in rubidium vapor. *American Journal of Physics*, 67(9):832, 1999.
- <sup>61</sup> Kang Bin Im, Hye Yun Jung, Cha Hwan Oh, Seok Ho Song, Pill Soo Kim, and Ho Seong Lee. Saturated absorption signals for the Cs D<sub>2</sub> line. *Physical Review A - Atomic, Molecular, and Optical Physics*, 63(3):1–4, 2001.
- <sup>62</sup> S Nakayama. Theoretical analysis of Rb and Cs D<sub>2</sub> lines in Doppler-free spectroscopic techniques with optical pumping. *Japanese Journal of Applied Physics*, 24(1):1–7, 1985.
- <sup>63</sup> David a. Smith and Ifan G. Hughes. The role of hyperfine pumping in multilevel systems exhibiting saturated absorption. *American Journal of Physics*, 72(5):631, 2004.
- <sup>64</sup> Ben E. Sherlock and Ifan G. Hughes. How weak is a weak probe in laser spectroscopy? *American Journal of Physics*, 77(2):111, 2009.
- <sup>65</sup> Daniel Adam Steck. Rubidium 87 D line data. 2001.
- <sup>66</sup> Michael Fleischhauer, Atac Imamoglu, and Jonathan P Marangos. Electromagnetically induced transparency : Optics in coherent media. *Reviews of Modern Physics*, 77(2):633–673, 2005.
- <sup>67</sup> Robert Potvliege. No Title. personal communication.
- <sup>68</sup> Daniel T Maxwell, D. J. Szwer, D. Paredes-Barato, H. Busche, Jonathan D Pritchard, A. Gauguet, Kevin J. Weatherill, M. P. a. Jones,

- and Charles S. Adams. Storage and Control of Optical Photons Using Rydberg Polaritons. *Physical Review Letters*, 110(10):103001, mar 2013.
- <sup>69</sup> Mark Saffman, Thad G Walker, and Klaus Mølmer. Quantum information with Rydberg atoms. *Reviews of Modern Physics*, 82(3):2313–2363, aug 2010.
- <sup>70</sup> M. F. Maghrebi, M. J. Gullans, P. Bienias, S. Choi, I. Martin, O. Firstenberg, M. D. Lukin, H. P. Büchler, and a. V. Gorshkov. Coulomb bound states of strongly interacting photons. *Phys. Rev. Lett.*, 115(September):123601, 2015.
- <sup>71</sup> W H Press. *Numerical Recipes 3rd Edition: The Art of Scientific Computing*. Cambridge University Press, 2007.
- <sup>72</sup> C. De Boor. On calculating with B-splines. *Journal of Approximation Theory*, 6(1):50–62, 1972.
- <sup>73</sup> Stéfan Van Der Walt, S. Chris Colbert, and Gaël Varoquaux. The NumPy array: A structure for efficient numerical computation. *Computing in Science and Engineering*, 13(2):22–30, 2011.
- <sup>74</sup> Eric Jones, Travis Oliphant, Pearu Peterson, and Others. {SciPy}: Open source scientific tools for {Python}.
- <sup>75</sup> P D Nation and J R Johansson. QuTiP : The Quantum Toolbox in Python. 2013.
- <sup>76</sup> G B Arfken and H J Weber. *Mathematical Methods For Physicists International Student Edition*. Elsevier Science, 2005.
- <sup>77</sup> L Edsberg. *Introduction to Computation and Modeling for Differential Equations*. Wiley, 2008.
- <sup>78</sup> Francis Bashforth and John Couch Adams. *An attempt to test the theories of capillary action: by comparing the theoretical and measured forms of*

*drops of fluid. With an explanation of the method of integration employed in constructing the tables which give the theoretical forms of such drops.* University Press, 1883.